Analysis of slow-light in Semiconductor Nanostructures

Henri Nielsen – s022050
Per Nielsen – s021719

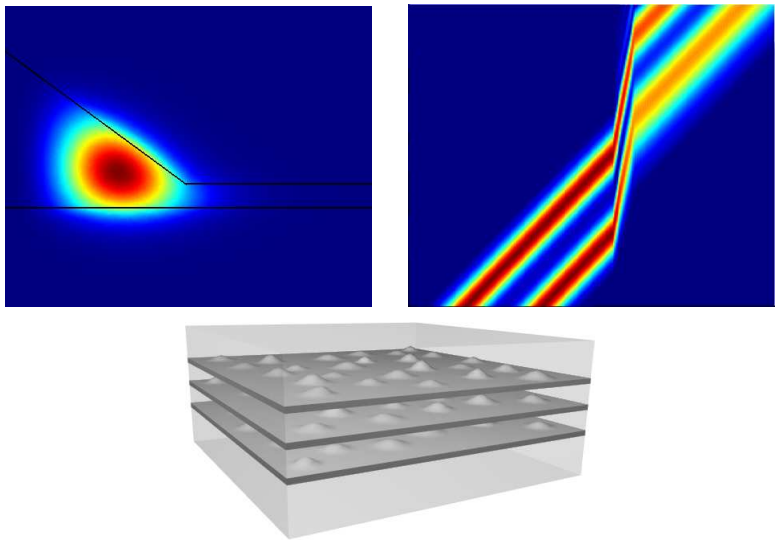

Supervisors:

Jesper Mørk and Bjarne Tromborg

Research Center COM
Technical University of Denmark

28th June 2005

The front page pictures: The first shows the radial probability of an electron in a rotationally symmetric quantum dot. The next shows two pulses propagating through an active quantum dot material, like the one sketched in the last picture.

Title:	Analysis of slow-light in Semiconductor Nanostructures
Project	Midterm project
Project period	Spring 2005

Group members:

Henri Nielsen

Per Nielsen

Supervisors:

Jesper Mørk

Bjarne Tromborg

Abstract

In this report we have analyzed the effect of Electromagnetically Induced Transparency (EIT). This has been done by using a quantum dot material to provide the necessary three-level system. A rotationally symmetric model of a quantum dot has been used to calculate eigenfunctions numerically by solving the Schrödinger equation under the envelope function approximation. These have been used to calculate the transition matrix elements for the dipole-allowed transitions used in the EIT analysis.

To simulate the light-matter interaction a semi-classical model has been set up. This consists of the optical Bloch equations where the interaction is due to a classical electric field, describing both the coupling and probe lasers. A steady state analysis of the Bloch equations in the limit of CW fields has been performed, to obtain analytical expressions for the complex susceptibility and refractive group index. These results have been compared to a dynamic model. In this the Bloch equations have been coupled to the wave equation for the probe field, to allow for pulses. Strong agreement between the two models is obtained for pulses not spectrally exceeding the EIT absorption window. If this is not not the case dipole beat oscillations are observed. Lastly, studies of two-pulse interactions have been done.

Preface

The present report is written as part of a 6th semester midterm project at the Technical University of Denmark under the Research Center COM. It is a presentation of our work on slow-light during the spring of 2005, from February to June, under the supervision of Jesper Mørk and Bjarne Tromborg both at the nanophotonics group.

We would like to acknowledge our supervisors for their continuous and patient support and constructive advice throughout the project. We have been given an introduction to the field of nanophotonics, which has been very exciting.

The level in this report is aimed at students at approximately the same level as our own. This includes basic knowledge on electromagnetism, quantum mechanics, semiconductor physics, and numerical analysis. The basics of these areas has not always been enough and literature studies in more advanced topics have been needed. Hence some of the derivations are quite thorough which represents our efforts in understanding the new theory. On the other hand, the report does not entirely resemble the time spent on the individual topics. Much time and effort has been given into exploring the strengths and weaknesses of FEMLAB, which in the end did not fulfill all our needs sufficiently.

Part of the steady state analysis is based on two papers by Chang-Hasnain *et al.* and the notation adopted in this report is greatly inspired by these.

In the end we would like to thank Jørn M. Hvam (Research Center COM) for aiding in the absence of our supervisors, and Per Grove (Informatics and Mathematical Modelling) for suggesting the spectral method for solving the full dynamic system. Many grammatical and linguistic errors have been avoided by the proofreading of Solveig Christensen, who we owe a lot to.

Henri Nielsen and Per Nielsen
Lyngby, DTU – 28th June 2005

Contents

1. Introduction

In this report we deal with two main topics. The main part will be the analysis of slow-light attained through electromagnetically induced transparency (EIT) in an InAs semiconductor quantum dot in GaAs bulk material; both in the steady state solution of the Bloch equations and in the dynamic case when the full light-matter interaction of the Bloch and Maxwell equations is included. A smaller part will deal with the numerical calculations of the transition matrix elements for the optical transitions considered in the quantum dots.

In recent years, great interest has been given to ideas on how to slow down the effective speed of light in an easy and controllable way. If this is achieved it would address many issues in connection with future optical networks.

Today, almost all modern communication is transferred in optical fibres and converted into electrical form when in need of being processed or switched. This conversion is time-consuming and the achievable bandwidth is limited by the conversion and signal processing capacity of the electrical equipment. To overcome this limit, great effort has been put into developing all-optical processing and switching systems. These systems have been demonstrated, though one of the critical key components, a controllable optical buffer which has the ability to delay a light signal, is still missing [1].

The obvious approach is to control the group velocity, $v_{\mathrm{g}} = \frac{c}{n_{\mathrm{g}}}$, in a material through the altering of the refractive group index, n_{g}. Different means to obtain a large refractive group index exist and have been demonstrated by different groups. Amongst the most interesting are population oscillations in quantum wells (PO) by which a refractive group index of more than 31000 has been demonstrated experimentally, photonic crystal filters and electromagnetically induced transparency (EIT) [2].

Electromagnetically induced transparency is probably best know as Lene Hau *et al.* utilized this effect in a ultra cold Bose-Einstein condensate. This was done at 900 nK and slowed a 1 km light pulse down to 17 m/s, and they later managed to stop a light pulse for almost a millisecond [3]. This was an important result and has clarified the potential of EIT. However the used technology is not well suited for the future applications in optical buffers, simply by the fact that gas needs to be cooled to just above 0 K in ultra high vacuum and the gas cloud has to be held in a magnetic trap. Which all complicates matter a lot and it is therefore desirable to find an alternative solution.

To achieve EIT one needs a discrete three-level system in which a strong coupling laser couples two out of the three states. The effect is to make it possible for a weak probe laser to propagate through the material like it was transparent and at the same time experience a high refractive group index. This occur for frequencies where it would normally be subjected to high absorption.

One way of obtaining a discrete three-level system is to use quantum dots. These are nanoscale structures in which the electrons are confined in all three dimensions and the QDs exhibit 0D

electronic behavior. The electron energy levels become discrete and the quantum dots effectively behave like super atoms. By choosing three of the discrete levels, in our case the highest in the valence band and the two lowest in the conduction band, we can use them to obtain EIT and slow-light. In this report we consider InAs semiconductor quantum dots packed in a GaAs bulk material. One way to make these is by surface deposition of a few nanometer thin layer (wetting layer) of In and As atoms on a GaAs semiconductor. In the interface, the crystal structures will try to adjust and due to the small difference in lattice parameter (GaAs: 5.65 Å and InAs: 6.05 Å) surface tension in the wetting layer produces self-assembled quantum dots, randomly distributed. This is called the Stranski-Krastanow growth technique.

In this report we present two different analyses for simulating the slow-light effect through a material consisting of homogeneously aligned quantum dots. In the first case we examine for both the coupling and probe fields being continuous waves. This is done by solving the Bloch equations in steady state which can be done analytically. This allows us to calculate the complex susceptibility and predict how a low intensity continuous electromagnetic wave will propagate through the material. This has been extensively studied in a number of papers [1, 4] and a refractive group index of the order 10^3 has been obtained which is well suited for 40 Gb/s optical systems.

This approach does not take into account the full dynamic of the electromagnetic pulse propagating through the material. The light-matter interaction is coupled. The induced dipoles from the electromagnetic pulse in the material, interfere with the electromagnetic pulse itself. Therefore, both the material and the wave are altered along the way. This implies that the front of the pulse experience a different material compared to the back, or that several pulses can interfere. These considerations have been taken into account in the second analysis. In this we have made a full simulation of pulses propagating through a quantum dot material by solving the dynamically coupled Bloch and Maxwell equations. To our knowledge, this has not been done previously in relation to the study of slow-light.

2. Electromagnetically Induced Transparency

The effect utilized in this report, to slow down light, is called electromagnetically induced transparency (EIT)[1]. It is a quantum phenomenon which allows an electric field, resonant with a transition, to propagate transparently through a medium in which it normally would feel a strong absorption. Furthermore, the field would see a high refractive group index, hence being slowed down.

To obtain slow-light by EIT, an atomic system containing at least three discrete atomic states and two laser fields are needed. A coupling laser which controls the EIT effect and the amount of slow down and a probe laser which is the one we want to slow down. Both lasers must be resonant (or near resonant) with a dipole allowed transition in the medium and the last transition we shall take as dipole forbidden. To achieve EIT it is required that the coupling field is much stronger than the probe field.

Figure 2.1 shows different setups to obtain EIT and to simplify the description we only consider the ladder scheme. We label the three eigenstates $|1\rangle$ (the ground state), $|2\rangle$, and $|3\rangle$ corresponding to increasing energy. The coupling field connects $|2\rangle$ and $|3\rangle$ and the probe field couples $|1\rangle$ and $|2\rangle$.

If we only turn on the coupling field the $|2\rangle$ and $|3\rangle$ states are no longer eigenstates of the total system. Each one gets split up in two new dressed states and the splitting is proportional to the field strength, or almost equal twice the Rabi frequency, see figure 2.2.

When the probe laser is turned on (assumed to be weak), it is only a small perturbation and does not alter the eigenstates of the system. The probe laser no longer match any transition to either of the new dressed $|2\rangle$ states. In the case of zero linewidth it does not interact with $|2\rangle$ at all and for finite linewidth the effect is cancelled due to destructive quantum interference between the two transitions. This implies that the carriers are trapped in the ground state, so called coherent

[1] Excellent reviews of EIT are given in [1, 3, 5, 6] from which we have been inspired.

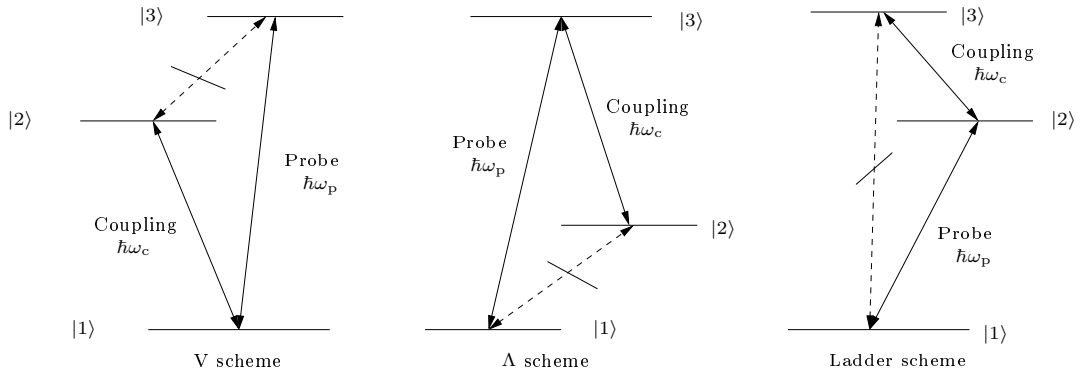

Figure 2.1.: *Different schemes for obtaining EIT*

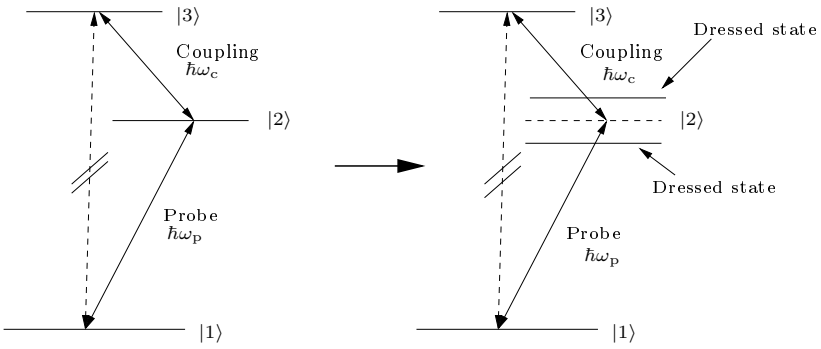

Figure 2.2.: *The principle of EIT*

population trapping, and no absorption of the probe laser occur. The probe field then propagates through the medium as if it was transparent.

Another description can be given in terms of the absorption and dispersion curves for the probe, which are related to the imaginary and real part of the complex susceptibility, $\tilde{\chi} = \chi' + i\chi''$, respectively. The absorption is approximately proportional to χ'' and the refractive group index is approximately proportional to the slope of χ'. In the case where we turn off the coupling field, the two curves look like figure 2.3(a) with a high absorption at resonance, characteristic of a normally absorbing material. When the coupling field is on the splitting of the $|2\rangle$ state is seen in the absorption spectrum as an spectral window, see figure 2.3(b). The linewidth of the absorption peaks is related to the decay rates of the $|1\rangle \leftrightarrow |2\rangle$ and $|1\rangle \leftrightarrow |3\rangle$ dipoles[2].

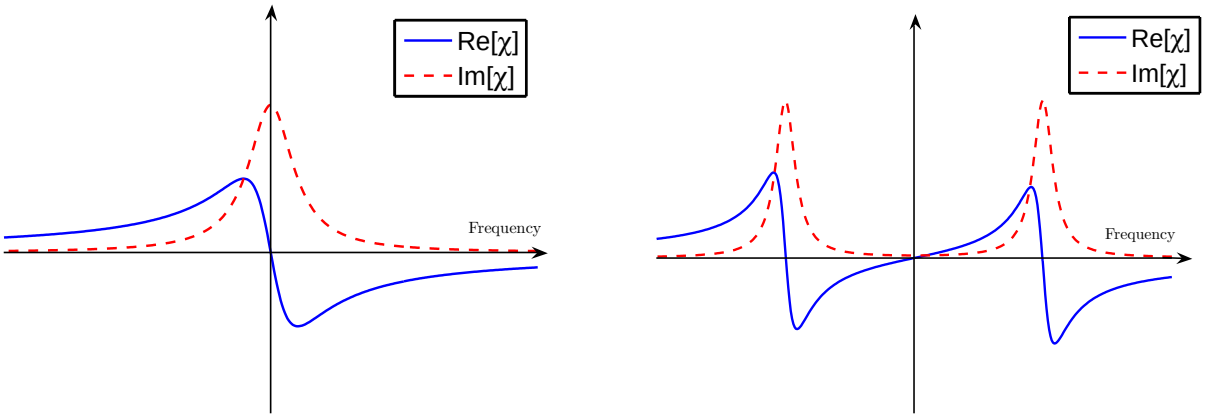

(a) $\tilde{\chi}$ for a normal material

(b) $\tilde{\chi}$ in the EIT state

Figure 2.3.: *The real and imaginary part of the complex susceptibility seen by a probe laser. This shows how the absorbance and the dispersion are related in a normal material (left figure) and under influence of EIT (right figure). The characteristic splitting of the $|2\rangle$ state in EIT is clearly seen.*

The Kramer-Kronig relations, which relate the real and imaginary parts of a complex analytical function, imply that χ' and χ'' should behave like each others derivatives. An extremum in χ'' means that χ' has to pass through zero. At resonance in the middle of the absorption window, this gives rise to a slope which is positive and corresponds to a large refractive group index.

[2]The $|1\rangle \leftrightarrow |3\rangle$ transition is not a directly dipole allowed transition, but is a kind of pseudo-dipole.

3. Semiconductor Quantum Dots

The goal of this chapter is to calculate the transition matrix elements defined in section 5.4, $\mu_{nm} = e\langle n|y|m\rangle$, for an InAs QD embedded in a GaAs bulk. First we discuss a few properties of semiconductors and semiconductor QDs and mention the envelope approximation used to describe localized states in semiconductor QDs. Our QD model will be presented and various parameters will be described. Actual calculations have been performed in the finite element package FEMLAB[1], as these could not be dealt with analytically. The results of the numerical calculations will be presented throughout the chapter.

3.1. Introduction

The following will be a short introduction to the semiconductors GaAs and InAs, as these are ones we will use in our QD system. In figure 3.1 the band structures of GaAs and InAs are shown for two directions in **k**-space in the vicinity of the Γ point. Both semiconductors are well suited for optical transitions, having a direct gap at Γ and a well defined effective mass of both valence bands and conduction band. However, these band structures are for bulk materials and we are going to deal with structures in nanometer regime. When downsizing the continuous nature of the band structures will become discrete due to new boundary conditions. The discrete energies of the heavy and light holes will split, due to the large difference in effective mass. The light hole states have the lightest mass and thus their highest energy will be much lower than the heavy hole states of interest. Here it is implicitly assumed that the QDs are large compared to the atomic unit cells, so that their bulk material parameters can still be used. Throughout the report we will continue to refer to bands when states of different effective mass are discussed, even though this is not entirely correct.

The energy gap of GaAs is about four times that of InAs. This means that if you embed InAs QDs in a GaAs bulk, band bending will create a confining potential for the electrons in the InAs QDs. This idea is illustrated in figure 3.3. It is transitions between these bound states we will consider. A quantum mechanical description of the bound states involves the so-called envelope approximation, which we will describe next.

Electron states in bulk semiconductors are Bloch states of the form

$$\psi_{\mathbf{k}}(\mathbf{r}) = e^{i\mathbf{k}\cdot\mathbf{r}} u_{\mathbf{k}}(\mathbf{r}).$$

These are however delocalized throughout the crystal and hence a single of these cannot be used to describe a bound state. We can consider a linear combination of Bloch states, as done by [7], to describe our bound states

$$\psi(\mathbf{r}) = \int A(\mathbf{k}) e^{i\mathbf{k}\cdot\mathbf{r}} u_{\mathbf{k}}(\mathbf{r}) d\mathbf{k},$$

[1] http://www.comsol.com/

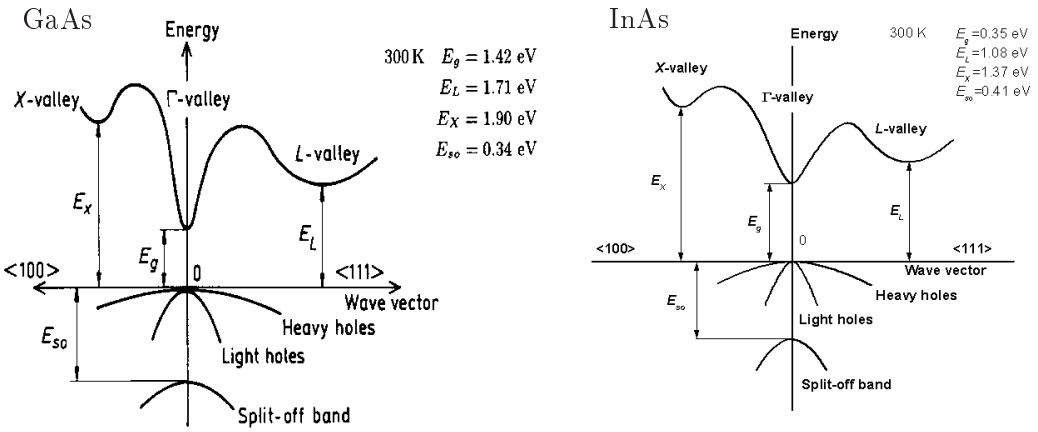

Figure 3.1.: *These two figures illustrate the energy band structure, in the vicinity of the* Γ *point. To the left is the band structure for GaAs and to the right for InAs. Source:* `http://www.ioffe.ru/SVA/NSM/Semicond/`

where $A(\mathbf{k})$ are the expansion coefficients. If we assume that near the band edge $u_{\mathbf{k}}(\mathbf{r})$ does not depend strongly on $\mathbf{k}$. Then we can put $\mathbf{k} = \mathbf{0}$ and take $u_{\mathbf{0}}(\mathbf{r})$ outside the integral and obtain

$$\psi(\mathbf{r}) = u_{\mathbf{0}}(\mathbf{r}) \int A(\mathbf{k}) e^{i\mathbf{k}\cdot\mathbf{r}} d\mathbf{k}.$$

The remaining integral we will term, the envelope function. By defining $u_{\mathbf{0}}(\mathbf{r}) \equiv u(\mathbf{r})$ we end up with

$$\psi(\mathbf{r}) = u(\mathbf{r})F(\mathbf{r}). \tag{3.1}$$

It turns out, as discussed in [8, App. 8], that we do not need to determine the Bloch functions (the u's) explicitly as their general properties are described in the literature. Thus we are left with determining the envelope functions. The equation for obtaining these functions is a Schrödinger-like equation that reads:

$$\left[-\frac{\hbar^2}{2}\nabla \cdot \left(\frac{1}{m^*(\mathbf{r})}\nabla\right) + V(\mathbf{r})\right] F(\mathbf{r}) = EF(\mathbf{r}), \tag{3.2}$$

where $V(\mathbf{r})$ is the confining potential due to the band bending and $m^*(\mathbf{r})$ is the effective mass of the respective band, possibly dependent on position. It should be noted that in taking the envelope approach, we neglect a lot of real physical effects. One of the most pronounced effects is the development of strain in the QDs buried in the GaAs bulk. This affects their crystal structure and hence their band structure which ultimately changes the effective mass. The excitons that appear when you excite an electron are also completed neglected and so are all other many-body effects. Due to the simple approach, the calculated results should only be considered as crude approximations to their real values. In the next section we consider more explicitly the details of our QD.

3.2. Modelling

We wish to consider QDs grown using the Stranski-Krastanow technique. In this technique, one deposits a very thin layer, the wetting layer (WL), of InAs on a GaAs surface. Due to the lattice

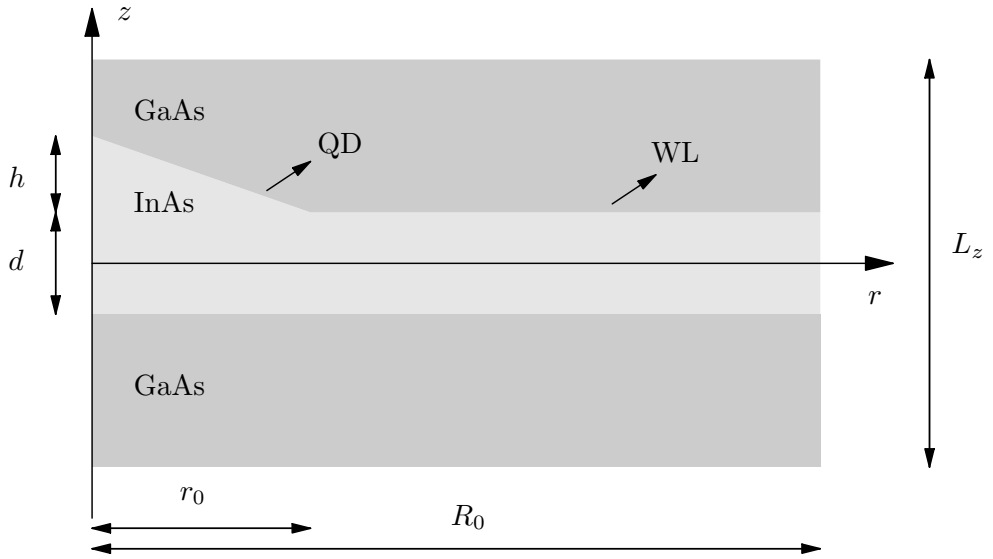

Figure 3.2.: *Schematic illustration of the rotation symmetric QD and wetting layer. Different parameters used in the modelling are shown.*

mismatch between these two crystals, surface tension will build in the WL and eventually small pyramid-like structures will appear on the GaAs surface. The formation of the QDs are due to the WL wanting to minimize its surface energy. On top of the WL and QDs a new layer of GaAs is now deposited and you start over. The result is a layered structure consisting of WLs and QDs of InAs embedded in GaAs bulk. This is the setup we want to describe.

In order to simplify the modelling we will only consider a single QD, containing a single electron, on an infinite WL. Further we will assume that the entire setup has rotational symmetry around the symmetry axis of the QD, allowing us to reduce the full 3D case to an effective 2D description. The shape of the QD does not allow us to solve the envelope equation analytically, so we are forced to adopt numerical methods for solving the problem. Due to the numerical implementation we cannot have infinite WL or GaAs bulk. So bounded dimensions of these have been introduced. A schematic illustration of the QD/WL/bulk system is presented in figure 3.2.

The specific states we wish to consider are the two first[2] electron states in the conduction band and the last electron state in the valence band, or heavy hole band. These states are depicted in figure 3.3 along with other quantities. The bound electron states in the flipped potential in the heave hole band are trapped there due to the Pauli principle. This prohibits them to go to a lower energy state, as they are occupied. Instead of treating electrons in the heavy hole band, we will consider holes as this is simpler. The holes will act as electrons do in a normal potential well, basically as bubbles seeking to the top of the flipped potential well. The cost of treating holes instead of electrons, is that we have to flip the energy axis.

[2]By first we mean the two first for which we can make transitions between. The selection rules for these transitions are discussed later in this chapter and in appendix A.3.

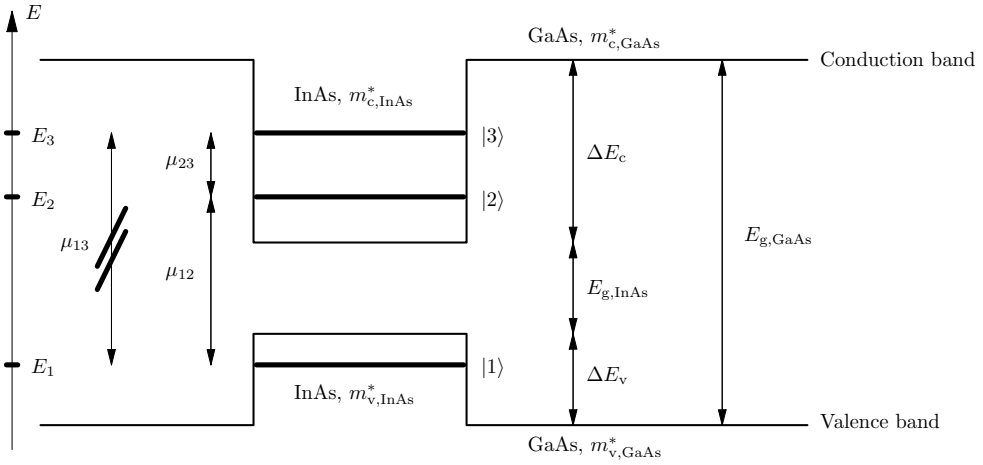

Figure 3.3.: *Schematic illustration of the band structures along a arbitrary direction through the InAs QD embedded in the GaAs bulk. Various parameters are indicated.*

3.2.1. The envelope equation

The rotational symmetry makes cylindrical coordinates a natural choice, from now on we use the coordinates (r, z, φ). Having symmetry, suggest that we can separate the envelope function in an angular part, depending on φ, and a part depending on r and z, so that: $F(\mathbf{r}) = \frac{1}{\sqrt{2\pi}} e^{im\varphi} f(r, z)$.

Solutions of the envelope equation must everywhere be continuous and differentiable along a direction given by a unit vector $\hat{\mathbf{n}}$. With a position dependent effective mass this can be stated mathematically as

$$F(\mathbf{r}), \tag{3.3}$$

$$\frac{1}{m^*(\mathbf{r})} \hat{\mathbf{n}} \cdot \nabla F(\mathbf{r}), \tag{3.4}$$

both being continuous at every point. From the continuity condition, eq. (3.3), and the fact that a rotation by 2π brings you back to the same point, we get the condition for m: $e^{im2\pi} = 1$ from which it follows that m must be an integer or zero. Inserting this separated solution into eq. (3.2) we [9] obtaining the following equation for f:

$$\left[-\frac{\hbar^2}{2r} \frac{\partial}{\partial r} \left(\frac{r}{m^*} \frac{\partial}{\partial r} \right) - \frac{\hbar^2}{2} \frac{\partial}{\partial z} \left(\frac{1}{m^*} \frac{\partial}{\partial z} \right) + \frac{\hbar^2 m^2}{2 m^* r^2} + V(r, z) \right] f = Ef, \tag{3.5}$$

where we have used that $m^* = m^*(r, z)$.

Our eigenvalue problem is not solvable until we specify appropriate boundary conditions for the domain. This will be discussed with the notation introduced in figure 3.2.

First we consider boundaries for which $r \neq 0$. We are interested in states mainly bound to the QD and we expect that the probability density, and hence the envelope function, will decay exponentially in the GaAs bulk surrounding it. It is thus fair to assume that if we set L_z to a large value compared to the QD, we can choose the horizontal domain boundaries at $z = \pm L_z/2$ equal to zero:

$$f(r \neq 0, \pm L_z/2) = 0.$$

At the boundary at $r = R_0$ the situation is a bit different due to the thin slap of WL. Here we cannot expect the same exponential decay as in the bulk, as the WL is InAs also. However for this particular calculation we are only interested in the ground and possibly the first excited state, so we will assume that the energy of these states is low enough for them to still be reasonably confined in the QD. Therefore, if we set R_0 to a large value compared to r_0 we can safely adopt zero boundary conditions for this domain edge too:

$$f(r = R_0, z) = 0.$$

The second boundary condition in r, at $r = 0$, has to be treated a bit more carefully, as it depends on m. First we consider the case where $m = 0$. F now becomes independent of φ and hence the directional derivative along[3] $\hat{\mathbf{r}}$, eq. (3.4), has to be zero at $r = 0$ or else F will not be differentiable on the z-axis. For $m \neq 0$ we consider a transition through the z-axis, for which the angle changes from say α to β, from eq. (3.3) we get the condition: $f(r = 0, z)e^{im\alpha} = f(r = 0, z)e^{im\beta}$, if this has to be valid for any α, β, and z we have to require that $f(r = 0, z) = 0$. Summarizing the boundary conditions at $r = 0$,

$$f(r = 0, z) = 0, \quad m \neq 0$$
$$\frac{\partial f(r = 0, z)}{\partial r} = 0, \quad m = 0.$$

The internal boundaries when going from one material to another are subjected to the general conditions eq. (3.3) and (3.4). For notational simplicity we define the domain describing the InAs material in figure 3.2 as $\mathbb{D}_{\mathrm{InAs}}$ and $\mathbb{D}_{\mathrm{GaAs}}$ for GaAs. For each band we now have a standard particle-in-a-box problem (when treating holes in the valence band), where the potential for a band j ($j = c, v$) is given by,

$$V(r, z) = \begin{cases} 0 & , \quad \mathbf{r} \in \mathbb{D}_{\mathrm{InAs}} \\ \Delta E_{\mathrm{j}} & , \quad \mathbf{r} \in \mathbb{D}_{\mathrm{GaAs}}, \end{cases}$$

and the position dependent effective mass is given by

$$m^*(r, z) = \begin{cases} m^*_{\mathrm{j,InAs}} & , \quad \mathbf{r} \in \mathbb{D}_{\mathrm{InAs}} \\ m^*_{\mathrm{j,GaAs}} & , \quad \mathbf{r} \in \mathbb{D}_{\mathrm{GaAs}}. \end{cases}$$

The different quantities are shown in figure 3.3. When solving eq. (3.5) with the set of boundary conditions above, the eigenenergy will be quantized and can be labelled by a set of quantum numbers. The angular quantum number m has already been introduced. As m appears squared in eq. (3.5), the same energy will be obtained for $\pm m$, hence the energy is two times degenerate for $m \neq 0$. To label the solutions we introduce a quantum number, n, for r and z dimensions. The energy will not be degenerate in n, as the only symmetry is connected to m. Eq. (3.5) is associated with a specific band, so in order to completely specify an envelope function, a band indication is needed too. We will use j ($j = c, v$) as a superscript to show which band we are talking about. An envelope function, with quantum numbers (j, n, m), will thus have the form

$$F^j_{nm}(\mathbf{r}) = \frac{1}{\sqrt{2\pi}} e^{im\varphi} f^j_{nm}(r, z), \tag{3.6}$$

and when being properly normalized it will satisfy the orthonormality relation, $\langle F^j_{n'm'} | F^j_{nm} \rangle = \delta_{n'n}\delta_{m'm}$, within a single band. When used with the Bloch function, eq. (3.1), for band j it will satisfy the orthonormality relation, $\langle u^{j'} F^{j'}_{n'm'} | u^j F^j_{nm} \rangle = \delta_{j'j}\delta_{n'n}\delta_{m'm}$, between bands.

[3] This is the vector given by: $\hat{\mathbf{r}} = \cos\varphi\hat{\mathbf{x}} + \sin\varphi\hat{\mathbf{y}}$

Quantity	Symbol	Value	Unit
Height of numeric domain	L_z	40	nm
Radius of numeric domain	R_0	100	nm
Radius of QD	r_0	9	nm
Band gap of GaAs	$E_{\mathrm{g,GaAs}}$	1.424	eV
Band gap of InAs	$E_{\mathrm{g,InAs}}$	0.359	eV
Conduction potential depth	ΔE_{c}	0.697	eV
Valence potential depth	ΔE_{v}	0.368	eV
Effective mass for GaAs in conduction band	$m^*_{\mathrm{c,GaAs}}$	0.0665	m_e
Effective mass for GaAs in valence band	$m^*_{\mathrm{v,GaAs}}$	0.38	m_e
Effective mass for InAs in conduction band	$m^*_{\mathrm{c,InAs}}$	0.027	m_e
Effective mass for InAs in valence band	$m^*_{\mathrm{v,InAs}}$	0.34	m_e

Table 3.1.: *Fixed parameters used in the numerical solution of the bound QD states.*

3.3. Numerical solutions

As mentioned, we cannot solve the envelope equation analytically and have to use numerical methods. This requires us to specify numerical values for all parameters used. In this section all calculations will be performed for fixed parameters, except for h and d the height of the QD and WL respectively. The values for the fixed[4] parameters are summarized in the table 3.1.

The equation for f described above has been implemented and solved in FemLab. In figure 3.4 we have illustrated a few radial probabilities for $h = 7$ nm and $d = 1.25$ nm. This will be our standard QD setup used in all calculations in the chapters to come. Figure 3.4(a) shows the radial probability for the first excited hole state in the valence band, with quantum numbers $(v, 1, 0)$. The state is nicely confined within the QD and many of the further excited states will also remain bound in the QD due to the large effective mass of the heavy hole band, decreasing the energy spacing between two states. In figure 3.4(b) the first excited state, $(c, 1, 0)$, of the conduction band is shown, this state also remains bound to the QD. The state $(c, 1, \pm 1)$ is shown in figure 3.4(c). Here we clearly see that the state is less confined within the QD, than the prior states were. A few energy levels above this the electron would have escaped into the WL. Here it would essentially become delocalized in the, in principle infinite, WL and be part of the continuum of energy states.

Even though we are not interested in the unbound WL states, we will briefly discuss this transition from the bound QD states to the unbound WL states. In figure 3.5(a) we have calculated an energy diagram[5] for our reference QD for both the conduction and valence band. However, the discussion will be restricted to the conduction band, as WL states will not be a problem in the valence band, but basically the same applies.

It is noticeable how the concentration of blue dots (density of states) increases very rapidly near the thin dashed line. This is due to the fact that the energy of the state has become too high

[4] The energies and effective masses are all at 300 K.

[5] This diagram should also show the negative values of m, but this would simply be a mirror picture of the part we show and hence we consider only positive m's.

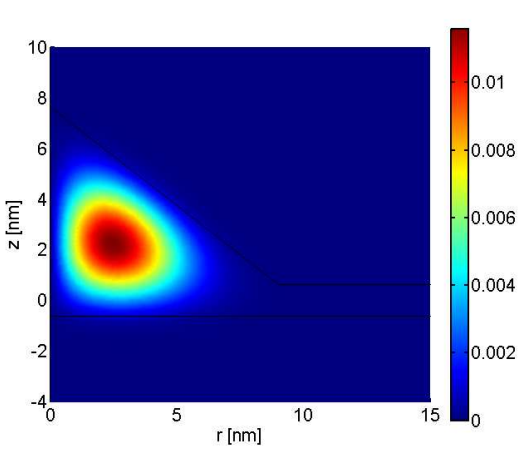

(a) Radial probability of f^v_{10}, $E_1 = 0.332$ eV.

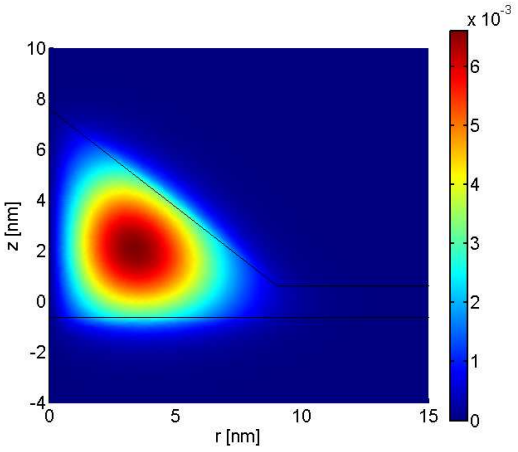

(b) Radial probability of f^c_{10}, $E_2 = 0.967$ eV.

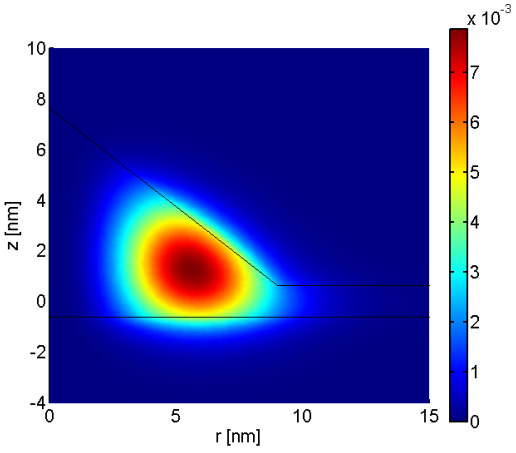

(c) Radial probability of $f^c_{1\pm1}$, $E_3 = 1.112$ eV.
Both $m = \pm 1$ give the same f.

Figure 3.4.: *The radial probability, $|f^j_{nm}(r,z)|^2 r$, for the envelope part the states $|1\rangle$, $|2\rangle$ and $|3\rangle$. The actual calculation domain is truncated for clarity. This particular dot has $d = 1.25$ nm and $h = 7$ nm, this will be our reference dot for other calculations throughout the report. The energies stated are with reference to the GaAs valence band edge.*

for it to be confined in the QD. It enters the WL, which in principle is infinite and no confining takes place. The energy spectrum becomes continuous and the states delocalized in the entire WL. Figure 3.5(b) shows the small rectangle in figure 3.5(a) magnified to be able to separate a few states. Figure 3.5(c) is a plot of the radial probability of the state $(c, 2, 0)$. It is clear that this state is still pretty much confined to the QD, while not as clearly confined as the states depicted in figure 3.4. Moving to the states $(c, 3, 0)$ and $(c, 4, 0)$, these have a very small energy separation and hence we would suspect them to be part of WL continuum. The figures 3.5(d) and 3.5(e) show that this is the case. These states are clearly not bound to the QD and will not be used in calculating the transition matrix elements in the next section.

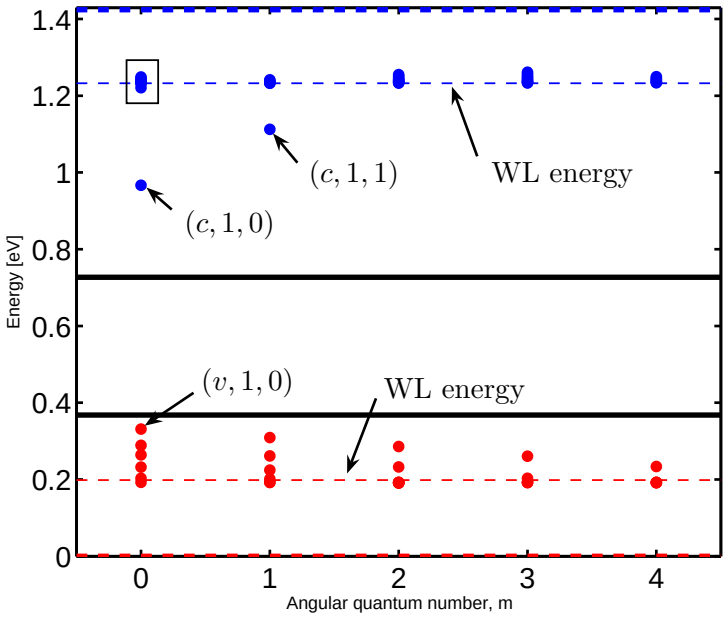

(a) Energy diagram for the eigenstates, the blue part corresponds to the conduction part and the red part to the valence part. A few states are indicated by their quantum numbers and the thin dashed lines indicate the onset of the WL continuum. These calculations are done for our reference dot.

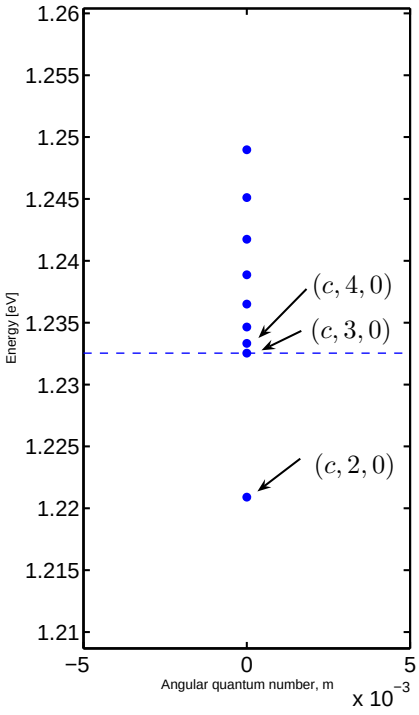

(b) Magnified part of the conduction band energies near the WL energy. A bound state, $(c,2,0)$, is indicated and two unbound WL states, $(c,3,0)$ and $(c,4,0)$.

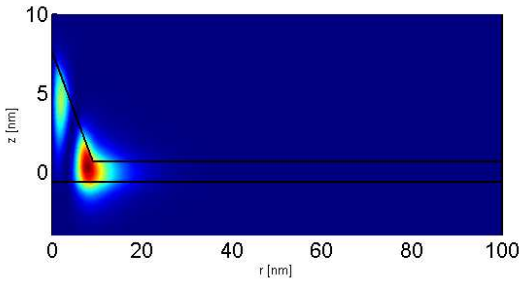

(c) Radial probability of the bound state $(c,2,0)$ from figure 3.5(b).

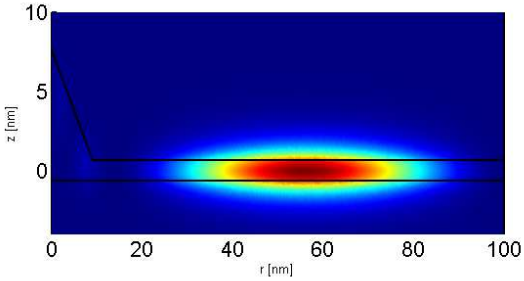

(d) Radial probability of the WL state $(c,3,0)$ from figure 3.5(b).

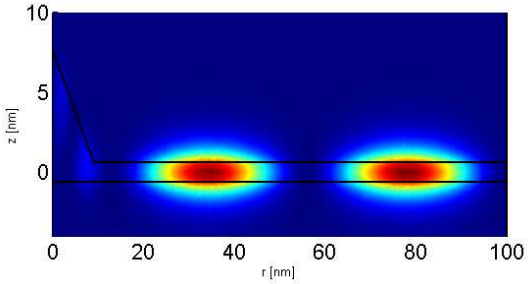

(e) Radial probability of the WL state $(c,4,0)$ from figure 3.5(b).

Figure 3.5.: *Energy diagrams and three states indicating the transition from bound QD states to unbound WL states.*

3.4. Transition matrix elements

Having solved the envelope equation and found its eigenstates, we now turn to the main subject of this chapter; the calculation of the transition matrix elements μ_{12} and μ_{23}, between the states defined in figure 3.3. We split the calculation in two parts, as the two transitions are different in nature. The $|1\rangle \leftrightarrow |2\rangle$ transition occurs between the valence and conduction band and hence it is called an interband transition. The $|2\rangle \leftrightarrow |3\rangle$ transition occurs within the conduction band alone and is called an intraband, or intersubband, transition.

The main difference between the states in the two bands is that the Bloch functions are not the same. As we recall from eq. (3.1), the full form of a state in a band is described by the product between a Bloch and an envelope function. This means that the transition matrix element, divided by e, between two states $|A\rangle$ and $|B\rangle$, in band a band b respectively, will be of the form

$$\langle A|y|B\rangle = \langle u^a F^a_{nm}|y|u^b F^b_{n'm'}\rangle \,. \tag{3.7}$$

This expression is general and will be applied to both the interband and intraband transition considered below.

3.4.1. Interband transitions

The transition $|1\rangle \leftrightarrow |2\rangle$ corresponds to $(v,1,0) \leftrightarrow (c,1,0)$. Inspecting figure 3.5(a), we notice that the states $(v,1,0)$ and $(v,1,\pm 1)$ are quite closely spaced energy wise. Thus you could expect that light with a photon energy of approximately E_{32} would couple to all these valence states. However, it turns out as described in appendix A.3 that the $(v,1,0) \leftrightarrow (v,1,\pm 1)$ is not dipole allowed. This means that we only have to consider the $(v,1,0) \leftrightarrow (c,1,0)$ transition.

Using eq. (3.7) we write the transition matrix element for the $|1\rangle \leftrightarrow |2\rangle$ transition as

$$\langle 1|y|2\rangle = \langle u^v F^v_{10}|y|u^c F^c_{10}\rangle \,.$$

This matrix element is approximately equal to [8, p. 120]

$$\langle 1|y|2\rangle \approx \langle u^v|y|u^c\rangle \langle F^v_{10}|F^c_{10}\rangle = M \langle F^v_{10}|F^c_{10}\rangle \,, \tag{3.8}$$

where $M \equiv \langle u^v|y|u^c\rangle$. The quantity M we are not able to calculate within our model, as it involves the lattice periodic Bloch functions. Luckily we do not need to, as this material parameter can be looked up in tables. An approximate expression for $|M|$ has been derived in appendix A.3 and the result is,

$$|M| = \frac{0.699}{(\omega_{\mathrm{p}}[\mathrm{fs}^{-1}])} \text{ nm.} \tag{3.9}$$

$|M|$ is dependent on the probe field frequency and hence a field composed of several frequency components would each have their own $|M|$. For simplicity we have only calculated $|M(\omega_{\mathrm{p}} = \omega_{21})|$, $\omega_{21} = (E_2 - E_1)/\hbar$, and will use this even though we do not always consider single frequency fields. This is justified whenever the width of the frequency distribution is much smaller than the carrier frequency.

The remaining overlap integral between the two envelope functions can be calculated within our model. Using eq. (3.6) we can write the explicit expression for the overlap integral,

$$\langle F^v_{10}|F^c_{10}\rangle = \frac{1}{2\pi}\int [f^v_{10}]^* f^c_{10} r dr dz d\varphi = \int [f^v_{10}]^* f^c_{10} r dr dz. \tag{3.10}$$

This is the integral we will be calculating using the numerical solutions obtained in FemLab.

3.4.2. Intraband transitions

The transition $|2\rangle \leftrightarrow |3\rangle$ corresponds to $(c,1,0) \leftrightarrow (c,1\pm 1)$. From figure 3.5(a) we see that $(c,2,0)$ has a relatively high energy compared to $(c,1,\pm 1)$. However a situation where the energy of these two states were comparable could occur. In this case we would have to worry about the electron making the transition to $(c,2,0)$ instead of that to $(c,1,\pm 1)$. This transition is however not allowed due to the selection rules discussed in appendix A.3 and we can concentrate on the transition to $(c,1,\pm 1)$.

The energy of the states $(c,1,\pm 1)$, E_3, is two times degenerate. Hence the angular part of the envelope function is spanned by the two functions $\frac{1}{\sqrt{2\pi}}e^{\pm i\varphi}$. To simplify the description we choose[6] a new basis for the angular part given by:

$$\Phi^+ = \frac{1}{\sqrt{\pi}}\frac{1}{2}\left(e^{i\varphi}+e^{-i\varphi}\right) = \frac{1}{\sqrt{\pi}}\cos\varphi,$$
$$\Phi^- = \frac{1}{\sqrt{\pi}}\frac{1}{2i}\left(e^{i\varphi}-e^{-i\varphi}\right) = \frac{1}{\sqrt{\pi}}\sin\varphi,$$

being orthonormal. This change of basis essentially decouples the transition to one of the degenerate states, such that its transition matrix element is zero. From eq. (3.7) the two matrix elements are

$$\langle 2|y|3^\pm\rangle = \left\langle u^c \frac{1}{\sqrt{2\pi}} f^c_{10} \middle| y \middle| u^c f^c_{11}\Phi^\pm \right\rangle,$$

which can be [4] approximated by

$$\langle 2|y|3^\pm\rangle \approx \underbrace{\langle u^c|u^c\rangle}_{=1} \frac{1}{\sqrt{2\pi}} \langle f^c_{10}|y|f^c_{11}\Phi^\pm\rangle . \tag{3.12}$$

We start by calculating $\langle 2|y|3^+\rangle$, as this will turn out extremely simple, which is given by

$$\langle 2|y|3^+\rangle = \frac{1}{\sqrt{2\pi}}\langle f^c_{10}|y|f^c_{11}\Phi^+\rangle = \frac{1}{\sqrt{2\pi}}\int \cos\varphi\sin\varphi d\varphi \int [f^c_{10}]^* f^c_{11} r^2 dr dz.$$

Sine and cosine are orthogonal functions and hence the integral over these is zero and $\langle 2|y|3^+\rangle = 0$ as intended. For $\langle 2|y|3^-\rangle$ we write

$$\begin{aligned}\langle 2|y|3^-\rangle &= \frac{1}{\sqrt{2\pi}}\langle f^c_{10}|y|f^c_{11}\Phi^-\rangle = \frac{1}{\sqrt{2\pi}}\int \sin^2\varphi d\varphi \int [f^c_{10}]^* f^c_{11} r^2 dr dz \\ &= \frac{1}{\sqrt{2}}\int [f^c_{10}]^* f^c_{11} r^2 dr dz.\end{aligned} \tag{3.13}$$

By construction the only contribution comes from $\langle 2|y|3^-\rangle$ and we define: $\mu_{23} \equiv e\langle 2|y|3^-\rangle$. The integral above can be calculated from the solutions acquired from FemLab.

[6] How to choose your basis cleverly depends, amongst other things, on how your electric field is polarized.

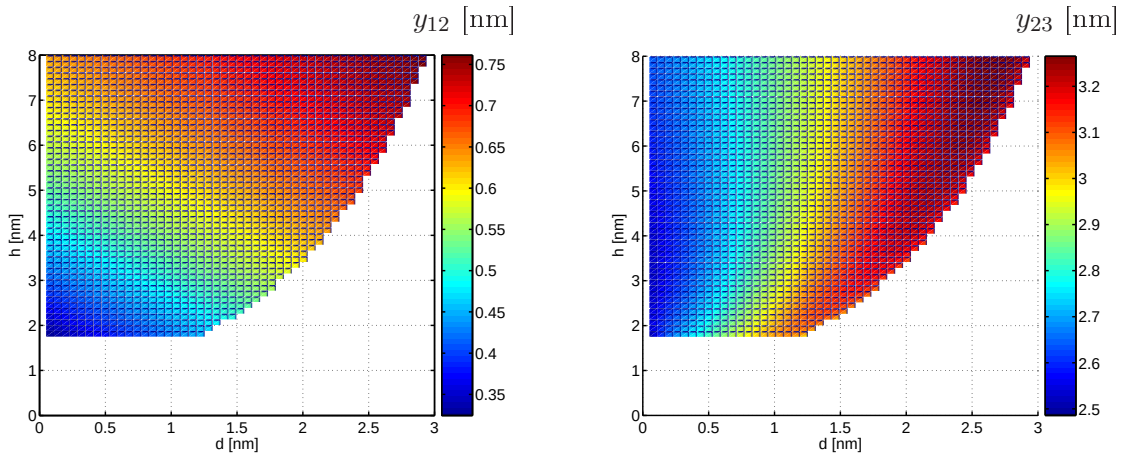

(a) Calculation of μ_{12}/e according to eq. (3.14a).

(b) Calculation of μ_{23}/e according to eq. (3.14b).

Figure 3.6.: *These figures show the calculation of y_{12} and y_{23} for a variety of QD sizes, $d \in [0\ 3]$ nm and $h \in [2\ 8]$ nm. The cut-off in the values is where $|3\rangle$ has become a WL state.*

3.4.3. Numerical calculation of the transition matrix elements

In the two previous sections we derived the integrals for the transition matrix elements we set out to find. Using the equations (3.9), (3.10) and (3.13) we can sum up what we are to calculate,

$$\mu_{12} = e\,\langle 1|y|2\rangle = e|M(\omega_{\mathrm{p}} = \omega_{21})| \int [f_{10}^{v}]^{*}\, f_{10}^{c} r dr dz \tag{3.14a}$$

and

$$\mu_{23} = e\,\langle 2|y|3^{-}\rangle = e\frac{1}{\sqrt{2}} \int [f_{10}^{c}]^{*}\, f_{11}^{c} r^{2} dr dz. \tag{3.14b}$$

The results of these integrals are illustrated in figure 3.6. Transition matrix elements where $|3\rangle$ is part of the WL continuum has been cut off the plots. The reason for this is that when making transitions to a continuum of states, our simple integrals do not yield the the correct value and you need some sort of Fermi's Golden Rule expression. The transition matrix elements we have calculated are in excellent agreement with the values stated in [1, 4].

4. Classical Electromagnetic Theory

The light-matter interaction in this report is described by a semiclassical model. In it, the quantum dot material is modelled by a quantum mechanical description and the electromagnetic field is described by the classical electromagnetic wave theory. Here we present some of the main results and definitions which will be using later.

4.1. The wave equation in matter

The propagation of light as electromagnetic waves is in general governed by the Maxwell equations. These can be rewritten to the electromagnetic wave equation, see appendix A.5. Assuming a transverse electric field propagating along the x-axis and polarized in the $\hat{\mathbf{y}}$-direction the wave equation reduces to[1]

$$\frac{\partial^2}{\partial x^2}E - \frac{n_\mathrm{b}^2}{c^2}\frac{\partial^2}{\partial t^2}E = \mu_0\frac{\partial^2}{\partial t^2}P. \tag{4.1}$$

In our model, P is the polarization induced by the active QD material. It can cause different effects like absorption, dispersion and phase changes. The contribution to the polarization from the linear dielectric medium is included through the background refractive index, n_b.

We will now consider CW fields. These can be written as the real part of a complex field

$$E(x,t) = \mathrm{Re}[\tilde{E}_0 e^{i(kx-\omega t)}],$$

in terms of a complex amplitude, $\tilde{E}_0$. In a similar fashion we can write the polarization as the real part of a complex polarization. It is convenient to use these complex functions as they satisfy the wave equation, (4.1), too. To go back to the physical real quantities we can then take the real part. The complex complex representation of the CW field will then take the form,

$$\tilde{E}(x,t) = \tilde{E}_0 e^{i(kx-\omega t)} \tag{4.2}$$

We can write the polarization in terms of the first order susceptibility as a convolution integral

$$P(t) = \varepsilon_0 \int_{-\infty}^{+\infty} \chi(t')E(t-t')dt'.$$

[1] In the absence of free charges and currents.

If we insert eq. (4.2) into this we can get an expression for the complex polarization for a CW field

$$\begin{aligned}\tilde{P}(x,t) &= \varepsilon_0 \int_{-\infty}^{+\infty} \chi(t')\tilde{E}_0 e^{i[kx-\omega(t-t')]}dt' \\ &= \varepsilon_0 \int_{-\infty}^{+\infty} \chi(t')e^{i\omega t'}dt'\tilde{E}_0 e^{i(kx-\omega t)} \\ &= \varepsilon_0 \tilde{\chi}(\omega)\tilde{E}_0 e^{i(kx-\omega t)},\end{aligned}$$

where we have recognized the Fourier transform of $\chi(t)$ in the last line. In general, this is a complex number and we adopt the notation, $\tilde{\chi}(\omega) = \tilde{\chi} = \chi' + i\chi''$. Similar notation for the real and imaginary part will be used for other quantities. To get the physical polarization we take the real part. Using that $\tilde{E}_0$ is real and neglecting space dependence (k=0), we get

$$\begin{aligned}P(t) &= \mathrm{Re}[\varepsilon_0 \tilde{\chi}(\omega)\tilde{E}_0 e^{-i\omega t}] \\ &= \varepsilon_0 \chi'(\omega)E_0 \cos(\omega t) + \varepsilon_0 \chi''(\omega)E_0 \sin(\omega t).\end{aligned} \tag{4.3}$$

This can be used to compare to a similar expression for the polarization for a CW field found in the quantum model. Thereby we are able to find a closed form expression for the frequency dependent susceptibility, which describe the response from the material. This allows us to extract the main characteristics of a low intensity probe field, like its absorption, dispersion, and group velocity.

4.2. Miscellaneous relations

If we insert both the complex field and polarization into eq. (4.1) and use that $\mu_0\varepsilon_0 = c^{-2}$ we get

$$\frac{\partial^2}{\partial x^2}\tilde{E} - \frac{n_\mathrm{b}^2 + \tilde{\chi}}{c^2}\frac{\partial^2}{\partial t^2}\tilde{E} = 0.$$

We can now introduce the complex refractive index

$$\tilde{n}^2 = (n' + in'')^2 = n_\mathrm{b}^2 + \tilde{\chi} = n_\mathrm{b}^2 + \chi' + i\chi''. \tag{4.4}$$

Using the normal dispersion relation

$$\tilde{k} = \frac{\omega}{c}\tilde{n} \tag{4.5}$$

we see that $\tilde{k}$ is now complex. This corresponds to an absorbtion/gain of the field in the material which can be seen by inserting a complex $\tilde{k}$ into eq. (4.2),

$$\tilde{E}(x,t) = \tilde{E}_0 e^{i(\tilde{k}x-\omega t)} = \tilde{E}_0 e^{ik'(x-\frac{\omega}{k'}t)-k''x}.$$

From this we can extract the usual expressions for the phase velocity, and the absorption coefficient

$$v_\mathrm{ph} = \frac{\omega}{k'} = \frac{c}{n'}, \qquad \alpha = k'' = \frac{\omega n''}{c}.$$

Superimposing a lot of plane waves with different frequencies, ω, peaked around ω_0, we form a wave packet, characterized by an envelope function $\tilde{E}(x,t)$. Then v_{ph} still describes the velocity of the phase of the underlying fast oscillations, but does not describe the velocity of the envelope. The velocity of the envelope is denoted the *group velocity* and by means of Fourier theory a dispersion relation for the top of the envelope can be found (see appendix A.6) to give

$$v_{\text{g}} = \frac{\partial \omega}{\partial k'} = \frac{c}{n_{\text{g}}}. \tag{4.6}$$

The definition of the group velocity given in eq. (4.6) has some limitations. This is due to the fact that v_{g} is derived with the assumption that we find the velocity by following the peak point of the pulse, and see how it develops in time. If the shape of the pulse changes this will not hold. For strongly dispersive and absorbing media, this can lead to group velocities greater than c or even negative! This is of course not a violation of special relativity, but simply a limitation of the definition. Despite of this we use this definition as it has been applied before with success [1, 4].

The refractive group index, n_{g}, will be the main parameter throughout the report. This measures how fast a pulse propagates through a medium. We can find an expression for n_{g} in terms of n' by inserting the real part of the dispersion relation (4.5) into (4.6),

$$\frac{1}{v_{\text{g}}} = \frac{\partial k'}{\partial \omega} = \frac{\partial}{\partial \omega}\left(\frac{\omega n'(\omega)}{c}\right) = \frac{n'(\omega) + \omega \frac{\partial n'(\omega)}{\partial \omega}}{c}$$

and get

$$n_{\text{g}} = n'(\omega) + \omega \frac{\partial n'(\omega)}{\partial \omega}.$$

For the pulse field we now have two main results

$$n_{\text{g}} = n'(\omega) + \omega \frac{\partial n'(\omega)}{\partial \omega} \quad \text{and} \quad \alpha = \frac{\omega n''(\omega)}{c}. \tag{4.7}$$

We can relate n_{g} and α to the susceptibility using eq. (4.4)

$$\tilde{n} = \sqrt{n_{\text{b}}^2 + \tilde{\chi}}. \tag{4.8}$$

As a first approximation, (4.8) can be Taylor expanded to first order around $\tilde{\chi} = 0$ to get

$$\tilde{n} \approx n_{\text{b}} + \frac{\tilde{\chi}}{2n_{\text{b}}} \quad \Rightarrow \quad n' \approx n_{\text{b}} + \frac{\chi'}{2n_{\text{b}}}, \quad n'' \approx \frac{\chi''}{2n_{\text{b}}}.$$

This is what normally is done and in most cases is a good approximation. It is however not valid in all our simulations and an exact solution can be found [6, p. 237]

$$\begin{aligned} &(n' + in'')^2 = n_{\text{b}}^2 + \chi' + i\chi'' \\ \Downarrow \\ &n'^2 - n''^2 = n_{\text{b}}^2 + \chi', \quad 2n'n'' = \chi'', \end{aligned}$$

which can be solved for n' and n'' to give

$$n' = \frac{1}{\sqrt{2}}\sqrt{\sqrt{(n_\mathrm{b}^2 + \chi')^2 + \chi''^2} + n_\mathrm{b}^2 + \chi'}, \tag{4.9a}$$

$$n'' = \frac{1}{\sqrt{2}}\sqrt{\sqrt{(n_\mathrm{b}^2 + \chi')^2 + \chi''^2} - (n_\mathrm{b}^2 + \chi')} \cdot \mathrm{sgn}(\chi''). \tag{4.9b}$$

This describes how the susceptibility changes the real and imaginary parts of the refractive index and thus the refractive group index and absorption.

5. Light-matter Interaction

In this chapter we will consider the effect of an applied electric field on an atomic system. First the equations governing the response of the medium will be derived under as general conditions as possible. These equations, called the optical Bloch equations, will then be applied to the three-level system we use to achieve EIT. The resulting set of equations will serve as the starting point for both the steady state and dynamical analysis we will perform. The following derivations are inspired by the approach taken in [10, chapter 2]

5.1. The stationary system

We set out by considering a one particle quantum mechanical system. A particle, e.g. a carrier, in this system is governed by the time-dependent Schrödinger equation,

$$\hat{H}_{\mathrm{S}} \left|\Psi(\mathbf{r},t)\right\rangle = i\hbar \frac{\partial}{\partial t} \left|\Psi(\mathbf{r},t)\right\rangle$$

which for a time-independent potential can be separated into a time-dependent and time-independent part. The form of the state vector will then become: $\left|\Psi_n(\mathbf{r},t)\right\rangle = e^{-i\omega_n t} \left|\psi_n(\mathbf{r})\right\rangle$, where $\omega_n \equiv E_n/\hbar$. The spatial part of the state vector along with the eigenenergy are obtained from the time-independent Schrödinger equation,

$$\hat{H}_{\mathrm{S}} \left|\psi_n(\mathbf{r})\right\rangle = E_n \left|\psi_n(\mathbf{r})\right\rangle .$$

The complete solution[1] can now be expanded in the eigenstates of $\hat{H}_{\mathrm{S}}$,

$$\left|\Psi\right\rangle = \sum_n b_n \left|\Psi_n\right\rangle = \sum_n b_n e^{-i\omega_n t} \left|n\right\rangle ,$$

where the b_n's are time-independent probability amplitudes. The eigenstates of the stationary system will be assumed to known.

5.2. Time-dependent interaction

Introducing a time-dependent interaction Hamiltonian means that the full Hamiltonian of the system can be written as the sum of the stationary and the new term, $\hat{H} = \hat{H}_{\mathrm{S}} + \hat{H}_{\mathrm{I}}$. The time-dependent Schrödinger equation for the whole system now reads,

$$(\hat{H}_{\mathrm{S}} + \hat{H}_{\mathrm{I}}) \left|\Psi\right\rangle = i\hbar \frac{\partial}{\partial t} \left|\Psi\right\rangle . \tag{5.1}$$

[1] For simplicity we omit explicit arguments for the wave functions and further adopt the notation $\left|\psi_n\right\rangle = \left|n\right\rangle$.

Having obtained the eigenstates of the eigenvalue equation, these constitute a complete set and because of that we can expand the solution of eq. (5.1) in this basis. We assume that the continuous part of the spectrum can be neglected. Thus we write the solution as follows

$$|\Psi\rangle = \sum_n c_n |\Psi_n\rangle = \sum_n c_n e^{-i\omega_n t} |n\rangle . \tag{5.2}$$

The only difference from the solution to the stationary system, is that the probability amplitudes now depends on time (and possibly position), $c_n = c_n(\mathbf{r}, t)$, but they are still unknown. In order to determine the equations of motion for these, we plug the full solution into the time-dependent Schrödinger equation describing the system. This yields the following

$$(\hat{H}_\mathrm{S} + \hat{H}_\mathrm{I}) \sum_n c_n |\Psi_n\rangle = i\hbar \frac{\partial}{\partial t} \sum_n c_n |\Psi_n\rangle .$$

Letting the two Hamiltonians operate[2] on the left hand side and differentiating with respect to time[3] on the right hand side we obtain

$$\hat{H}_\mathrm{I} \sum_n c_n |\Psi_n\rangle + \sum_n c_n \underbrace{\hat{H}_\mathrm{S} |\Psi_n\rangle}_{=\hbar\omega_n |\Psi_n\rangle} = i\hbar \sum_n \dot{c}_n |\Psi_n\rangle + \sum_n c_n \hbar\omega_n |\Psi_n\rangle ,$$

cancelling the two sums with the $\hbar\omega_n$-factor we get

$$\hat{H}_\mathrm{I} \sum_n c_n |\Psi_n\rangle = i\hbar \sum_n \dot{c}_n |\Psi_n\rangle .$$

To find the equation governing each of the c_n's, we multiply the above equation by $\langle\Psi_l|$ from the left. This results in

$$\sum_n c_n e^{i(\omega_l - \omega_n)t} \langle l|\hat{H}_\mathrm{I}|n\rangle = i\hbar \sum_n e^{i(\omega_l - \omega_n)t} \dot{c}_n \underbrace{\langle l|n\rangle}_{=\delta_{ln}} = i\hbar \dot{c}_l . \tag{5.3}$$

Rearranging eq. (5.3) yields the equation of motion for the c_l's,

$$\dot{c}_l = \sum_n -\frac{i}{\hbar} c_n e^{i(\omega_l - \omega_n)t} \langle l|\hat{H}_\mathrm{I}|n\rangle . \tag{5.4}$$

5.3. Optical Bloch equations

The probability coefficients themselves are not of much interest, but rather their absolute values squared. These can be interpreted as the probability that the carrier is in that state. What we want, are equations of motion for the probabilities themselves. For this purpose we adopt the density matrix formalism, in which the squared probability amplitudes can be viewed as elements in a matrix. This matrix also contains off-diagonal elements, which are the ones we are really

[2] We assume that the $\mathbf{r}$-dependence of c_n and $\dot{c}_n$ is very small compared to the eigenstates.
[3] The dot denotes partial differentiation with respect to time, $\dot{f} \equiv \frac{\partial f}{\partial t}$.

after as they describe the induced dipoles. We now define an element in the density matrix as

$$\rho_{jk} \equiv c_j c_k^*,$$

where the * denotes the complex conjugate. Differentiating this with respect to time yields

$$\dot{\rho}_{jk} = \dot{c}_j c_k^* + c_j \dot{c}_k^*.$$

This equation along with eq. (5.4), and its complex conjugate, will provide us with the equations of motion for the ρ's. Thus we write

$$\begin{aligned}\dot{\rho}_{jk} &= \sum_n -\frac{i}{\hbar} \underbrace{c_n c_k^*}_{=\rho_{nk}} e^{i(\omega_j-\omega_n)t} \langle j|\hat{H}_\mathrm{I}|n\rangle + \sum_n \frac{i}{\hbar} \underbrace{c_j c_n^*}_{=\rho_{jn}} e^{-i(\omega_k-\omega_n)t} \langle n|\hat{H}_\mathrm{I}|k\rangle \\ &= \frac{i}{\hbar} \sum_n \left[\rho_{jn} e^{i\omega_{nk}t} \langle n|\hat{H}_\mathrm{I}|k\rangle - \rho_{nk} e^{i\omega_{jn}t} \langle j|\hat{H}_\mathrm{I}|n\rangle\right], \quad \omega_{ab} = \omega_a - \omega_b. \end{aligned} \tag{5.5}$$

These equations are called the optical Bloch equations. The form above provides a nearly exact description of the system, within the framework of quantum mechanics.

It is a very difficult task to write up the complete interaction Hamiltonian, as it contains many contributions that are hard to describe theoretically. Our model is based on electrons that only interact with the electromagnetic field and not with each other, thus many-body effects are not considered through fundamental principles. The effects of spontaneous emission, collisions, phonons, and other terms causing various kinds of decay/dephasing, will be added phenomenologically, as this is really the best we can do.

To account for the finite lifetime[4] of the electronic states we introduce a diagonal decay matrix, $\mathbf{\Gamma}$, such that $\Gamma_{nm} = \gamma_n \delta_{nm}$ [6, p. 161]. To incorporate the decay matrix we expand the anti-commutator $-\frac{1}{2}[\mathbf{\Gamma}, \rho]_+$ in the same set as our solution, using the closure relation $\hat{I} = \sum_n |n\rangle \langle n|$. Adding this to eq. (5.5) we obtain the following,

$$\dot{\rho}_{jk} = \frac{i}{\hbar} \sum_n \left[\rho_{jn} e^{i\omega_{nk}t} \langle n|\hat{H}_\mathrm{I}|k\rangle - \rho_{nk} e^{i\omega_{jn}t} \langle j|\hat{H}_\mathrm{I}|n\rangle\right] - \frac{1}{2} \sum_n \left[\gamma_j \delta_{jn} \rho_{nk} + \gamma_n \delta_{nk} \rho_{jn}\right]. \tag{5.6}$$

In expanding the relaxation sum above we will adopt the notation: $\gamma_{ab} \equiv \frac{\gamma_a}{2} + \frac{\gamma_b}{2}$. And further for the off-diagonal decays an extra dephase term, γ_ph, will be added to account for elastic interatomic collisions[5] so that: $\gamma_{ab,a\neq b} \Rightarrow \gamma_{ab} + \gamma_\mathrm{ph}$. This of course means that the decay rate of the off-diagonal elements always will be larger than that of the diagonal elements.

5.4. Field interaction

We now consider the explicit form of the interaction Hamiltonian, $\hat{H}_\mathrm{I}$, describing the electric field. Luckily, the main contribution to the interaction Hamiltonian is due to the so-called dipole

[4] The finite lifetime is an consequence of various effects we do not describe explicitly, but they still influence our electron states. Due to this coupling the energy of the states becomes uncertain by an amount ΔE and through Heisenberg's uncertainty relation, $\Delta E \Delta t \geq \frac{\hbar}{2}$, the states will have a finite lifetime.

[5] Being elastic the collisions does not change the energy of the states, but rather cause dephasing in the off-diagonal elements.

interaction between the electronic charge distribution and the applied electric field. The effect of the magnetic field, $\mathbf{B}$, associated with the electromagnetic wave is neglected, as it is a factor of $\frac{n_b}{c}$ smaller than the electric field. As described in chapter 2, EIT requires a strong coupling field and a weaker probe field carrying the signal you want transmitted. Classically[6] these two electric fields travelling along the x-axis and polarized along the y-axis, can be represented in the following way

$$\mathbf{E}(x,t) = E(x,t)\hat{\mathbf{y}} = E_{\mathrm{p}}(x,t)\cos(k_{\mathrm{p}}x - \omega_{\mathrm{p}}t + \phi_{\mathrm{p}}(x,t))\hat{\mathbf{y}} + E_{\mathrm{c}}(x,t)\cos(k_{\mathrm{c}}x - \omega_{\mathrm{c}}t + \phi_{\mathrm{c}}(x,t))\hat{\mathbf{y}}, \tag{5.7}$$

where $\hat{\mathbf{y}}$ is a unit vector in the y-direction and $E(x,t)$, k, ω and $\phi(x,t)$ is the field envelope, wave vector, frequency, and phase of the respective field. This way of representing the field is perfectly valid, but due to some numerical issues discussed in section 7.1, we will rewrite this representation. Any field given on the form of one of the terms in eq. (5.7) can be rewritten to

$$E(x,t) = \frac{1}{2}\tilde{E}(x,t)e^{i(kx-\omega t)} + \frac{1}{2}\tilde{E}^*(x,t)e^{-i(kx-\omega t)}, \tag{5.8}$$

where we have introduced a complex envelope given by: $\tilde{E} = E' + iE''$. The components of the new envelope are defined as: $E' \equiv E\cos\phi$ and $E'' \equiv E\sin\phi$.

The dipole moment operator of the electron is given by: $\hat{\mathbf{d}} = -e\mathbf{r}$ and the interaction Hamiltonian is equal to the potential energy of the dipole in a electric field,

$$\hat{H}_{\mathrm{I}} = -\hat{\mathbf{d}}\cdot\mathbf{E} = eyE(x,t).$$

Plugging the rewritten field into this yields,

$$\hat{H}_{\mathrm{I}} = \frac{ey}{2}\left(\tilde{E}_{\mathrm{p}}e^{i(k_{\mathrm{p}}x-\omega_{\mathrm{p}}t)} + \tilde{E}^*_{\mathrm{p}}e^{-i(k_{\mathrm{p}}x-\omega_{\mathrm{p}}t)} + \tilde{E}_{\mathrm{c}}e^{i(k_{\mathrm{c}}x-\omega_{\mathrm{c}}t)} + \tilde{E}^*_{\mathrm{c}}e^{-i(k_{\mathrm{c}}x-\omega_{\mathrm{c}}t)}\right),$$

plugging this into eq. (5.6) we get

$$\begin{aligned}\dot{\rho}_{jk} = \frac{i}{2\hbar}\sum_n \Big[&\rho_{jn}\mu_{nk}e^{i\omega_{nk}t}\left(\tilde{E}_{\mathrm{p}}e^{i(k_{\mathrm{p}}x-\omega_{\mathrm{p}}t)} + \tilde{E}^*_{\mathrm{p}}e^{-i(k_{\mathrm{p}}x-\omega_{\mathrm{p}}t)} + \tilde{E}_{\mathrm{c}}e^{i(k_{\mathrm{c}}x-\omega_{\mathrm{c}}t)} + \tilde{E}^*_{\mathrm{c}}e^{-i(k_{\mathrm{c}}x-\omega_{\mathrm{c}}t)}\right)\\ &-\rho_{nk}\mu_{jn}e^{i\omega_{jn}t}\left(\tilde{E}_{\mathrm{p}}e^{i(k_{\mathrm{p}}x-\omega_{\mathrm{p}}t)} + \tilde{E}^*_{\mathrm{p}}e^{-i(k_{\mathrm{p}}x-\omega_{\mathrm{p}}t)} + \tilde{E}_{\mathrm{c}}e^{i(k_{\mathrm{c}}x-\omega_{\mathrm{c}}t)} + \tilde{E}^*_{\mathrm{c}}e^{-i(k_{\mathrm{c}}x-\omega_{\mathrm{c}}t)}\right)\Big]\\ -\frac{1}{2}\sum_n &\left[\gamma_j\delta_{jn}\rho_{nk} + \gamma_n\delta_{nk}\rho_{jn}\right],\end{aligned} \tag{5.9}$$

where the transition matrix elements are defined as $\mu_{nk} \equiv e\langle n|y|k\rangle$. In taking the matrix elements of the interaction Hamiltonian, we assume the electric field part is essentially constant over the dimensions of the QD. Therefore it can be taken outside the braket. This assumption is well meet for the case of light in the visible range and with envelopes much larger than the QD. As the name indicates, the transition matrix element measures the strength of a transition. This has the consequence that we only have a dipole moment for allowed transitions. For the three-level QD system we are going to consider shortly, the transition matrix elements have been calculated in

[6] We use the classical representation of the electric field, rather than a quantized field. This gives a correct description when a very large number of photons are involved, ie. high field amplitudes.

chapter 3. Due to the selection rules of the QD system and the fact that[7] $\mu_{nn} = e\langle n|y|n\rangle = 0$, the only non-zero transition matrix elements are: μ_{12}, μ_{21}, μ_{23} and μ_{32}.

As seen from eq. (5.9) we will get a lot of complex exponentials oscillating at high and low frequencies. The frequencies will be of the form: $\omega_{ab} \pm \omega_{\text{p or c}}$, with $\omega_{ab} > 0$. The maximum effect of EIT is reached when the frequencies of probe and coupling field are tuned very close to transitions they are to match. This means that we will have a few exponentials oscillating at a frequency close to zero and many who oscillate at much higher frequencies. Neglecting all other terms than those at low frequency is called the rotating wave approximation (RWA). We will apply the RWA in the rest of this work, as it yields very significant simplifications in the analytical work and make it possible to solve numerically.

5.5. The three-level Bloch equations

To obtain the equations of motion describing our three-level system, we have to let j and k run from 1 to 3 in all combinations in eq. (5.9). This will result in 9 equations all in all. To reduce this number we recall the definition of the density matrix elements, $\rho_{jk} \equiv c_j c_k^*$, and notice that, $\rho_{jk}^* = [c_j c_k^*]^* = c_k c_j^* = \rho_{kj}$. The 6 off-diagonal elements equations reduces to 3 and we are left with 6 distinct[8] equations for the matrix elements. Using eq. (5.9), applying the RWA and the fact that the only non-zero transition matrix elements are: μ_{12}, μ_{21}, μ_{23} and μ_{32}, we get the following equations of motions for the diagonal elements

$$\begin{aligned}
\dot{\rho}_{11} &= i\Omega_{\text{p}}^* e^{i(k_{\text{p}}x+\Delta_{\text{p}}t)}\rho_{12} - i\Omega_{\text{p}} e^{-i(k_{\text{p}}x+\Delta_{\text{p}}t)}\rho_{21} + \gamma_{22}\rho_{22} + \gamma_{33}\rho_{33}, \\
\dot{\rho}_{22} &= -i\Omega_{\text{p}}^* e^{i(k_{\text{p}}x+\Delta_{\text{p}}t)}\rho_{12} + i\Omega_{\text{p}} e^{-i(k_{\text{p}}x+\Delta_{\text{p}}t)}\rho_{21} + i\Omega_{\text{c}}^* e^{i(k_{\text{c}}x+\Delta_{\text{c}}t)}\rho_{23} - i\Omega_{\text{c}} e^{-i(k_{\text{c}}x+\Delta_{\text{c}}t)}\rho_{32} - \gamma_{22}\rho_{22}, \\
\dot{\rho}_{33} &= i\Omega_{\text{c}} e^{-i(k_{\text{c}}x+\Delta_{\text{c}}t)}\rho_{32} - i\Omega_{\text{c}}^* e^{i(k_{\text{c}}x+\Delta_{\text{c}}t)}\rho_{23} - \gamma_{33}\rho_{33}.
\end{aligned}$$

We have defined the detuning frequencies for the probe and coupling fields respectively as, $\Delta_{\text{p}} \equiv \omega_{21} - \omega_{\text{p}}$ and $\Delta_{\text{c}} \equiv \omega_{32} - \omega_{\text{c}}$, and the complex Rabi frequencies[9] are defined as $\Omega_{\text{p}} \equiv \frac{\mu_{12}\tilde{E}_{\text{p}}^*}{2\hbar}$ and $\Omega_{\text{c}} \equiv \frac{\mu_{23}\tilde{E}_{\text{c}}^*}{2\hbar}$, for the probe and coupling fields respectively. These might have a spatial dependence as the field envelopes might.

The two last terms in the equation for $\dot{\rho}_{11}$ do not come from eq. (5.9), but these are necessary in order to conserve probability in the system. Physically this means that decay from the two upper levels will end up in $|1\rangle$. For the off-diagonal elements we again apply eq. (5.9), this yields

$$\begin{aligned}
\dot{\rho}_{12} = \dot{\rho}_{21}^* &= i\Omega_{\text{p}} e^{-i(k_{\text{p}}x+\Delta_{\text{p}}t)}(\rho_{11} - \rho_{22}) + i\Omega_{\text{c}}^* e^{i(k_{\text{c}}x+\Delta_{\text{c}}t)}\rho_{13} - \gamma_{12}\rho_{12}, \\
\dot{\rho}_{13} = \dot{\rho}_{31}^* &= i\Omega_{\text{c}} e^{-i(k_{\text{c}}x+\Delta_{\text{c}}t)}\rho_{12} - i\Omega_{\text{p}} e^{-i(k_{\text{p}}x+\Delta_{\text{p}}t)}\rho_{23} - \gamma_{13}\rho_{13}, \\
\dot{\rho}_{23} = \dot{\rho}_{32}^* &= i\Omega_{\text{c}} e^{-(k_{\text{c}}x+\Delta_{\text{c}}t)}(\rho_{22} - \rho_{33}) - i\Omega_{\text{p}}^* e^{i(k_{\text{p}}x+\Delta_{\text{p}}t)}\rho_{13} - \gamma_{23}\rho_{23}.
\end{aligned}$$

This set of first order equations constitute a fairly complicated problem due to the fact that we have non-constant coefficients in the system, that possibly also depends on position. However

[7] Since the bra and ket will have the same parity, even or odd, and y is inherently odd this integral will equal zero.

[8] Really it is 5 distinct equations, as conservation of probability requires that: $\rho_{11}+\rho_{22}+\rho_{33} = 1 \Rightarrow \dot{\rho}_{11}+\dot{\rho}_{22}+\dot{\rho}_{33} = 0$.

[9] It should be noted that another commonly used definition of the Rabi frequency is: $\Omega = \frac{\mu E}{\hbar}$, which is twice our definition.

by introducing the following set of transformations of the off-diagonal elements, we can simplify the equations a bit (and as a bonus the transformed functions are occurring naturally in the calculations of the dipoles). The transformations are as follows

$$\rho_{12} = \sigma_{12} e^{-i(k_\mathrm{p} x + \Delta_\mathrm{p} t)}, \quad \rho_{13} = \sigma_{13} e^{-i((k_\mathrm{p}+k_\mathrm{c})x + (\Delta_\mathrm{p}+\Delta_\mathrm{c})t)}, \quad \rho_{23} = \sigma_{23} e^{-i(k_\mathrm{c} x + \Delta_\mathrm{c} t)}, \tag{5.10}$$

and of course their complex conjugates. Plugging these into our Bloch equations and performing straight forward differentiations and multiplication we obtain the following transformed set of Bloch equations

$$\dot{\rho}_{11} = i\Omega_\mathrm{p}^* \sigma_{12} - i\Omega_\mathrm{p} \sigma_{21} + \gamma_{22}\rho_{22} + \gamma_{33}\rho_{33}, \tag{5.11a}$$

$$\dot{\rho}_{22} = -i\Omega_\mathrm{p}^* \sigma_{12} + i\Omega_\mathrm{p} \sigma_{21} + i\Omega_\mathrm{c}^* \sigma_{23} - i\Omega_\mathrm{c} \sigma_{32} - \gamma_{22}\rho_{22}, \tag{5.11b}$$

$$\dot{\rho}_{33} = i\Omega_\mathrm{c} \sigma_{32} - i\Omega_\mathrm{c}^* \sigma_{23} - \gamma_{33}\rho_{33}. \tag{5.11c}$$

And for the off-diagonal elements,

$$\dot{\sigma}_{12} = \dot{\sigma}_{21}^* = i\Omega_\mathrm{p}(\rho_{11} - \rho_{22}) + i\Omega_\mathrm{c}^* \sigma_{13} - \tilde{\gamma}_{12}\sigma_{12}, \tag{5.11d}$$

$$\dot{\sigma}_{13} = \dot{\sigma}_{31}^* = i\Omega_\mathrm{c} \sigma_{12} - i\Omega_\mathrm{p} \sigma_{23} - \tilde{\gamma}_{13}\sigma_{13}, \tag{5.11e}$$

$$\dot{\sigma}_{23} = \dot{\sigma}_{32}^* = i\Omega_\mathrm{c}(\rho_{22} - \rho_{33}) - i\Omega_\mathrm{p}^* \sigma_{13} - \tilde{\gamma}_{23}\sigma_{23}, \tag{5.11f}$$

where we for notational simplicity have introduced the complex detunings: $\tilde{\gamma}_{12} \equiv \gamma_{12} - i\Delta_\mathrm{p}$, $\tilde{\gamma}_{13} \equiv \gamma_{13} - i(\Delta_\mathrm{p} + \Delta_\mathrm{c})$ and $\tilde{\gamma}_{23} \equiv \gamma_{23} - i\Delta_\mathrm{c}$. We now have the complete set of equations describing our three-level system. In the following chapters these equations will be used for different forms of the electric field envelope.

6. Steady State Analysis

In this chapter we start our analysis of slow-light by considering the simplest case of the electric field, namely a CW field with no phase term. This we can treat analytically and expressions for the susceptibility are obtained in the steady state and long wavelength limit. In the end we give numerical examples of the refractive group index and various parameters are discussed. The following analysis has been performed by [1, 4] and our approach is in large parts inspired by these papers.

6.1. Continuous wave fields

In the following analysis we will use CW fields, with no phase terms. Setting the phase to zero, the complex envelope we introduced in section 5.4 reduces to a scalar, as $\cos(0) = 1$ and $\sin(0) = 0$. The total field will have the form

$$\mathbf{E}(x,t) = E_{\mathrm{p}} \cos(k_{\mathrm{p}} x - \omega_{\mathrm{p}} t)\hat{\mathbf{y}} + E_{\mathrm{c}} \cos(k_{\mathrm{c}} x - \omega_{\mathrm{c}} t)\hat{\mathbf{y}}.$$

The field envelopes, E_{p} and E_{c}, are constant in both position and time corresponding to infinite width in these two dimensions. This implies that the spectral width is infinitely narrow, essentially a delta spike. In order to simplify, we will use the so-called dipole approximation, in which we set $k_{\mathrm{c,p}} = 0$ (long wavelength limit). This approximation can be justified by considering the following: The wavelength of visible light is of the order 5.5×10^{-7} m hence $k \simeq 1.0 \times 10^{7}$ m^{-1}. The dimensions of our QDs is of order of nanometers, from which it follows that $k\Delta x_{\mathrm{QD}} \simeq 10^{-2}$. This shows that the contribution from the variation in x is very small and can therefore be neglected, hence the electric field becomes a function of time alone

$$\mathbf{E}(t) = E_{\mathrm{p}} \cos(\omega_{\mathrm{p}} t)\hat{\mathbf{y}} + E_{\mathrm{c}} \cos(\omega_{\mathrm{c}} t)\hat{\mathbf{y}}.$$

Having this functional form of the field, we do not allow it to change due to the interaction with the QDs. This approach can be justified, as very wide pulses consists of very few frequency components (one in the limit of a true CW field). It can be expected that after a certain duration, the microscopic dipoles and hence the polarization will oscillate out of phase with the field, which corresponds to a frequency-dependent susceptibility.

6.2. The complex susceptibility

In order to obtain the real part of the refractive index, and thus the slowdown factor, we need an expression for the complex susceptibility that gives rise to the induced polarization in the medium. From classical electromagnetism we recall that the macroscopic polarization is defined as the density of the microscopic dipoles

$$\mathbf{P} \equiv N \langle \mathbf{d} \rangle . \tag{6.1}$$

We define N to be the density of QDs. It really should be the density of dipoles, but each QD only contains one (two if you include spin) electron(s) at each energy level, so these two densities are equal. In chapter 5, we derived the theory enabling us to calculate the induced microscopic dipoles. The average value of the dipole in eq. (6.1) can be obtained through the quantum mechanical average of the dipole operator

$$\langle \mathbf{d} \rangle = \langle \Psi | - e\mathbf{r} | \Psi \rangle .$$

As we have polarized our electric field in the y-direction, the dipole becomes a scalar as $\mathbf{r} \to y$. Inserting the full wave function given by eq. (5.2) yields the following

$$\langle d \rangle = -e \left(\sum_{n=1}^{3} c_n^* e^{i\omega_n t} \langle n | \right) y \left(\sum_{n=1}^{3} c_n e^{-i\omega_n t} | n \rangle \right) .$$

Exploiting the transition selection rules (i.e. $y_{13} = y_{31} = 0$), the parity of the eigenstates along with the definitions of the density matrix elements the sums reduce to

$$\langle d \rangle = -e \left(\rho_{12} y_{21} e^{i\omega_{21} t} + \rho_{21} y_{12} e^{-i\omega_{21} t} + \rho_{23} y_{32} e^{i\omega_{32} t} + \rho_{32} y_{23} e^{-i\omega_{32} t} \right) , \tag{6.2}$$

where $y_{ab} = \langle a | y | b \rangle$. Introducing the transition matrix elements and the transformation[1] of the off-diagonal elements given by eq. (5.10) the average of the induced dipoles becomes

$$\langle d \rangle = - \left(\sigma_{12} \mu_{21} e^{i\omega_\mathrm{p} t} + \sigma_{21} \mu_{12} e^{-i\omega_\mathrm{p} t} + \sigma_{23} \mu_{32} e^{i\omega_\mathrm{c} t} + \sigma_{32} \mu_{23} e^{-i\omega_\mathrm{c} t} \right) .$$

The probe field, which is the one we want slowed down, only experience the polarization induced by the two first terms in the above expression. This you can realize from the electromagnetic wave equation. In the same way the coupling field only sees the two last. We separate in this way because in the end we are only interested in the susceptibility seen by the probe field. The polarization seen by the probe is

$$P_\mathrm{p} = N \langle d_\mathrm{p} \rangle = -N \left(\sigma_{12} \mu_{21} e^{i\omega_\mathrm{p} t} + \sigma_{21} \mu_{12} e^{-i\omega_\mathrm{p} t} \right) .$$

We rewrite this in terms of cosine and sine as this will become handy in a moment,

$$P_\mathrm{p} = -N \left(\left[\sigma_{12} \mu_{21} + \sigma_{21} \mu_{12} \right] \cos(\omega_\mathrm{p} t) + i \left[\sigma_{12} \mu_{21} - \sigma_{21} \mu_{12} \right] \sin(\omega_\mathrm{p} t) \right) .$$

Comparing to $P_\mathrm{p} = \varepsilon_0 \chi' E_\mathrm{p} \cos(\omega_\mathrm{p} t) + \varepsilon_0 \chi'' E_\mathrm{p} \sin(\omega_\mathrm{p} t)$, eq. (4.3), we can immediately read off the expressions for the real and imaginary part of the susceptibility. Doing this we obtain for the real part

$$\chi' = -\frac{N}{\varepsilon_0 E_\mathrm{p}} \left[\sigma_{12} \mu_{21} + \sigma_{21} \mu_{12} \right] , \tag{6.3}$$

and for the imaginary part

$$\chi'' = -i \frac{N}{\varepsilon_0 E_\mathrm{p}} \left[\sigma_{12} \mu_{21} - \sigma_{21} \mu_{12} \right] . \tag{6.4}$$

Notice that the second term in both the square brackets is complex conjugate of the first, $\sigma_{21} \mu_{12} = [\sigma_{12} \mu_{21}]^*$, so it is already now clear that the real and imaginary part are real quantities as they

[1] Due to the dipole approximation we can set $k_{p,c} = 0$ in these too.

should be. The equations above indicate that the susceptibility seen by the probe, depends on the off-diagonal density matrix elements and transition matrix elements that couple the $|1\rangle \leftrightarrow |2\rangle$ transition. This is reasonable because the probe fields frequency is tuned to match the $|1\rangle \leftrightarrow |2\rangle$ transition.

From eq. (6.3) and (6.4) it is apparent that we need to obtain the functional expression for σ_{12} and σ_{21}, or really just one of them as they are each others complex conjugates. This involves solving the complete set of Bloch equations eq. (5.11a) to (5.11f) in steady state, that is all the time derivatives set to zero. The steady state solutions are in closed form very extensive, so through the solution process we will make a few approximations. The assumptions in these approximations are however very well justified under normal EIT conditions, see appendix A.2.

Setting the time derivative equal to zero, reduces the equation of motion for σ_{12} (we only solve for σ_{12} as $\sigma_{21} = \sigma_{12}^*$) to

$$0 = i\Omega_\mathrm{p}(\rho_{11} - \rho_{22}) + i\Omega_\mathrm{c}^*\sigma_{13} - \tilde{\gamma}_{12}\sigma_{12}.$$

The first term contains the difference in occupation between level 1 and 2. When EIT is reached, almost all carriers will be in the ground state and this difference will be ≈ 1. We consider this as nearly constant and set $\eta \equiv \rho_{11} - \rho_{22}$ and solve for σ_{12}

$$\sigma_{12} = \frac{1}{\tilde{\gamma}_{12}}\left(i\Omega_\mathrm{p}\eta + i\Omega_\mathrm{c}^*\sigma_{13}\right). \tag{6.5}$$

Next we consider the steady state equation of σ_{13}

$$0 = i\Omega_\mathrm{c}\sigma_{12} - i\Omega_\mathrm{p}\sigma_{23} - \tilde{\gamma}_{13}\sigma_{13},$$

and notice that in the two first terms we have the Rabi frequencies for the coupling and probe field as factors. In order for EIT to work, the field that couples the two upper levels must be much stronger than the field that couples the two lower levels, this means that $\Omega_\mathrm{c} \gg \Omega_\mathrm{p}$. Under the assumption that this condition is fulfilled, we can neglect the second term in the equation for σ_{13}. Doing this and solving for σ_{13} yields

$$\sigma_{13} = i\frac{\Omega_\mathrm{c}}{\tilde{\gamma}_{13}}\sigma_{12}.$$

This can now be inserted into eq. (6.5), solving again for σ_{12} we arrive at an approximate steady state solution for σ_{12} (and σ_{21}) which is given by

$$\sigma_{12} = \frac{i\tilde{\gamma}_{13}\Omega_\mathrm{p}\eta}{\tilde{\gamma}_{12}\tilde{\gamma}_{13} + |\Omega_\mathrm{c}|^2}.$$

As seen from eq. (6.3) and (6.4) we need the product $\sigma_{12}\mu_{21}$ in the calculation of the susceptibility, so we will calculate this first. Inserting the complex detunings, defined below eq. (5.11f), and multiplying with μ_{21} we get

$$\mu_{21}\sigma_{12} = \frac{\mu_{21}\Omega_\mathrm{p}((\Delta_\mathrm{p} + \Delta_\mathrm{c}) + i\gamma_{13})\eta}{(\gamma_{12} - i\Delta_\mathrm{p})(\gamma_{13} - i\Delta_\mathrm{c}) + |\Omega_\mathrm{c}|^2}.$$

Reminding how Ω_p is defined, namely $\Omega_\mathrm{p} = \frac{\mu_{12}E_\mathrm{p}}{2\hbar}$, we notice that $\mu_{21}\Omega_\mathrm{p} = \frac{\mu_{21}\mu_{21}^*E_\mathrm{p}}{2\hbar} = \frac{|\mu_{21}|^2E_\mathrm{p}}{2\hbar}$ is a real number. Using this and for convenience setting the real part of the denominator equal to:

$\xi = \gamma_{12}\gamma_{13} - \Delta_\mathrm{p}(\Delta_\mathrm{p}+\Delta_\mathrm{c}) + |\Omega_\mathrm{c}|^2$, and the imaginary part equal to: $\zeta = -(\Delta_\mathrm{p}+\Delta_\mathrm{c})\gamma_{12} - \Delta_\mathrm{p}\gamma_{13}$, we can write

$$\mu_{21}\sigma_{12} = \frac{|\mu_{21}|^2 E_\mathrm{p}\eta}{2\hbar(\xi^2+\zeta^2)}\left([(\Delta_\mathrm{p}+\Delta_\mathrm{c})\xi + \gamma_{13}\zeta] + i\left[\gamma_{13}\xi - (\Delta_\mathrm{p}+\Delta_\mathrm{c})\zeta\right]\right).$$

Having clearly separated this product into a real and imaginary part makes the calculation of the susceptibility easier. We are now down to plugging the above determined product into eq. (6.3) and (6.4). For the real part of the susceptibility we obtain

$$\begin{aligned}\chi' &= -\frac{N}{\varepsilon_0 E_\mathrm{p}}\frac{|\mu_{21}|^2 E_\mathrm{p}\eta}{2\hbar(\xi^2+\zeta^2)}\left([(\Delta_\mathrm{p}+\Delta_\mathrm{c})\xi + \gamma_{13}\zeta] + i\left[\gamma_{13}\xi - (\Delta_\mathrm{p}+\Delta_\mathrm{c})\zeta\right] + c.c.\right)\\ &= -\frac{N|\mu_{21}|^2\eta}{2\hbar\varepsilon_0(\xi^2+\zeta^2)}2[(\Delta_\mathrm{p}+\Delta_\mathrm{c})\xi + \gamma_{13}\zeta]\end{aligned}$$

where *c.c.* denotes the complex conjugate. Inserting ξ and ζ and rearranging yields the wanted approximate expression for χ', namely

$$\chi' = \frac{N|\mu_{21}|^2\eta}{\varepsilon_0\hbar}\frac{\gamma_{13}^2\Delta_\mathrm{p} + (\Delta_\mathrm{p}+\Delta_\mathrm{c})(\Delta_\mathrm{p}(\Delta_\mathrm{p}+\Delta_\mathrm{c}) - |\Omega_\mathrm{c}|^2)}{\left[\gamma_{12}\gamma_{13} - \Delta_\mathrm{p}(\Delta_\mathrm{p}+\Delta_\mathrm{c}) + |\Omega_\mathrm{c}|^2\right]^2 + \left[(\Delta_\mathrm{p}+\Delta_\mathrm{c})\gamma_{12} + \Delta_\mathrm{p}\gamma_{13}\right]^2}. \tag{6.6}$$

For the imaginary part the procedure is much the same, from eq. (6.4) we get

$$\begin{aligned}\chi'' &= -i\frac{N}{\varepsilon_0 E_\mathrm{p}}\frac{|\mu_{21}|^2 E_\mathrm{p}\eta}{2\hbar(\xi^2+\zeta^2)}\left([(\Delta_\mathrm{p}+\Delta_\mathrm{c})\xi + \gamma_{13}\zeta] + i\left[\gamma_{13}\xi - (\Delta_\mathrm{p}+\Delta_\mathrm{c})\zeta\right] - c.c.\right)\\ &= -i\frac{N|\mu_{21}|^2\eta}{2\hbar\varepsilon_0(\xi^2+\zeta^2)}2i\left[\gamma_{13}\xi - (\Delta_\mathrm{p}+\Delta_\mathrm{c})\zeta\right],\end{aligned}$$

again inserting ξ and ζ and rearranging we arrive at the approximate expression for χ'', which is

$$\chi'' = \frac{N|\mu_{21}|^2\eta}{\varepsilon_0\hbar}\frac{\gamma_{13}(\gamma_{13}\gamma_{12} + |\Omega_\mathrm{c}|^2) + (\Delta_\mathrm{p}+\Delta_\mathrm{c})^2\gamma_{12}}{\left[\gamma_{12}\gamma_{13} - \Delta_\mathrm{p}(\Delta_\mathrm{p}+\Delta_\mathrm{c}) + |\Omega_\mathrm{c}|^2\right]^2 + \left[(\Delta_\mathrm{p}+\Delta_\mathrm{c})\gamma_{12} + \Delta_\mathrm{p}\gamma_{13}\right]^2}. \tag{6.7}$$

We notice that χ'' always[2] will be positive, as intended through our definition of the complex susceptibility. The reason why we wanted χ'' positive comes from the fact that the imaginary part of the susceptibility corresponds more or less to the absorption coefficient, which traditionally[3] is a positive quantity. We also notice how the approximations used have made several of the original parameters drop out of the solutions. These are the decay rates for the states $|2\rangle$ and $|3\rangle$, γ_{22} and γ_{33}. Also the decay rate for the $|2\rangle \leftrightarrow |3\rangle$ dipole transition, has lost its significance. Most noticeable perhaps is the fact that the probe field amplitude E_p (and hence Ω_p) is of no importance, as long as it satisfies $\Omega_\mathrm{p} \ll \Omega_\mathrm{c}$.

6.3. The refractive group index

Having obtained the susceptibility we can calculate the refractive group index, the quantity we are really after. According to eq. (4.7) the group index is given by

$$n_\mathrm{g} = n' + \omega_\mathrm{p}\frac{\partial n'}{\partial \omega_\mathrm{p}},$$

[2] Provided that we have reached EIT, such that $\eta > 0$.

[3] The absorption coefficient α is approximately equal to $\frac{\omega\chi''}{2n_\mathrm{b}c}$ and normal exponential decay is usually written in the form $e^{-\alpha x}$, with $\alpha > 0$.

where n', the real part of the refractive index, is known from eq. (4.9a),

$$n' = \frac{1}{\sqrt{2}}\sqrt{\sqrt{(n_\mathrm{b}+\chi')^2+\chi''^2}+n_\mathrm{b}^2+\chi'}.$$

From straightforward substitution and differentiation the explicit expression for the group index is right in front of us. This is however a rather cumbersome affair and the actual calculation has been carried out in MATHEMATICA. The detuning of both fields has been set to zero, thus obtaining a slightly simpler expression and maximum EIT effect, the result is

$$n_\mathrm{g} = \left[\frac{\varepsilon_\mathrm{b}+\sqrt{\varepsilon_\mathrm{b}^2+\varepsilon_\mathrm{res}^2}}{2}\right]^{\frac{1}{2}}\left[1+\frac{\hbar\omega_{21}}{2\sqrt{\varepsilon_\mathrm{b}^2+\varepsilon_\mathrm{res}^2}}\frac{U_{21}(|\Omega_\mathrm{p}|^2-\tilde{\gamma}_{13}^2)}{\hbar^2(\tilde{\gamma}_{13}\tilde{\gamma}_{12}+|\Omega_\mathrm{p}|^2)^2}\right], \tag{6.8}$$

where $\varepsilon_\mathrm{b} = n_\mathrm{b}^2$, $U_{21} = \frac{N|\mu_{21}|^2\eta}{\varepsilon_0}$, and $\varepsilon_\mathrm{res} = \frac{U_{21}}{\hbar\ \gamma_{12}+\frac{|\Omega_\mathrm{p}|^2}{\gamma_{13}}}$. The background dielectric constant is denoted ε_b, U_{21} is related to the oscillator strength of the probe and ε_res is a kind of resulting dielectric function seen by the way it adds to ε_b [4].

6.4. Numerical examples

In order to get a better understanding of the results obtained, we want to illustrate these by sets of realistic parameter values. By inspection of eq. (6.6), (6.7) and (6.8) we infer that the set of parameters we need values for are: N, μ_{21}, μ_{32}, γ_{12}, γ_{13}, η, n_b and Ω_c. The detuning for the coupling field, Δ_c, will throughout this section be set to zero.

For the density of QDs we have chosen $N = 3\times10^{21}$ m^{-3}, this leads to a center-to-center distance for the QDs of 70 nm, assuming they are placed in a square lattice. This is a parameter that we assume will be very controllable in the future, as growth techniques develop.

The values of the transition matrix elements have been calculated in chapter 3 for a variety of different dot sizes. For these calculations we have used the reference QD introduced in section 3.3. The calculated values are: $\mu_{21} = 1.07\times10^{-28}$ Cm $= 0.67\ e$ nm and $\mu_{32} = 4.69\times10^{-28}$ Cm $= 2.93\ e$ nm.

For the decay rates of the off-diagonal elements, we have found experimental data for dephasing times in InAs and InGaAs QDs. We will use these as indicators for the order of magnitude of our decay rates. These dephasing times have been measured at different temperatures and from [11, 12] we can compose table 6.1. The table indicates that the decay rate ranges from a few GHz to around 3.5×10^3 GHz, within the temperature range of 7 K to room temperature. The actual decay rate used will be indicated in the calculation.

The population inversion between level 1 and 2, η, will be set to 1 as almost all carriers are trapped in the ground state (EIT state). The background refractive index, n_b, of GaAs has the value 3.6. The Rabi frequency for the coupling field, Ω_c, we will leave as an open parameter, as this parameter is easily changeable.

To summarize, we have collected all the parameters used in the table 6.2.

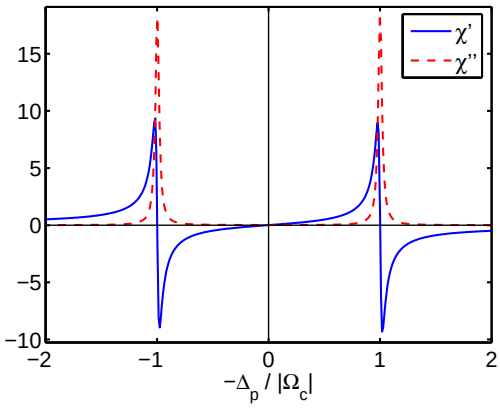

(a) For this plot: $\gamma_{12} = \gamma_{13} = 10^0$ GHz and $|\Omega_c| = 50$ GHz

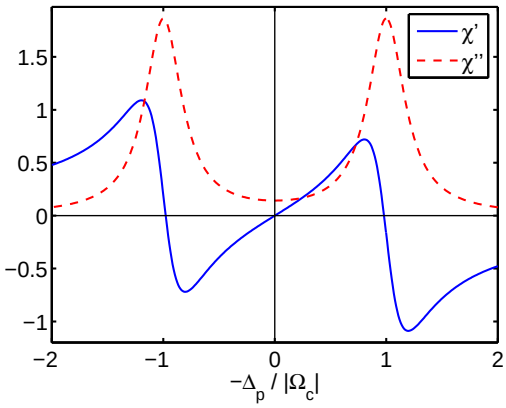

(b) For this plot: $\gamma_{12} = \gamma_{13} = 10^1$ GHz and $|\Omega_c| = 50$ GHz

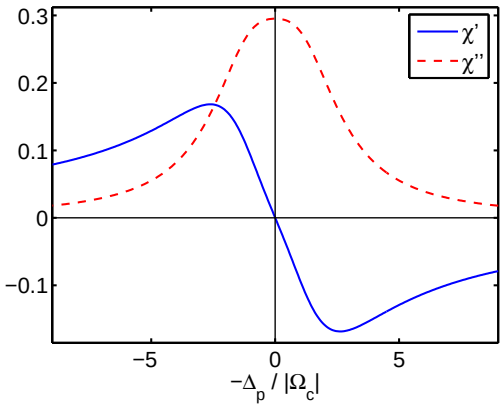

(c) For this plot: $\gamma_{12} = \gamma_{13} = 10^2$ GHz and $|\Omega_c| = 50$ GHz

Figure 6.1.: *Real and imaginary part of the susceptibility plotted against the probe detuning, for different sets of parameter values.*

Temperature [K]	T_2 [ps]	$\gamma = 1/T_2$ [GHz]
7	630	1.59
25	170	5.88
50	37	27.0
75	11	90.9
100	6	161
300	0.29	3448.0

Table 6.1.: *Dephasing times [11, 12].*

Quantity	Symbol	Value	Unit
Density of QDs	N	3×10^{21}	m^{-3}
Transition matrix element	μ_{21}	1.07×10^{-28}	Cm
Transition matrix element	μ_{32}	4.69×10^{-28}	Cm
Off-diagonal decay rate	$\gamma_{12/13}$	variable	Hz
Population difference	η	1	-
Background refractive index	n_b	3.6	-
Rabi frequency for coupling field	Ω_c	variable	Hz

Table 6.2.: *Parameters used in the calculations.*

In figure 6.1 we have illustrated the complex susceptibility eq. (6.6) and (6.7), for a few sets of parameter values. In section 4.2 it has been shown that under normal conditions the dispersion, n', is approximately proportional to χ' and the absorption, n'', is approximately proportional to χ''. We will adopt this and will often speak of the dispersion and absorption, rather than the more correct χ' and χ''.

Figure 6.1(a) shows a typical EIT situation. A spectral window opens in the absorption spectrum along with a high slope in the dispersion. The high slope is associated with a high group index. The point of zero detuning is at the moment the only one of interest to us, as our CW fields only have frequency components at this frequency. This example is for decay rates in the lower end of the range given by table 6.1. The Rabi frequency of the coupling field has been set to 50 GHz, which means that $|\Omega_\mathrm{c}| \gg \gamma_{12}, \gamma_{13}$.

In figure 6.1(b) we have raised the decay rates by a factor of 10. We see the same qualitative shape of the dispersion and absorption as in figure 6.1(a) except that the peaks are now of lesser peak value and wider. Notice that the ordinate axis has shifted down by a factor of 10. Actually, at zero detuning the slope of χ' is almost the same as for the prior figure, however the absorption has gone up by a significant amount.

More dramatic is the situation depicted in figure 6.1(c), where $\gamma_{12}, \gamma_{13} \gg |\Omega_\mathrm{c}|$. Here we see a radical departure from the EIT situation described in the previous plots. Instead of a window at $\frac{\Delta_\mathrm{p}}{|\Omega_\mathrm{c}|} = 0$ we now see a peak in the absorption and we have lost the transparency characteristic of the former examples. The material seems to have gone to a normal absorbing state. This happens as we increase γ_{12} and γ_{13} beyond the value of $|\Omega_\mathrm{c}|$. The width of the peaks increase as the decay rates increase and we understand why the decay rates are commonly known as linewidths, due to

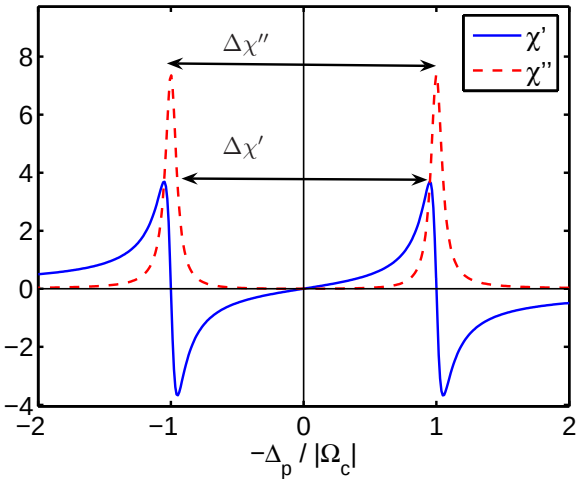

Figure 6.2.: *This figure indicates $\Delta\chi'$ and $\Delta\chi''$ given by eqs. (6.10) and (6.9) respectively.*

this effect.

As one might have noticed, the peaks in the absorption spectrum of the EIT states shown in figure 6.1(a) and 6.1(b) occur at a detuning around $\pm|\Omega_c|$. This is no coincidence and in fact these peaks are signatures of the level splitting of the second level in our QD system, due to the coupling laser. This splitting is discussed in further details in chapter 2. In appendix A.1 the width of this EIT *window* have been calculated under the assumption that $\gamma_{13} \ll |\Omega_c|, \gamma_{12}$. The result of this approximation yields

$$\frac{\Delta\chi''}{|\Omega_c|} = 2. \tag{6.9}$$

The width of the *inner* window in the dispersion has also been found

$$\frac{\Delta\chi'}{|\Omega_c|} = \sqrt{\frac{\gamma_{12}}{|\Omega_c|} + 4} - \frac{\gamma_{12}}{|\Omega_c|}. \tag{6.10}$$

We see that the peaks do occur at $\pm|\Omega_c|$. The assumption that $\gamma_{13} \ll |\Omega_c|, \gamma_{12}$ will be discussed in the dynamic analysis performed in chapter 7, for reasons that will be apparent shortly.

We now turn to the main subject of this chapter; how much can we expect to slow down our CW probe field, ie. alter its refractive group index. The general expression for the group index was derived in section 4.2. In section 6.3 we presented an explicit expression for n_g for the case of zero detuning for both fields, as the effect of EIT is largest for this setting. The variable will now be $|\Omega_c|$ or actually the field strength, E_c of the coupling field. This parameter will be easily controllable from the outside of a given future optical device, so naturally it is important and interesting to know the effect of this on n_g. As seen in from figure 6.1 even at $\Delta_p = 0$ the absorption does not drop to zero, except for the ideal case of $\gamma_{13} = 0$. This non-zero absorption is a trade-off in using EIT to obtain slow light. This will be much more apparent in the dynamic analysis. To illustrate the absorption associated with slow-light, n_g and χ'' are presented in the same figures for easy comparison.

In figure 6.3(a) we have plotted the situation where $\gamma = \gamma_{12} = \gamma_{13}$ and γ has then been varied in each of the four series. For the red series we notice a group index of almost 10^6, but also a

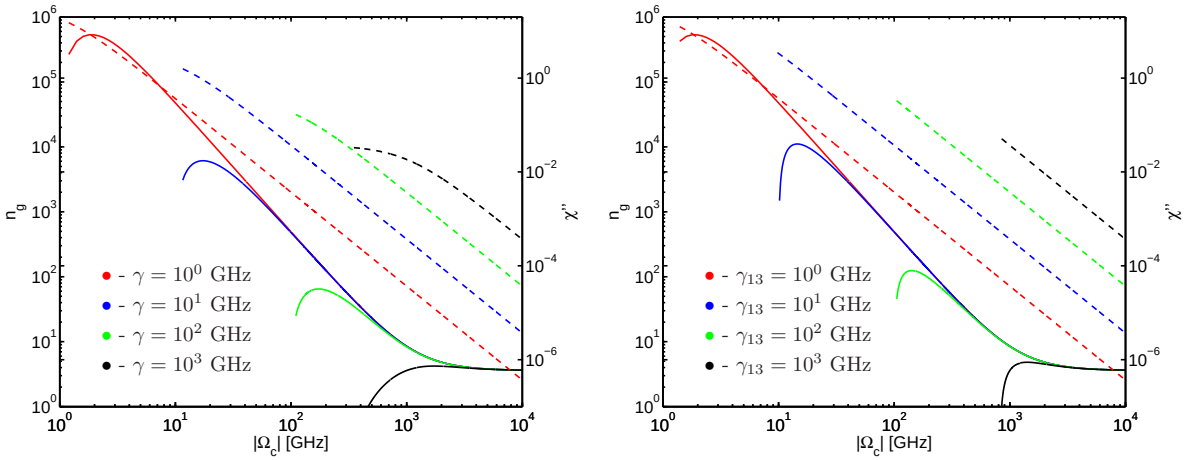

(a) For this plot γ_{12} and γ_{13} are equal to γ in each of the four series.

(b) Here γ_{12} has been fixed to 10^0 GHz, while is γ_{13} varied.

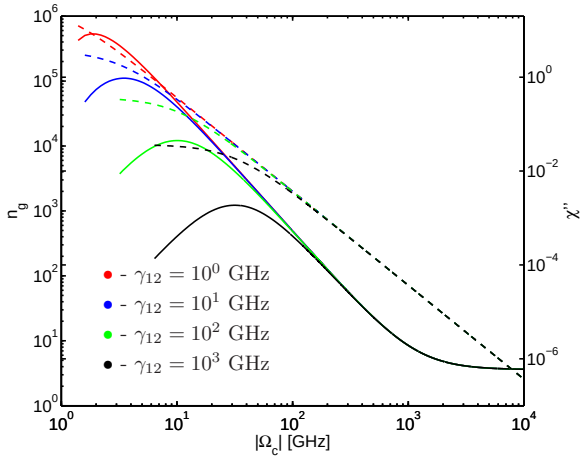

(c) Here γ_{13} has been fixed to 10^0 GHz, while is γ_{12} varied.

Figure 6.3.: *The refractive group index, eq.* (6.8)*, and absorption, eq.* (6.7)*, of the probe field for different decay rates, plotted against the Rabi frequency of the coupling field. The dashed line is the absorption,* χ''*, and the solid line is the refractive group index.*

correspondingly high absorption. As we increase the decay rates through the blue, green, and black series, we see that the maximum slow down decreases. For higher $|\Omega_c|$ yet, n_g join with the curves from the previous series. However, the absorption curves do not join, as the n_g curves did. They remain large for a high decay rate even though the corresponding group indexes are the same. For very high $|\Omega_c|$ the group index for all series tends to the background group index, n_b, at a value of 3.6. This happens as the $|2\rangle$ level gets more and more split, the slope in χ' will tend to zero and n_g tends to the background value. The series for the group index are not plotted for the entire $|\Omega_c|$ range as one might have noticed. This cut-off is due to the fact that just left of the peak in the group index, its value decreases very rapidly and eventually becomes smaller than 1 and it even passes through zero. This is caused by limitations in the group index definition, as discussed in section 4.2.

Figure 6.3(b) illustrates the case where γ_{12} has been fixed to 1 GHz and γ_{13} is varied. Comparing this figure to figure 6.3(a) we see both quantitative and qualitative likeness, same trends in n_g and χ'' for high coupling field. This indicates that the significance of γ_{13} is larger than that of γ_{12}. In figure 6.3(c) we have the situation of γ_{13} being held fixed at 1 GHz, while γ_{12} is varied. Here we see something really interesting, the peaks in the series for n_g have all moved toward the same value of $|\Omega_c|$, where it is equal to the fixed value of γ_{13}. The curves for n_g join up at much lower values of $|\Omega_c|$ than in the former figures. The absorption curves also tend toward the same curve, namely that characteristic of $\gamma_{13} = 1$ GHz. The independence of γ_{12} is clear at a Rabi frequency of around 100 GHz corresponding to a group index of almost 2500, which is still a fairly high slow down.

An important conclusion that can be drawn from the analysis above is well illustrated in the subfigures of figure 6.3. Namely that the refractive group index and absorption experienced by a CW (or very broad pulse) field mainly depend on the decay rate γ_{13}. This is rather surprising since the $|1\rangle \leftrightarrow |3\rangle$ is not a dipole-allowed transition and one could expect the significance of γ_{12} to be more pronounced, since this is the transition the probe couples to. One can also conclude that in order to see the effect of EIT, the Rabi frequency of the coupling must larger than both γ_{12} and γ_{13}. Physically this means that the level splitting $|2\rangle$ must be larger than the linewidth of the two dressed states.

7. Dynamic Analysis

Now that we have gained some insight of how the system behaves in the steady state solution for various parameters, we want to go one step further. We solve the dynamic case where we include the coupling between the Bloch and Maxwell equations and allow the probe field to have an arbitrary pulse shape. The coupling field we still consider to be a high intensity CW wave.

The coupling between the two different sets of equations arises from the fact that both electric fields induce dipole oscillations in the QD material. These dipoles give rise to a polarization which is the source term in the wave equation. The mathematical description is a system of coupled non-linear PDEs consisting of the Bloch equations (5.11) and the wave equation (4.1), which can only be solved numerically.

Solving this system of coupled PDEs both in time and space (1D), we are able to verify whether the steady state solution gives correct predictions when applied to more realistic situations. For example when a pulse train of pulses is sent through the material, we are able to see if the pulses change shape or are completely destroyed by dipole oscillations.

7.1. The slowly varying envelope approximation

To describe the full dynamics of the system we need to return to the general description of the electric field described by an envelope and a phase, eq. (5.7). The coupling field is taken to be a high intensity CW field, compared to the probe, which have been on for all times. This ensures that the coupling field and the material have reached a state in which EIT is possible. Being much stronger than the probe, we can neglect any changes in the coupling field and remove the dependence of x and t from $\mathcal{E}_\mathrm{c}$ and ϕ_c. The total field is now given by

$$E(x,t) = E_\mathrm{p}(x,t)\cos(k_\mathrm{p}x - \omega_\mathrm{p}t + \phi_\mathrm{p}(x,t)) + \mathcal{E}_\mathrm{c}\cos(k_\mathrm{c}x - \omega_\mathrm{c}t). \tag{7.1}$$

The field is polarized in the y-direction and travel along the x-axis. For mathematical convince we take all unknown functions to implicitly be defined as $f \equiv f(x,t)$; remembering that $\mathcal{E}_\mathrm{c}$ is not a function.

This is the most intuitive way to think of a time dependent electric field, as we have separated the underlying oscillations and the envelope. It allows for a general description, as E_p and ϕ_p are dependent functions. Going through the calculation in this section with this representation we will end up with two PDEs, one for E_p and ϕ_p. The equation for ϕ_p turns out to be highly singular and non-linear. It effectively transforms the system into a differential-algebraic system, which is difficult to solve numerically. None of our implementations could handle this system.

Alternatively, we can rewrite the probe field in the notation of eq. (5.8), in terms of a complex envelope: $\tilde{E}_\mathrm{p} = E'_\mathrm{p} + iE''_\mathrm{p} = E_\mathrm{p}\cos\phi_\mathrm{p} + iE_\mathrm{p}\sin\phi_\mathrm{p}$. The total field now reads

$$\begin{aligned} E &= \frac{1}{2}\tilde{E}_\mathrm{p}e^{i(k_\mathrm{p}x-\omega_\mathrm{p}t)} + \frac{1}{2}\tilde{E}^*_\mathrm{p}e^{-i(k_\mathrm{p}x-\omega_\mathrm{p}t)} + \mathcal{E}_\mathrm{c}\cos(k_\mathrm{c}x-\omega_\mathrm{c}t) \\ &= E'_\mathrm{p}\cos(k_\mathrm{p}x-\omega_\mathrm{p}t) - E''_\mathrm{p}\sin(k_\mathrm{p}x-\omega_\mathrm{p}t) + \mathcal{E}_\mathrm{c}\cos(k_\mathrm{c}x-\omega_\mathrm{c}t). \end{aligned} \tag{7.2}$$

To go back to the representation of (7.1), we can utilize the usual relations for complex numbers,

$$E_\mathrm{p} = |\tilde{E}_\mathrm{p}| = \sqrt{E'^2_\mathrm{p} + E''^2_\mathrm{p}}, \quad \phi_\mathrm{p} = \arctan\left(\frac{E''_\mathrm{p}}{E'_\mathrm{p}}\right).$$

Similarly we can write the polarization in complex envelope notation $P = \frac{1}{2}(U+iV)e^{i(kx-\omega t)} + c.c.$. This can be rewritten to sine and cosine as $P = U\cos(ky-\omega t) - V\sin(ky-\omega t)$, which comes in handy when we have to compare to the quantum model. The two fields drive the dipoles, so we expect that these will oscillate near the carrier frequencies of the fields. If we write a contribution to the polarization of frequency ω_p and ω_c, we can expect to get four slowly varying envelopes. The coupling field is assumed to have reached steady state and the corresponding dipoles will oscillate in resonance, out of phase with the field, and we can assume $\mathcal{U}_\mathrm{c}$ and $\mathcal{V}_\mathrm{c}$ to be constant[1]. The total polarization then becomes,

$$P = U_\mathrm{p}\cos(k_\mathrm{p}x-\omega_\mathrm{p}t) - V_\mathrm{p}\sin(k_\mathrm{p}x-\omega_\mathrm{p}t) + \mathcal{U}_\mathrm{c}\cos(k_\mathrm{c}y-\omega_\mathrm{c}t) - \mathcal{V}_\mathrm{c}\sin(k_\mathrm{c}y-\omega_\mathrm{c}t). \tag{7.3}$$

Using the envelope notation we have encapsulated the fast underlying oscillations in the sine and cosine, and the envelopes will be slowly varying. This is a tremendous advantage in the numerical solution process as we can solve for the envelopes when applying the slowly varying envelope approximation (SVEA). To arrive at the approximate equations we insert (7.3) and (7.2) into the wave equation, (4.1),

$$\frac{\partial^2}{\partial x^2}E - \frac{n_\mathrm{b}^2}{c^2}\frac{\partial^2}{\partial t^2}E = \mu_0\frac{\partial^2}{\partial t^2}P.$$

Using that sine and cosine are linear independent we get two complicated non-linear PDEs. These turn into simple form under the SVEA. In this it is assumed that all space and time derivatives of the envelopes are slow compared to the underlying oscillations. This is a good approximation as long as the envelope pulse width does not narrow down to femtoseconds. In mathematical terms this imply that $\partial F/\partial t \ll \omega F, \partial F/\partial x \ll kF, \partial^2 F/\partial t^2 \ll \omega\partial F/\partial t, \partial^2 F/\partial x^2 \ll k\partial F/\partial x$, where F represent the four envelope functions [13]. In practice we end up removing all non-linear and 2. order terms and thereafter applying the SVEA a few times. See appendix A.7 for calculations. The result is two simple wave equations of first order,

$$\frac{\partial E'_\mathrm{p}}{\partial x} + \frac{n_\mathrm{b}}{c}\frac{\partial E'_\mathrm{p}}{\partial t} = -\frac{\mu_0\omega_\mathrm{p}c}{2n_\mathrm{b}}V_\mathrm{p}, \tag{7.4a}$$

$$\frac{\partial E''_\mathrm{p}}{\partial x} + \frac{n_\mathrm{b}}{c}\frac{\partial E''_\mathrm{p}}{\partial t} = \frac{\mu_0\omega_\mathrm{p}c}{2n_\mathrm{b}}U_\mathrm{p}. \tag{7.4b}$$

[1] This is not truly correct as σ_{23}, which drives the polarization for the $|2\rangle \leftrightarrow |3\rangle$ transition is not zero. But in the limit of a strong field it is very small and can be neglected.

To find U_p and V_p we use the same procedure as for $\tilde{\chi}$ in section 6.2. Inserting the full transformation of the off-diagonal elements, (5.10), into the polarization, (6.2), and rewriting to sine and cosine we get the following polarization experienced by the probe

$$P_\mathrm{p} = N\langle d_\mathrm{p}\rangle = -N\left([\sigma_{12}\mu_{21} + \sigma_{21}\mu_{12}]\cos(k_\mathrm{p}x - \omega_\mathrm{p}t) - i[\sigma_{12}\mu_{21} - \sigma_{21}\mu_{12}]\sin(k_\mathrm{p}x - \omega_\mathrm{p}t)\right).$$

We can immediately read off the expressions for U_p and V_p,

$$V_\mathrm{p} = -iN(\sigma_{12}\mu_{21} - \sigma_{21}\mu_{12}) = 2\mu_{21}N\mathrm{Im}[\sigma_{12}], \tag{7.5a}$$
$$U_\mathrm{p} = -N(\sigma_{12}\mu_{21} + \sigma_{21}\mu_{12}) = -2\mu_{21}N\mathrm{Re}[\sigma_{12}]. \tag{7.5b}$$

Above it has been used that μ_{12} and μ_{21} are complex conjugates and real.

The total coupled system now consist of eight PDEs. Two wave equations and the Bloch equations, all in all eight unknowns, ρ_{11}, ρ_{22}, ρ_{33}, σ_{12}, σ_{23}, σ_{13}, E'_p and E''_p. The envelope functions couples to the Bloch equations through Ω_p and Ω_c which are given by

$$\Omega_\mathrm{p} \equiv \frac{\mu_{12}\tilde{E}^*_\mathrm{p}}{2\hbar}, \quad \Omega_\mathrm{c} \equiv \frac{\mu_{23}\tilde{E}^*_\mathrm{c}}{2\hbar}.$$

The system is non-linear now that Ω_p and Ω_c are dependent functions. This makes the system unsolvable analytically and quite a task to do numerically.

7.2. Numerical implementation

To simplify the description in the numerical analysis, the total system can be written in the form

$$\frac{\partial \mathbf{u}}{\partial t} = \nabla\mathbf{\Gamma}(x,t,\mathbf{u}) + \mathbf{F}(x,t,\mathbf{u}),$$

where $\mathbf{u}$ is the solution vector containing all the unknowns. Writing it in this form makes it easy to point out strategies to solve the problem. We need a method to calculate the space derivatives of $\mathbf{\Gamma}$ and a method for forward time stepping. For the spatial part methods like finite difference (FD), finite element (FEM) or spectral methods (SM) are suitable. One could also discretize the whole time domain and use any of these methods, but we loose the ability to take variable step size and thus control the error. When making a space discretization of $\mathcal{N}$ points, we get 8 unknown for each space point and $\mathbf{u}$ would contain $8\mathcal{N}$ elements, and looks like

$$\mathbf{u} = [E'_{\mathrm{p},1},\ldots,E'_{\mathrm{p},\mathcal{N}},\ E''_{\mathrm{p},1},\ldots,E''_{\mathrm{p},\mathcal{N}},\ \rho_{11,1},\ldots,\rho_{11,\mathcal{N}},$$
$$\rho_{22,1},\ldots,\rho_{22,\mathcal{N}},\ \rho_{33,1},\ldots,\rho_{33,\mathcal{N}},\ \sigma_{12,1},\ldots,\sigma_{12,\mathcal{N}},\ \sigma_{13,1},\ldots,\sigma_{13,\mathcal{N}},\ \sigma_{23,1},\ldots,\sigma_{23,\mathcal{N}}]^T.$$

T denotes the vector transposed. $\mathbf{\Gamma}$ has only nonzero terms for the elements concerning E'_p and E''_p, as only these have spatial derivatives. Hence it is given by

$$\mathbf{\Gamma} = [E'_{\mathrm{p},1},\ldots,E'_{\mathrm{p},\mathcal{N}},\ E''_{\mathrm{p},1},\ldots,E''_{\mathrm{p},\mathcal{N}},\ldots,0,\ldots]^T.$$

In the actual implementation $\nabla\mathbf{\Gamma}$ will be calculated separately.

$\mathbf{F}(x,t,\mathbf{u})$ is a vector function containing the right hand side of both the Bloch and wave equations.

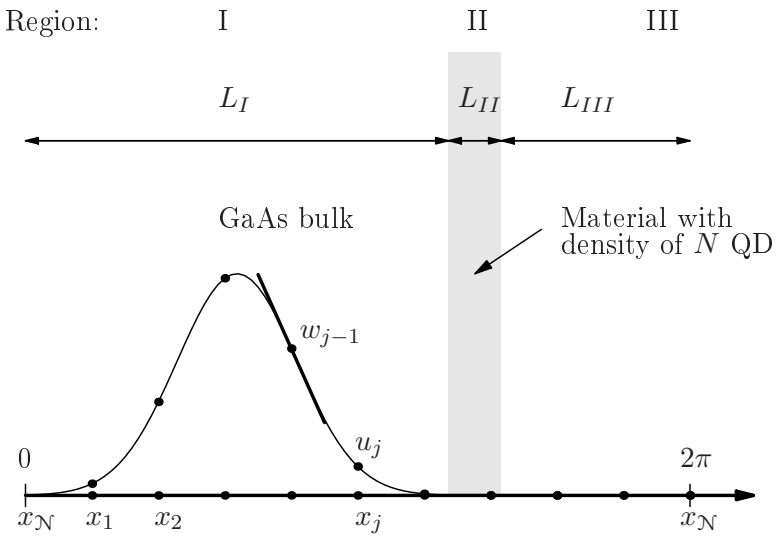

Figure 7.1.: *A sketch of the solution domain, and some parameters*

Figure 7.1 shows a simplified sketch of our solution domain including a solution for E'_{p}. We label the discrete points, x_j, the corresponding approximate solution, u_j, and the approximate derivatives, w_j. To simplify the notation, we have divided the solution domain into three different regions; Region I, before the material, region II, the material itself, and region III after the material. Each region has the length shown on the figure. The sketch represents the final setup with the 2π periodicity included.

The goal of the implementation is to simulate one or more pulses as they propagate through the domain, being initiated in region I. No matter what method we choose, a smooth pulse shape can only be described accurately by a minimum number of space points. This is limited by the minimum width of the pulse in region II. For spectral methods this is around 3-5 and for FEM and FD 10-20. These considerations are important as our pulses get squeezed under slow down.

Moreover, the transition into region II requires a lot of points to describe, as the QD density changes very rapidly and so does the envelope. These effects imply that to get an accurate solution we need a large number of space points. A simulation of this is shown in figure 7.2, where we see a pulse while it propagates at different times. Notice the periodic boundary condition which we will comment on later.

The initial pulses are implemented through a initial condition, $E'_{\mathrm{p}}(x,0) = g(x)$. The active material is modelled by making the QD density parameter, $N(x)$, into a square function in x. The initial condition for the electron population is that the ground state is fully occupied. As there are no QDs outside region II, this is given by the same square function dependence as $N(x)$. All other unknowns are initiated to 0.

7.2.1. The breakdown of FEMLAB

Initially we tried to implement the equations in Femlab v3.1, due to the great success in solving the envelope equation for the QD (see section 3.3). Femlab is a multipurpose program designed to solve coupled systems of PDEs, through different implementations of the FEM method in

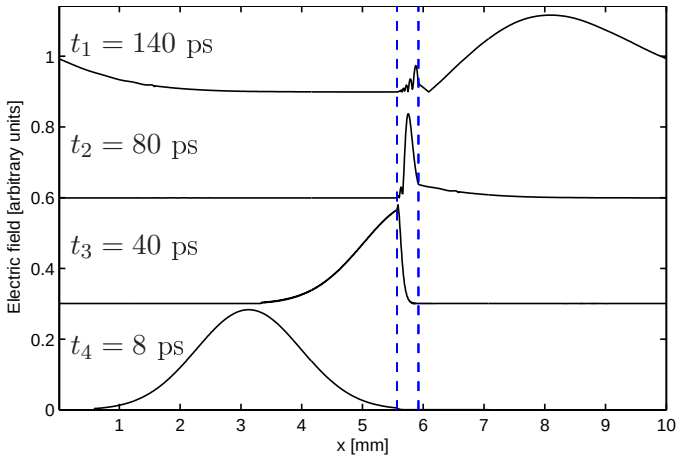

Figure 7.2.: *Different states of a pulse while it propagates through region II, with a refractive group index of 60. Notice the effect of the periodic boundary conditions and that it has been broadened due to dispersion.*

space and implicit time stepping methods. It sounded like an ideal solution for implementing the problem, but turned out to prove some difficulty. In the end we actually gave up in using FEMLAB to implement the whole dynamic system and instead decided to write our own solver based on spectral methods.

FEMLAB has a large collection of build in differential equations, but none of which suited us. All implementation in FEMLAB has been carried out using the general mode in which any PDE can be expressed in the form;

$$\mathbf{M}\frac{\partial \mathbf{u}}{\partial t} + \nabla \mathbf{\Gamma} = \mathbf{F},$$

which fully matched our needs. $\mathbf{M}$ is a mass matrix which is allowed to be singular and $\mathbf{u}$ is the solution vector. $\mathbf{\Gamma}$ and $\mathbf{F}$ are arbitrary vector expressions which can contain the solutions themselves and their time and space derivatives. The boundary condition and initial values are expressed in a similar manner. We will not go into the theory of FEM, just mention that the solution is found by discretizing the space domain in a number of points. The solution at each point is then approximated by a local polynomial of low order (typical 2-4) from which its derivatives is found. We will comment on the differences to spectral methods in the next section.

We started out by only implementing the dynamic Bloch equations for CW fields, hence leaving out the explicit space dependence. This we had easily solved earlier by the build in MATLAB function `ode45` for time stepping[2]. FEMLAB proved to do it just as easily and found the same solution at each point.

Implementing the envelope wave equation, leaving out the ϕ_{p} equation[3], the time stepping would not converge and the solution exploded in a matter of a few time steps. This got worse with increasing number of discrete space points, which is characteristic for unstable solutions.

The desired behavior is to get better accuracy by increasing the number of space points, $\mathcal{N}$, so that the error goes like some polynomial order $\mathcal{O}(\mathcal{N}^{-p})$, for a fixed $p > 0$. This is what normally

[2] An implicit forth order Runge Kutta method.

[3] Which turned out to be the difficult one to solve, as at that time we used the slowly varying envelope approximated version of eq. (7.1)

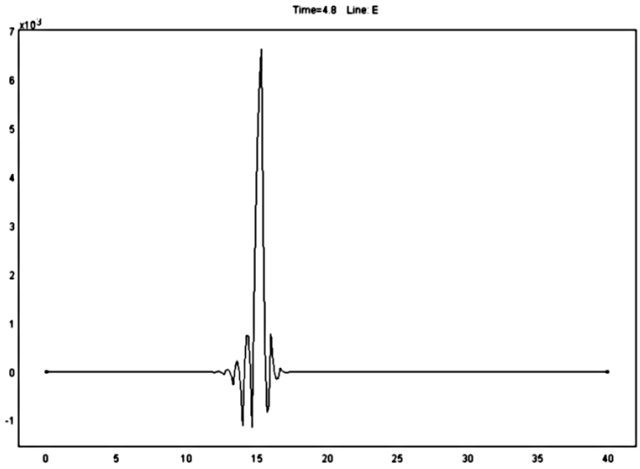

Figure 7.3.: *A* Femlab *solution supposed to be a pulse starting at* $x = 15$ *travelling towards a material beginning at* $x = 20$. *The figure shows that instead of travelling the pulse becomes unstable. To get a solution we have made the number of space discretization* $\mathcal{N}$ *small (64).*

happens. If the solution is unstable, small differences from the exact solution blow up and the accuracy is destroyed. None of our solutions managed to remain stable. Due to the low order polynomials we need a lot of points to describe a pulse. In figure 7.3 we see a Femlab solution at an early state of becoming unstable.

We managed, however, to solve a simple wave equation including a small damping term. Hence the other equations, combined with the large source term, seemed to have a great impact on the solution. This happened even though they should not be significant when the wave was outside the material.

7.3. Spectral methods

When Femlab failed to solve our PDE system we decided to do our own implementation. For the space discretization we used a spectral method and the `ode45` function in Matlab for time stepping. The main source of this implementation has been taken from [14], which has a good introduction to the subject. Our implementation is a rewritten example from [14], that includes our equations and use time-stepping function `ode45` for better accuracy. A more extended description of spectral methods is given in [15].

Spectral methods are in general methods which interpolate the solution by a global interpolant and calculates the derivatives from this approximate function[4]. Remark the difference to FEM, which uses local interpolants. In most aspects the spectral methods are superior to FEM, at the cost of flexibility. One of the advantages of spectral methods is that they take the approach of FEM and FD to the limit.

When calculating the derivative at a point x_j, instead of only including a set of neighboring points, all the points in the discretization are included. This gives much better accuracy, better

[4]That said, there exist spectral method not based on interpolation but on integration instead, so called non-interpolation spectral methods.

stability, and the need for fewer points. For solutions which have infinitely many continuously derivatives the error of the differentiation is characterized by the so called spectral or exponential order. This means that the error goes like $\mathcal{O}(\mathcal{N}^{-p})$ for all p's. Where p increases for increasing $\mathcal{N}$, which is a remarkable feature [14].

The interpolation function is most often a finite Fourier series or Chebyshev polynomials. As we are looking for wavelike solutions the Fourier basis is the obvious choice. Choosing the Chebyshev basis would force us to distribute the space points along the edge of the solution domain, which is a complete waste in our case as all details are located in the center.

The basic idea when approximating the derivative is to exploit that the derivative in real space can be found by multiplying by ik in Fourier space[5]. The strategy is to use the discrete Fourier transform (DFT) to transform discrete points in real space, multiply by ik, and use the inverse DFT to find the derivatives at each point, w_j.

$$u_j \xrightarrow{\text{DFT}} u_k \xrightarrow{ik} w_k \xrightarrow{\text{IDFT}} w_j$$

In the actual implementation we have used the fast Fourier transform (FFT) instead of DFT as it is faster.

Using this method we are forced to use periodic boundary condition as the finite Fourier series is 2π periodic. This is implicitly enforced by the solver, which is clearly seen in figure 7.2 and imposes some limitations of what can be simulated. It becomes a trade-off between how long time we want to simulate and how small structures we want to see.

A basic flowchart of the final implementation can be seen in figure 7.4. The dashed boxes represent the two key functions involved. The outer box is the `ode45` function which control the whole process and essentially does the time stepping. The inner box, is the right hand side of eq. (7.2) and gets called one or more times in each time step. It is responsible for calculation the time derivative at each time and contain the spectral method implementation.

[5]Whether you multiply by ik or $-ik$ depends on your definition of the Fourier transform. Multiplying by ik is the correct one when using the MATLAB `fft` function.

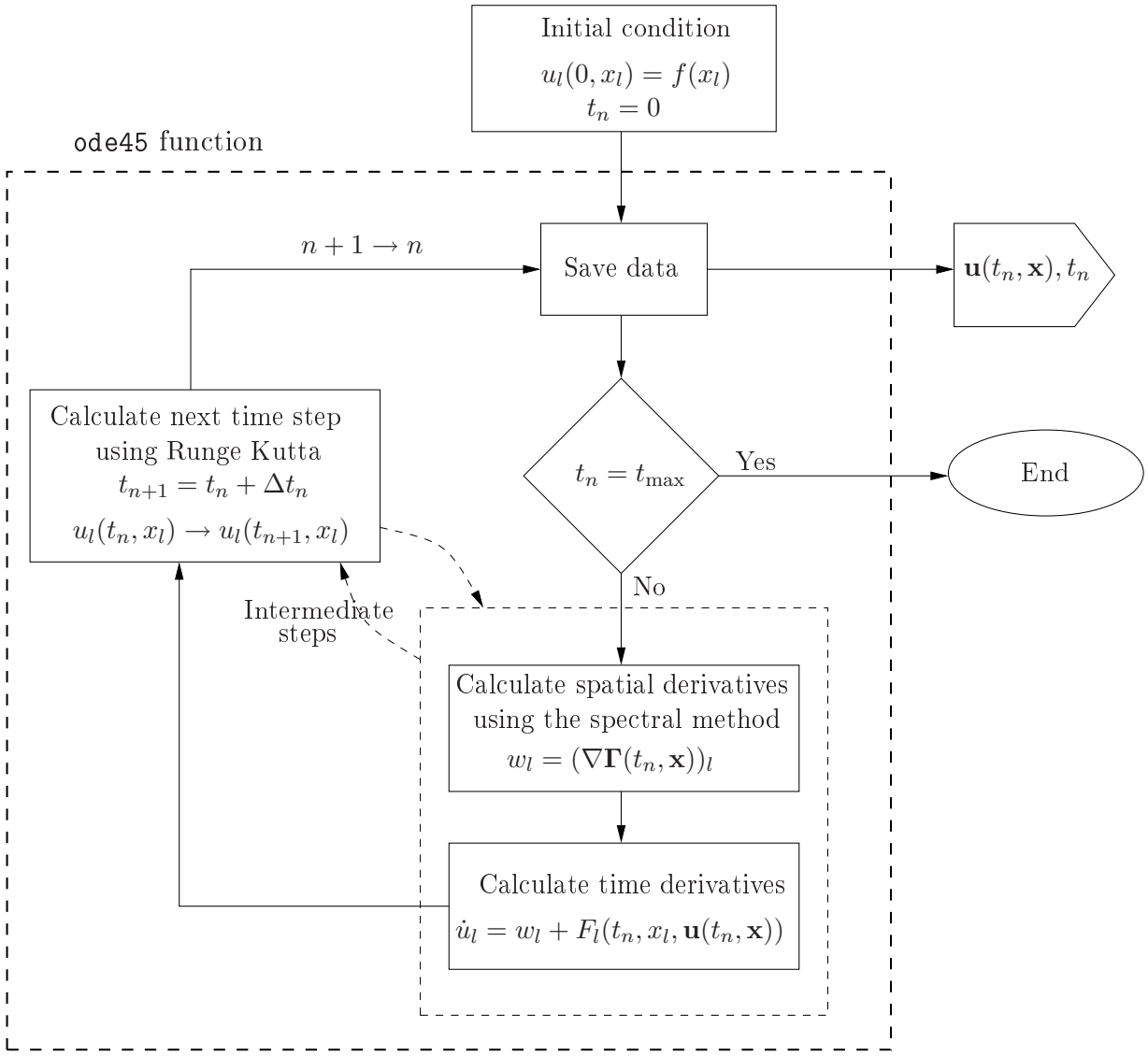

Figure 7.4.: *Flowchart for the simulation program.* $\mathbf{u}(t_n, \mathbf{x})$ *is the solution vector at the time step* t_n *and subscript* l *denotes the* l*th element belonging to the* l*th discretization point. The dot represent the exact time derivative at the time* t_n *and* w_l *is the spatial derivative of* $\mathbf{u}(t_n, \mathbf{x})$ *at each point .*

7.4. Verification of the implementation

In order to have confidence in our implementation we need to verify that it behaves correctly. This can be tested under simple conditions under which we can predict the behavior, and make sure that the solution converges when we increase $\mathcal{N}$. An obvious test would be for long pulses, which can be compared to the solutions in chapter 6. For zero amplitude coupling field we would expect nothing to happen except for a high absorption.

7.4.1. Verification of convergence

To verify the convergence we can solve a simple system where an exact solution is known and compare the two for different $\mathcal{N}$. The time stepping algorithm will of course have an influence too. However, in our case this is not significant as long as the solution converges. This is because the `ode45` solver can take variable time steps and hence keep the error within a chosen tolerance. If this tolerance is set to a small value like 10^{-13}, we will expect the solution to behave well down to this tolerance, if not corrupted by instabilities and rounding errors.

The simplest case we can solve analytically is a running envelope in the bulk material, ensuring that it does not cross the periodic boundary. In figure 7.5 the 2-norm of the error for such a calculation is shown in a double-logarithmic plot. The spectral order is clearly noticeable as the error decreases much faster than a straight line, almost down to the tolerance of the `ode45` solver, at $\mathcal{N} = 128$. This corresponds to 4 points for an entire pulse. For higher $\mathcal{N}$ yet, rounding errors come in to play. But what seems like a increase in the error, is mostly a more smooth distribution of the error. To represent the squeezed pulses in region II we will most often use between 512 and 1024 points.

7.4.2. Zero coupling field verification

The next step is to verify whether the solution behaves correctly for zero coupling field. In the absence of a coupling field the pulse will experience a damping like the one shown in figure 6.1(c).

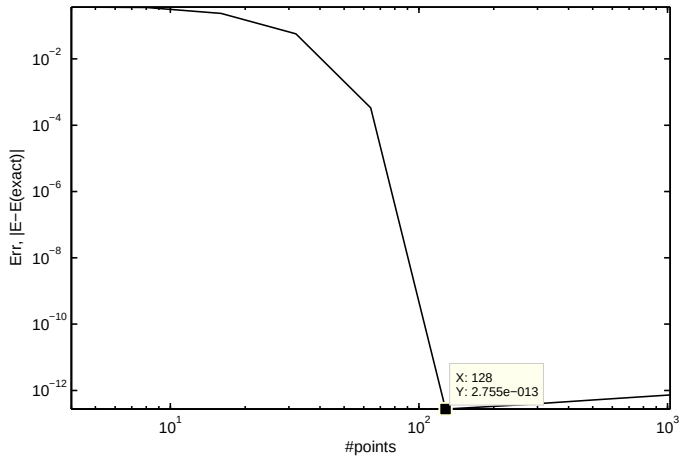

Figure 7.5.: *The 2-norm of the error for a small pulse which propagates in the bulk material, calculated at* $t = 50$ *ps.*

The splitting of the $|2\rangle$ state will not occur and the system will effectively behave as a two-level system. This means that the carrier population of the second level will start to change as the probe field now couples the two levels. We expect to see a high damping and not observe slow down different from the background refractive group index. To be able to see any effect we have set the QD density to 3×10^{20} m^{-3}, which is a order of magnitude lower than other plots in this chapter. Otherwise we will just observe complete damping in a very short distance. All pulses have a temporal width, $W_t = 15$ ps.

Solutions of the envelope and carrier population in the ground state are shown in figure 7.6 and 7.7. In figure 7.6(a) we see the expected behavior as the envelope gets damped and experience no slow down. From figure 7.6(b) we see that all the carriers no longer remain in the ground state, but are exited to the $|2\rangle$ state. This is calculated for $\gamma_{12} = 3000$ GHz which corresponds to room temperature, table 6.1.

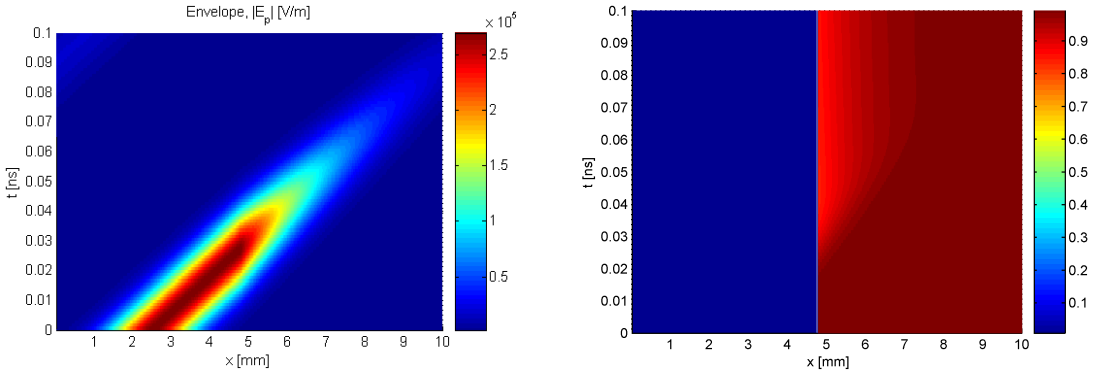

(a) The envelope function.

(b) The population of the ground state.

Figure 7.6.: *Verification of the model for $\Omega_c = 0$ and for $\gamma_{12} = 3000$ GHz. The solution corresponds to a two-level system with high absorption and no slow down.*

Lowering the dephasing to $\gamma_{12} = 3$ GHz, so that $\gamma_{12}^{-1} \ll W_t$, we should experience self induced transparency, which is seen in figure 7.7. This is another quantum phenomena which occurs in a two-level system. In it, a short pulse[6] will pass through a normally absorbing medium, like it was transparent and had a high group refractive index. After some damping it will reach a steady state and will keep its shape all along the propagation line. This shape can only correspond to certain areas under the envelope. If we start the pulse with a too small amplitude it will die away [13, sec. 15.4]. We can not expect the shape to fully remain constant as all the approximations are not completely met.

7.4.3. Steady state verification

Our last method to verify the implementation is to compare it with the Bloch equations, eq. (5.11), solved for a space independent CW coupling and probe field, not coupled to the wave equation. The probe field is turned on smoothly in time to simulate a very broad pulse approaching region II. Our new implementation should give the same results for the off-diagonal elements near the

[6] Compared to both the dephasing time and relaxing time of the carriers

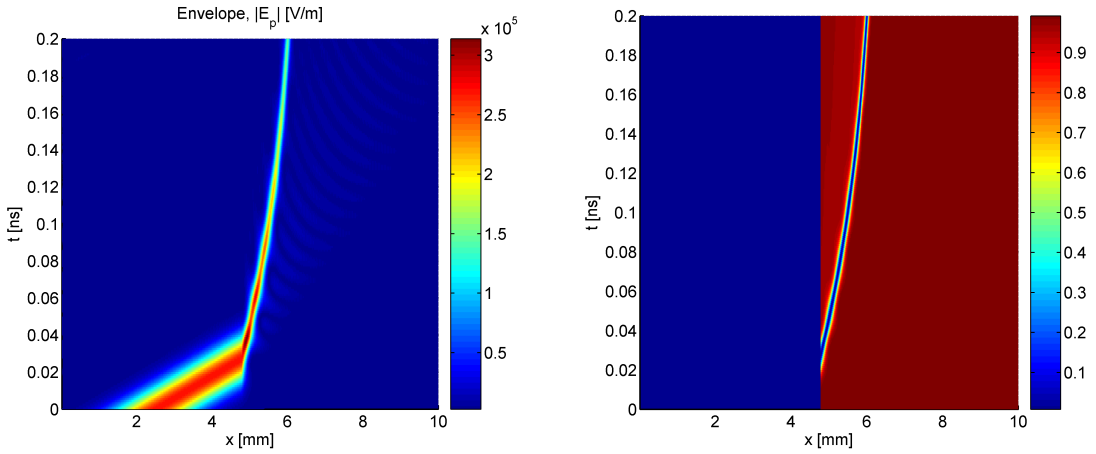

(a) The envelope function.

(b) The population of the ground state.

Figure 7.7.: *Verification of the model for $\Omega_c = 0$ and $\gamma_{12} = 3$ GHz, a situation in which self induces transparency is seen. The pulse continues to propagate even though it should experience a high damping.*

edge of the material for very broad pulses (approximate CW fields), like the one in figure 7.8(c). The two comparable solutions are shown in figure 7.8(a) and 7.8(b).

Having turned on the field smoothly we quickly obtain a steady state as compared to a more steep turn on which would cause a longer transient [6, p. 229]. To reach steady state we used a solution domain of 20 mm. The plots are not completely equal as one represents a pulse at a certain x value and the other represents a transient beginning of a CW field in a ultra thin material.

The peak value on both graphs only differs by 2.1×10^{-6} or an error of 0.5%, at the same t value. The steady state plateau differs by 1.4×10^{-6} which corresponds to and an error of 2.8%. The two solutions match each other well.

It should now be justified that the model behaves correctly and reproduces the desired solutions under the simple conditions which we can test. This indicates that the model and implementation can be trusted to produce the correct result with good accuracy.

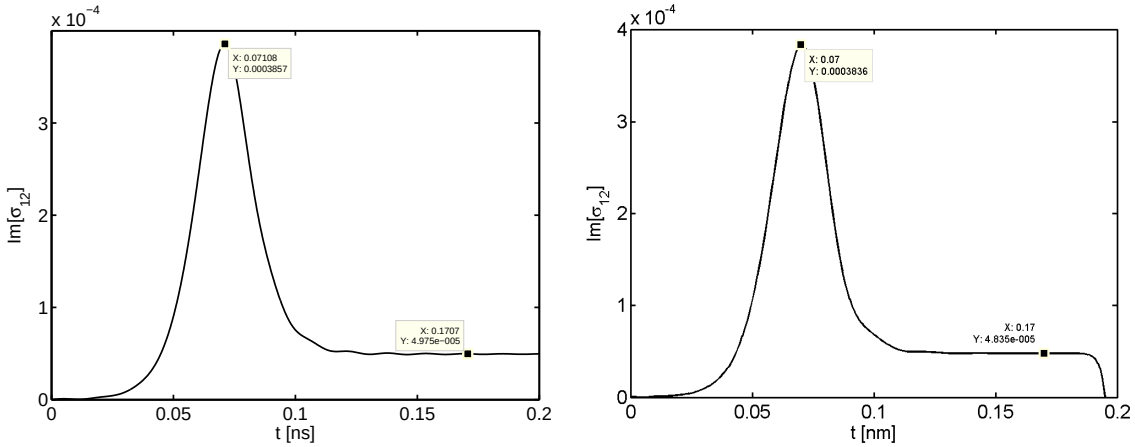

(a) Im $[\sigma_{12}]$ plotted for the uncoupled solution for CW fields

(b) The coupled solution of Im $[\sigma_{12}]$ plotted at a cross section near the edge of the material.

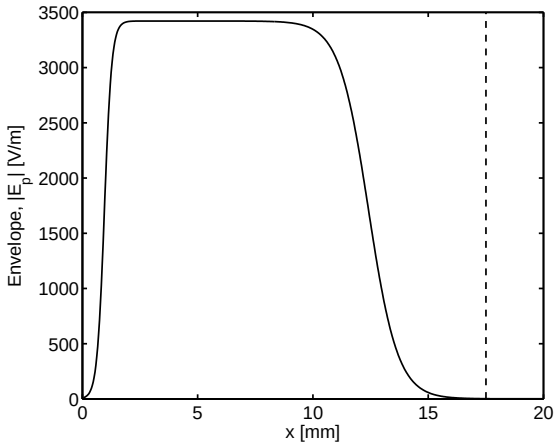

(c) The pulse used to verify the steady state solution

Figure 7.8.: *Verification of the implementation in the limit of a very broad pulse. The above calculations have been performed with* $\Omega_c = 400$ *GHz,* $\gamma_{12} = 40$ *GHz and* $\gamma_{13} = 4.55$ *GHz.*

7.5. Single pulse analysis

In the following section we will analyze the dynamic behavior of a single pulse, using the model developed in the previous sections. The model is based on the assumption that the complex envelope is slowly varying and for this function we can solve numerically. The complex envelope is however not as intuitive as the regular envelope. Hence the solutions presented in this section will be of the envelopes and not the complex ones. We will often refer to the envelope as the probe pulse, even though this is not strictly correct. The phase, ϕ_{p}, will generally not be given much attention as for zero detuning, $\Delta_{\mathrm{p}} = \Delta_{\mathrm{c}} = 0$, its value does not change (continuously), see appendix A.8. Under certain conditions the phase changes discontinuously, this rather peculiar phenomena is discussed in section 7.5.2.

The pulses we simulate will be Gaussians. The numerical implementation requires us to state an initial condition for the complex envelope, $\tilde{E}_{\mathrm{p}}(x, t = 0)$. For all simulations in this chapter the

initial condition will have the standard form:

$$E_{\mathrm{p}}^{'}(x,t=0)=\mathcal{E}_{\mathrm{p}}\exp\left[-2\ln 2\left(\frac{x-x_0}{W_x}\right)^2\right],\quad E_{\mathrm{p}}^{''}(x,t=0)=0, \tag{7.6}$$

where $\mathcal{E}_{\mathrm{p}}$ is a field strength, x_0 is center of the envelope, and finally W_x is the FWHM[7]. For a Gaussian we can obtain the constant characterizing the product between the real space width and the Fourier space width. This has been done in appendix A.4 and the result is,

$$W_xW_k=W_tW_\omega=4\ln 2. \tag{7.7}$$

Along with the background dispersion relation, $\frac{c}{n_{\mathrm{b}}}=\frac{W_\omega}{W_k}=\frac{W_x}{W_t}$, this gives the important relation connecting the width in real space and in frequency space:

$$W_xW_\omega=\frac{4\ln 2c}{n_{\mathrm{b}}}. \tag{7.8}$$

This relation will be useful in interpreting some of the results in this chapter, even though it is not valid in general.

As mentioned in section 7.1, the full set of equations governing the pulse consists of eight coupled differential equations. In analyzing the solution of a given parameter set, one ought to look at the solutions for all eight dependent variables. We will however focus on a few of these. The first is of course the envelope itself, E_{p}. Secondly the off-diagonal element σ_{12}, as this serves as a direct source term in the wave equation, see eqs. (7.4) and (7.5).

7.5.1. Wide pulses

We will start our analysis by considering spatially wide pulses, and correspondingly narrow frequency wise, through eq. (7.8). These resemble the CW fields considered in chapter 6 the most. By wide we mean that W_x should be large enough, so that W_ω will fit well inside the EIT window. In the limit were $W_x\to\infty$ the spectral width will tend to zero, $W_\omega\to 0$, and we are back to the case studied in chapter 6.

In the steady state analysis we had the luxury that quite a few parameters lost their significance under the assumption that $\Omega_{\mathrm{c}}\gg\Omega_{\mathrm{p}}$ (appendix A.2). For all calculations from this point we will adopt the following: $\frac{|\Omega_{\mathrm{c}}|}{|\Omega_{\mathrm{p}}|}=230\Rightarrow\mathcal{E}_{\mathrm{p}}\approx\frac{1}{51}\mathcal{E}_{\mathrm{c}}$. We need to assign values to the decay rates γ_{22}, γ_{33}, and γ_{23}. These were the ones who dropped out in the steady state analysis. The diagonal rates will be set so that: $\gamma_{22}=\gamma_{33}=2\times10^9$ Hz. This is lower than the off-diagonal rates, due to the fact that the off-diagonal elements experience dephasing and the diagonal elements do not. For the time being the off-diagonal decay rates will be set to: $\gamma_{12}=\gamma_{13}=\gamma_{23}=5\times10^{11}$ Hz. These values are reasonable according to table 6.1.

The frequencies of the probe and coupling field are set to achieve maximum effect of EIT, $\Delta_{\mathrm{p}}=\Delta_{\mathrm{c}}=0$, hence $\omega_{\mathrm{p}}=\omega_{21}$ and $\omega_{\mathrm{c}}=\omega_{32}$. These will of course change depending on the QD used. We will use frequencies corresponding to our reference QD, figure 3.4: $\omega_{\mathrm{p}}=9.647\times10^{14}$ Hz and $\omega_{\mathrm{c}}=2.203\times10^{14}$ Hz. The corresponding transition matrix elements are thus the same as used in the steady state analysis: $\mu_{21}=1.07\times10^{-28}$ Cm $=0.67\ e$ nm and $\mu_{32}=4.69\times10^{-28}$ Cm $=$

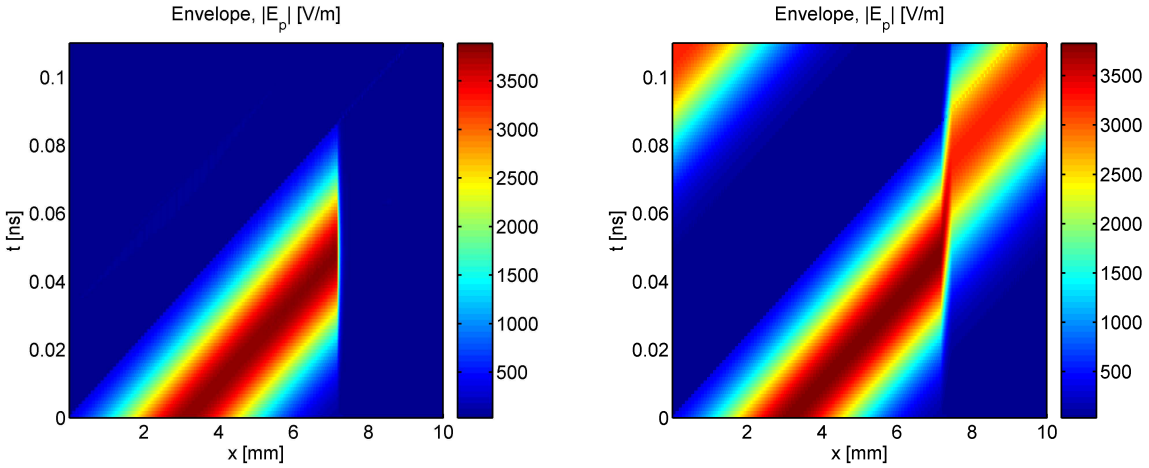

(a) The pulse is getting rapidly damped due to the high γ_{13}. Parameters: $\gamma_{13} = 5 \times 10^{11}$ Hz and $\Omega_c = 450$ GHz.

(b) The pulse is allowed to pass through region II due to low γ_{13}. Parameters: $\gamma_{13} = 5 \times 10^6$ Hz and $\Omega_c = 450$ GHz.

Figure 7.9.: *Two figures illustration the effect of γ_{13} on the absorption of a pulse. The width of the active area is: $L_{II} = 300$ μm.*

2.93 e nm. The density of QDs, N, has been set to 3×10^{21} m^{-3} and the background refractive index, n_b, is 3.6.

For the following simulations a value of $\Omega_c = 450$ GHz is used. This value does not yield the highest achievable value of n_g, see figure 6.3. It is necessary to limit the slow down, as the pulse width is roughly inversely proportional to n_g. Hence, a group index of 10^5 would compress a 2.39 mm pulse to 23.9 nm! In order to describe an envelope, the spectral method needs 3 to 5 discrete points over the envelope. Our calculation domain is 10 mm, so in order to describe the 23.9 nm envelope, we would need approximately $\frac{10 \text{ mm}}{23.9 \text{ nm}} \times 4 \approx 10^6$ points in our domain. This is beyond our computer capacity and the theory cannot describe pulses which vary appreciably over the size of a QD either. All in all we are forced to go for lower slow down, but in turn we get nicer illustrations.

In figure 7.9(a) a simulation is shown for a pulse of $W_x = 2.39$ mm, $\Omega_c = 450$ GHz and the rest of the parameters are as mentioned above. It shows how the pulse is damped very rapidly and nothing gets through region II, even though its width is only $L_{II} = 300$ μm. This result indicates that for the current parameter set, the absorption in region II is very high. As far as applications go, it is a serious problem that one cannot send signals through the slow down device.

From figure 6.3 one could suspect that it might be the high value of γ_{13} that causes the high absorption of the probe. In figure 7.9(b) we have solved for the same parameters except that we have lowered γ_{13} by a factor of 10^5 so that $\gamma_{13} = 5 \times 10^6$ Hz. Here the situation is completely different, the pulse is nicely slowed down in region II and comes out much less damped than for the high value of γ_{13}. One could speculate that in order to reduce the absorption, the density of QDs could simply be reduced. This does indeed lower the absorption, but unfortunately it also lowers the group index and you loose your ability to slow down the probe pulse.

[7] Full Width at Half Maximum, defined by: $|f(W_x/2)|^2 = \frac{1}{2}|f(x_{max})|^2$.

Quantity	Symbol	Value	Unit
Density of QDs	N	3×10^{21}	m^{-3}
Transition matrix element	μ_{12}	1.07×10^{-28}	Cm
Transition matrix element	μ_{23}	4.69×10^{-28}	Cm
Diagonal decay rates	γ_{22}, γ_{33}	2	GHz
Off-diagonal decay rates	γ_{12}, γ_{23}	50	GHz
Off-diagonal decay rate	γ_{13}	5	MHz
Probe field frequency	ω_p	9.647×10^{14}	Hz
Coupling field frequency	ω_c	2.203×10^{14}	Hz
Detuning	Δ_p, Δ_c	0	Hz
Rabi frequency coupling field	Ω_c	450	GHz
Rabi frequency probe field	Ω_p	1.96	GHz
Background refractive index	n_b	3.6	-
Length of region II	L_{II}	300	μm

Table 7.1.: *Parameters used in the dynamic simulation. These are to be considered as default values, if anything else is used it will be indicated.*

As a consequence of this discouraging result, we are forced to adopt a value of γ_{13} that is unnaturally low for a semiconductor QD[8], to be able to show some results. From this point on all calculations will be performed with $\gamma_{13} = 5 \times 10^6$ Hz. We will also lower the default value of the two off-diagonal elements by a factor of 10. Fortunately γ_{13} is mainly responsible for the absorption, so lowering this will hopefully not affect the solution much beside decreasing the absorption. γ_{12} is the decay rate for the dipole σ_{12}, which is the source of the wave equation. This means that we can still analyze a lot of interesting scenarios even γ_{13} has been set very low. The default parameters used in all simulations to follow are summarized in table 7.1.

As mentioned in the beginning of this section the limiting case of a very wide pulse corresponds to a CW pulse. This means that we can expect some agreement with the analysis performed in chapter 6. We have numerically calculated the group index for a range of wide pulses and the values obtained are in very good agreement with those from eq. (6.8). As long as the pulses are sufficiently wide.

We will now investigate when we can talk about a pulse being wide, in the sense that it basically behaves as a CW pulse. CW pulses have essentially zero width in frequency space, but as we decrease the pulse spatially we increase its spectral width according to eq. (7.8). For these wide pulses the spectral width is unchanged upon entering the active material. Depending on the parameters the value of χ'' and the slope of χ', can be the same for a range of frequencies. As long as the spectral width is contained within this range, it will behave as a CW pulse and we can expect the analytical results from the steady state analysis to be valid. Whether this can be fulfilled in the region II, is mainly determined by Ω_c, γ_{12}, and γ_{13} as discussed in section 6.4.

[8]Other atomic three-level systems exits where γ_{13} indeed is very low, eg. the Bose-Einstein condensates used by Lene Hau *et al.* [3].

7.5.2. Narrow pulses

Having examined wide pulses, we want go to the regime of spatially narrow pulses which in turn are wide spectrally. We will look at pulses that possess a spectral width larger than the EIT window of $2|\Omega_c|$. This means that we are far away from the CW case and qualitative as well as quantitative differences can be expected.

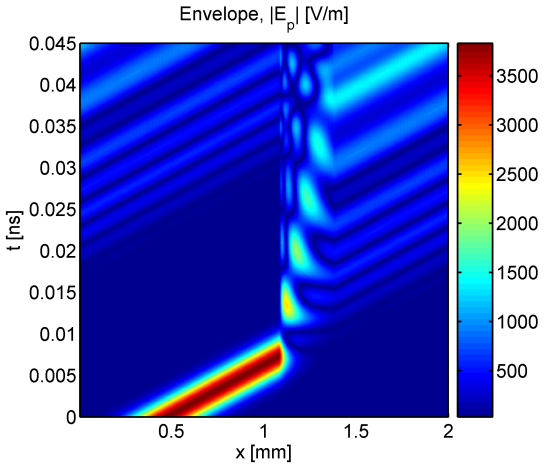

(a) Solution of the envelope for a narrow pulse of $W_x = 0.22$ mm and spectral width $W_\omega = 1042$ GHz. Other parameters: $\gamma_{12} = 10$ GHz and $\Omega_c = 450$ GHz.

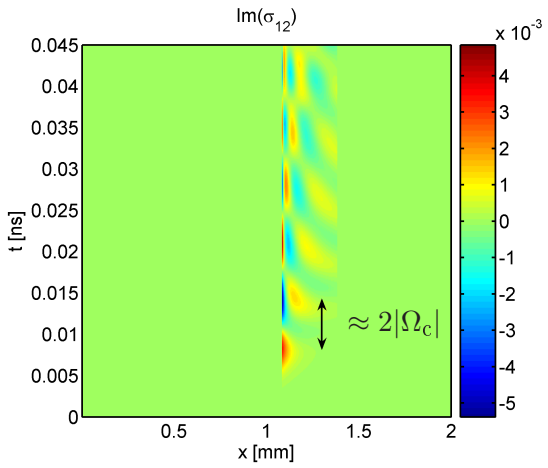

(b) Corresponding solution of $\mathrm{Im}\,[\sigma_{12}]$.

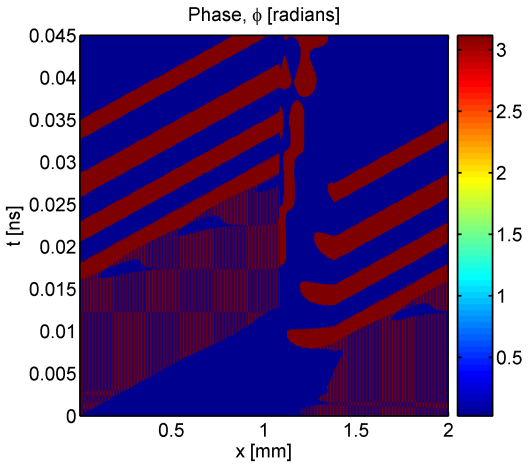

(c) Corresponding solution of ϕ_p.

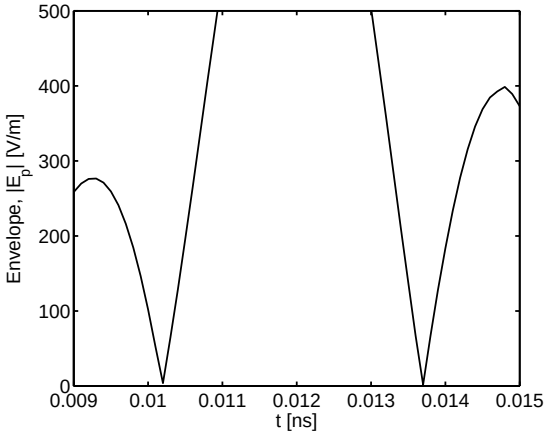

(d) Cross section of the solution in figure 7.10(a) at $x = 1.23$ mm, where the kinks in are E_p clear.

Figure 7.10.: *Solutions for a narrow pulse with* $\gamma_{12} \ll \Omega_c$.

In figure 7.10(a) we have solved for a $W_x = 0.22$ mm pulse with a spectral width of $W_\omega = 1042$ GHz, hence it has frequency components at $\pm\Omega_c$. The decay rate γ_{12} has been set to 10 GHz. The solution shows behavior much different from that of the wide pulses. The pulse is slowed down, but it seems like the envelope function has started oscillating. These oscillations are caused by the source term in the wave equation, $\mathrm{Im}[\sigma_{12}]$. $\mathrm{Re}[\sigma_{12}]$ never changes from its initial value of zero, as both detunings are zero (see appendix A.8). The corresponding solution for $\mathrm{Im}[\sigma_{12}]$

is shown in figure 7.10(b), and indeed this oscillates with a frequency of approximately $2|\Omega_c|$ (indicated by black arrow). We suspect these oscillating dipoles to be a response from the split $|2\rangle$ state, now that the probe has frequency components directly at these two levels. The equation of motion for σ_{12} is now driven by terms with frequencies $\pm|\Omega_c|$. These are resonant with the two split levels and the equation responds with large oscillations. These in turn affect the envelope which also starts oscillating, but it lags a bit after $\mathrm{Im}[\sigma_{12}]$ as does not have instantaneously effect. The appearance of the frequency $2|\Omega_c|$ can be interpreted as a beat frequency, as it corresponds to the difference between the two.

In the domain where $2|\Omega_c| \ll W_\omega$ one do not observe the $2|\Omega_c|$-frequency in connection with the envelope itself. But rather in the oscillations of the dipoles after the pulse has passed a certain x point. We can expect this from a pulse being spectrally much wider than the splitting. It will only interact weakly with the two split levels, as it is only a very small number of all the frequency components that actually see the two levels.

Oscillating envelopes are not an everyday sight and it could be interesting to see how the phase behaves. The phase is shown in figure 7.10(c). Focus should be on the data in the right side of the figure as the rest are numerical artifacts[9]. The solution shows that the phase changes discontinuously between 0 and π. We can understand that this happens by noting that $\mathrm{Im}[\sigma_{12}]$ is the only source term in the equation for E_p'. Hence if the value of $\mathrm{Im}[\sigma_{12}]$ changes from a value to another large value of opposite sign, E_p' will change sign too. This means that E_p' can pass through zero and the envelope, E_p, will have to become zero too ($E_p = |E_p'|$ as $E_p'' = 0$ due to zero detuning).

It seems strange that a nice physical quantity like the phase can be discontinuous. We can understand this from the requirement that the entire field must differentiable. We can write the entire probe field as

$$E_{\mathrm{probe}} = E_p \cos(k_p x - \omega_p t + \phi_p),$$

differentiating this with respect to x and t yields

$$\frac{\partial E_{\mathrm{probe}}}{\partial x} = \frac{\partial E_p}{\partial x}\cos(k_p x - \omega_p t + \phi_p) - E_p \sin(k_p x - \omega_p t + \phi_p)(k_p + \frac{\partial \phi_p}{\partial x}),$$
$$\frac{\partial E_{\mathrm{probe}}}{\partial t} = \frac{\partial E_p}{\partial t}\cos(k_p x - \omega_p t + \phi_p) - E_p \sin(k_p x - \omega_p t + \phi_p)(-\omega_p + \frac{\partial \phi_p}{\partial t}).$$

At the x and t points where the phase jumps, the envelope is zero. Using this to simplify we get

$$\frac{\partial E_{\mathrm{probe}}}{\partial x} = \frac{\partial E_p}{\partial x}\cos(k_p x - \omega_p t + \phi_p),$$
$$\frac{\partial E_{\mathrm{probe}}}{\partial t} = \frac{\partial E_p}{\partial t}\cos(k_p x - \omega_p t + \phi_p).$$

From this it is clear that if the phase suddenly changes by π, both of these will change sign. If they are to remain continuous, the slope of E_p in x and t would have to change sign, corresponding to a kink in E_p along a certain x or t direction. Figure 7.10(d) shows a cross section at $x = 1.23$ mm of the solution in figure 7.10(a), where it is indicated that we actually do have these kinks.

[9] The vertical lines are fluctuations around $\phi_p = 0$ and the left side is due to the 2π-periodicity.

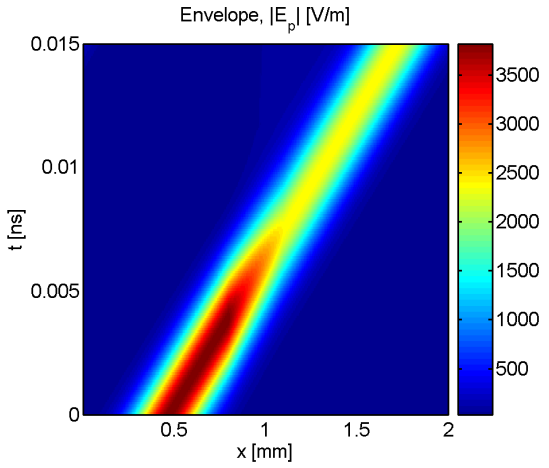

(a) Solution of the envelope for a narrow pulse of $W_x = 0.22$ mm and spectral width $W_\omega = 1036$ GHz. Other parameters: $\gamma_{12} = 10000$ GHz and $\Omega_c = 450$ GHz.

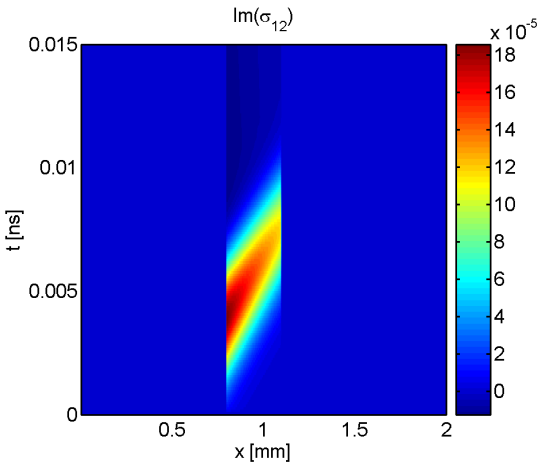

(b) Corresponding solution of $\mathrm{Im}\,[\sigma_{12}]$.

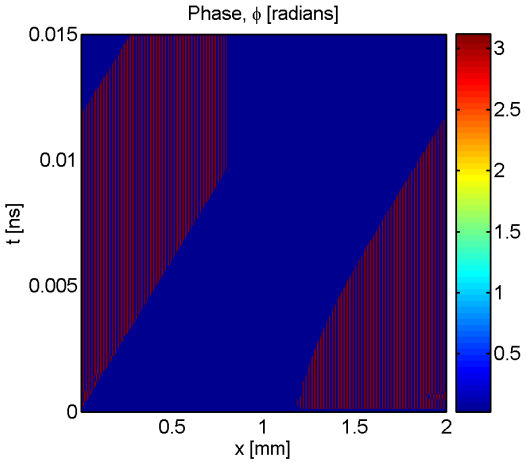

(c) Corresponding solution of ϕ_{p}.

Figure 7.11.: *Solutions for a narrow pulse with* $\gamma_{12} \gg \Omega_c$.

Comparing to the wide pulse in figure 7.9, this narrow pulse is poorly transmitted through region II (the width L_{II} is of course held fixed). This is due to its large spectral width extending beyond the EIT window of $2|\Omega_{\mathrm{c}}|$ and the hence the narrow pulse will experience absorption and dispersion.

We will now consider the same narrow pulse as above, but set $\gamma_{12} = 10000$ GHz so that $\gamma_{12} \gg \Omega_{\mathrm{c}}$. In the above example we had the opposite case, $\gamma_{12} \ll \Omega_{\mathrm{c}}$. The solutions are shown in figure 7.11. Figure 7.11(a) shows the envelope being damped as it passes through region II, however its group index does not seem to be affected. The dipole $\mathrm{Im}\,[\sigma_{12}]$, illustrated in figure 7.11(b), does not oscillate as for the low value of γ_{12}. It does however become negative, but apparently not enough to influence the envelope in a significant way. This is also apparent from figure 7.11(c) showing that the phase stays at zero. As in figure 7.10(c) you should disregard the data indicating a phase of π as these are numerical artifacts.

This behavior can be explained when interpreting γ_{12} as a linewidth, contributing to the width of the two split $|2\rangle$ levels. As γ_{12} becomes much larger than the separation between them, $\approx 2|\Omega_c|$, the distinct two level nature will be washed out and they will effectively behave as a single wide level. This explains why the QD material appears to has gone normal, much like the situation depicted in figure 6.1(c).

7.6. Two pulse analysis

In the last section we examined how single pulses behaved. Hence we are in a better position to interpret and predict how several pulses will behave. The question of how several pulses will interact in a slow-light device is of great practical interest. These might become important components in future optical systems. Our analysis will however still suffer from the fact that γ_{13} has been set to an unrealistically low value.

From the previous section we can draw some important conclusions on how to obtain well behaving pulses, ie. pulses not getting destroyed by dipole oscillations or damped too much. First of all, in order for the split $|2\rangle$ levels to be distinct, the linewidth γ_{12} must be much smaller than the splitting, $2|\Omega_c|$, itself. We can state the requirement: $\gamma_{12} \ll 2|\Omega_c|$. This is a property of the QDs and hence not very easy to control. Secondly, we observed that if the pulse had a spectral width, W_ω, of the order or larger than the splitting, $\mathrm{Im}[\sigma_{12}]$ began to oscillate and this destroyed the pulse. Hence another requirement is that W_ω must be much smaller than the splitting: $W_\omega \ll 2|\Omega_c|$. This is a property which to some degree is controllable, but limited by the bandwidth of the signal.

Both these requirements limit how low the Rabi frequency of the coupling field can be. From figure 6.3 we see the general trend that increasing $|\Omega_c|$ will decrease the group index and thereby the amount one can slow down light. In a optical network a group index of several thousands will typically be needed [4] and as we set a lower limit for n_g, we could get into trouble with the fulfillment of the two requirements, $\gamma_{12} \ll 2|\Omega_c|$ and $W_\omega \ll 2|\Omega_c|$.

In the following we will present a few examples to show some effects, that occur when more than one pulse is present.

We start out by considering a simulation of two narrow pulses of spectral width $W_\omega = 1358$ GHz, $W_\omega > 2|\Omega_c|$, and with a top-to-top distance of 0.67 mm. The solution is shown in figure 7.12(a). As expected the pulse does not behave well, the large dipole oscillations destroy both pulses and nothing useful is transmitted through region II.

Figure 7.12(b) shows two wide pulses of spectral width $W_\omega = 274.7$ GHz, and hence $W_\omega < 2|\Omega_c|$, separated by a top-to-top distance of 2.40 mm. The plot is cross sections at 7 equidistant times as this illustrates the point better. Here we expect the pulses to behave nicely as their spectral width is smaller than the level splitting, and so they do. After transmission through region II, one can easily distinguish the top of each pulse, which is necessary for them to be able to represent binary data.

Decreasing the separation between the pulses corresponds to increasing the network bandwidth, which is of great interest in the industry. In figure 7.12(c) we have decreased the separation between the pulses to 1.76 mm. The effect is that you are not able to clearly distinguish the two peaks, as there is no longer anything really separating them. An electronic device that would

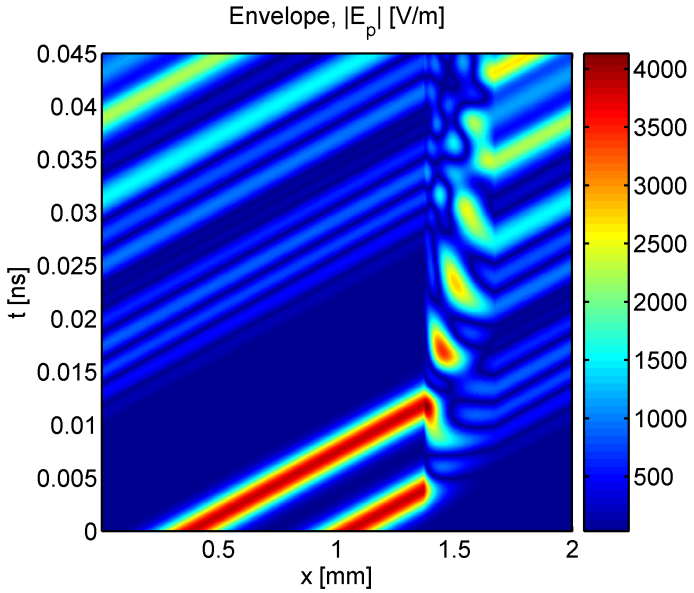

(a) Two narrow pulses of $W_x = 0.17$ mm and $W_\omega = 1358$ GHz, separated by a distance $\Delta x = 0.67$ mm.

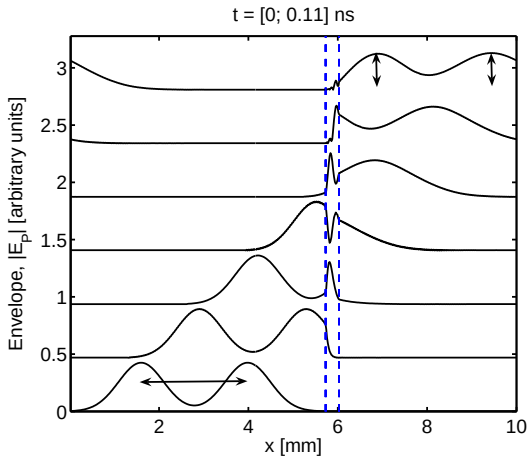

(b) Two wide pulses of $W_x = 0.84$ mm and $W_\omega = 274.7$ GHz, separated by a distance $\Delta x = 2.40$ mm.

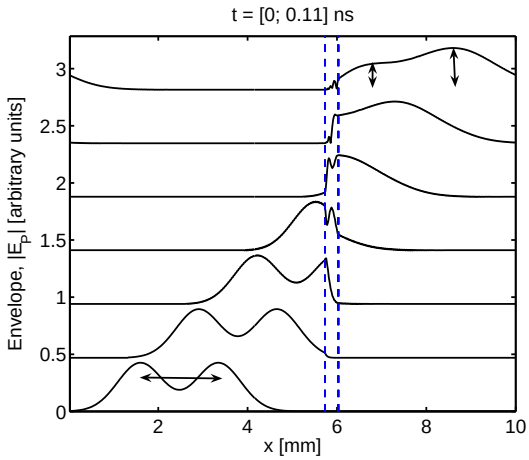

(c) Two wide pulses of $W_x = 0.84$ mm and $W_\omega = 274.7$ GHz, separated by a distance $\Delta x = 1.76$ mm.

Figure 7.12.: *Solutions of different two-pulse situations.*

have to decide what binary sequence these represents, would have a problem. This mixing of the two pulses is caused by the dipole oscillations the first pulse induces, as it enters region II. The dipole oscillations are not as powerful as those induced by the pulse in figure 7.12(a), and they do not destroy the pulse itself. As the first pulse has passed through a section in region II, it leaves behind oscillating dipoles. These of course decay according to γ_{12}, but if the second hits region II before they have vanished, it will interact with the dipoles. Exactly what happens to the second pulse depends on whether it hits a *hill* or *valley* in the oscillating $\mathrm{Im}[\sigma_{12}]$. This gives rise to many peculiar and interesting phenomena.

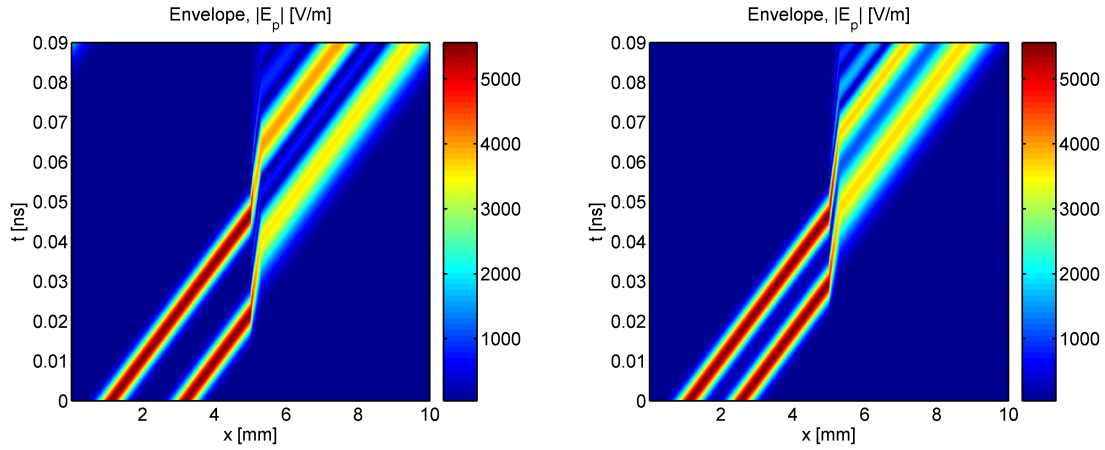

(a) Separation of 2.08 mm.

(b) Separation of 1.43 mm.

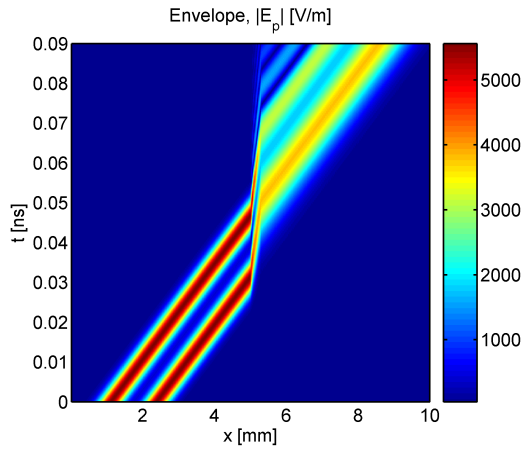

(c) Separation of 1.27 mm.

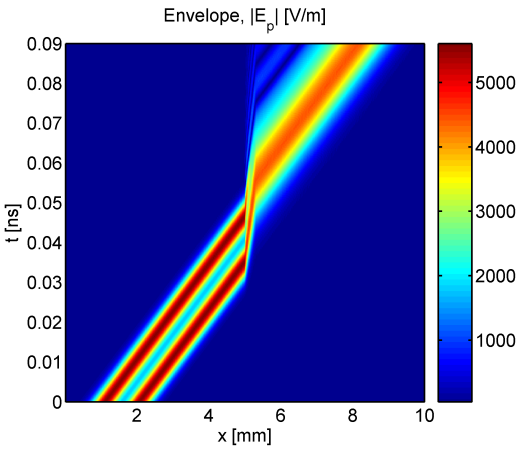

(d) Separation of 0.95 mm.

Figure 7.13.: *Illustrations of how decreasing the separation between two pulses will eventually destroy them due to dipole oscillations. The separation in the first plot corresponds to a 40Gbs signal and a 88Gbs in the last plot. The pulse width* 5 ps *for all simulations,* $\Omega_c = 650$ GHz, *and* $\gamma_{12} = 50$ GHz.

As a last example we have selected a temporal pulse width of 5 ps suitable of a 40Gbs signal (corresponds to a separation of 25 ps). We will examine how the two pulses interact when we decrease the separation between them and hence obtain a minimum of this distance. This is close to what have been done above, but these pulses do not fulfill the $W_\omega \ll 2|\Omega_c|$-requirement as well as above. A Rabi frequency of $|\Omega_c| = 650$ GHz has been selected, to avoid too powerful dipole oscillations. This means, on the down side, that we can only achieve a group index of around 15.

A quantity as the extinction ratio[10] could be expected to provide a nice number for this kind of test. This turns out not to be the case for these simulations. The dipole oscillations create small fields in between the two pulses and make it difficult to have a well defined extinction ratio. Instead we will shortly describe what is seen and what can be concluded.

In figure 7.13(a) the two pulses are well transmitted through region II. This is also the case for the simulation in figure 7.13(b), where the separation has been decreased from 2.08 mm to 1.43 mm. The situation is slightly worse in figure 7.13(c), where we have further decreased the separation now to 1.27 mm. The second pulse is now clearly influenced by the dipole oscillations induced by the first. Figure 7.13(d) shows a separation of 0.95 mm, where the second pulse is completely destroyed and somehow mixes up with the first.

This example illustrates that a separation of 1.43 mm the two pulses will not mix noticeably, and the bandwidth would go from 40Gbs to almost 60Gbs. Moving the pulse closer together will, if maintaining fixed pulse width, of course make the binary data they represent less distinct. This issue is related to the detection equipment converting the optical signals back to electrical form and is not considered in this report. We observed that if one move two pulses too close to each other, they will interact and can not be distinguished in region III. This sets a limit on the bandwidth, which can only be removed by further increasing $|\Omega_c|$ and hence a further reduction of the group index.

[10] Sometimes defined as: $r_e = 10 \log_{10} \frac{P_2}{P_1}$, where P_2 and P_1 are the powers of a peak and a valley in a signal.

8. Outlook

After finishing these analyses there are of course interesting subjects which have not been examined. Most of these are related to how our system performs under conditions used in future real life applications. That is, it could be interesting to perform a deeper and more systematic analysis of how several pulses interact. Thereby, obtain a better understanding of the limitations of the bandwidth and refractive group index on physical grounds. Simpler analyses of this sort have been performed by different groups for general slow down materials, with considerations similar to the ones in the steady state chapter [2, 16], but with different conclusions. They do not, however, include the dynamic coupling and misses some of the limitations it imposes.

As mentioned the dipole oscillations induced by spectrally wide pulses, give rise to many interesting effects. Some of these we have been able understand as a beat phenomena. A more thorough analysis could hopefully lead to a better physical understanding of these phenomena. There are lots of parameter sets we have not examined and one could hope for exciting new effects lurking somewhere in the parameter wilderness.

In the last chapter we have performed dynamic simulations, but are limited to low group indexes (~ 50) and small spacing between two pulses, compared to the material width. These limitations are mostly due to the periodic boundary conditions and the fact that we can only initiate the pulses in the space domain, as $E(x,0) = f(x)$. If we could initiate them in time, $E(t,0) = f(t)$, we could simulate many wide pulses and make the material extend to most of the domain and thus cope with large slowdown factors without using a lot of points.

One way to overrule the periodic boundary conditions is to enforce a strong damping at the right boundary [15]. Every pulse approaching it would be absorbed and only solutions of zero value would be reenter at the left boundary. It is however very difficult to implement the boundary condition in time. This we tried, but the spectral method does not handle these boundary conditions in time very well, as they are discontinuous at the left boundary.

In our model the coupling field is assumed to be constant, as it is much stronger than the probe field. When this is the case our model provides a good description. In situations in which we turn the coupling field on and off fast, this is not a sufficient description. To analyze this, the model should be extended to include a dynamic coupling field from which we would get two new wave equations.

9. Conclusion

In the following we will summarize the results obtained in this project.

We have calculated the transition matrix elements for the interband transition $|1\rangle \leftrightarrow |2\rangle$, and intraband transition $|2\rangle \leftrightarrow |3\rangle$ in a rotational symmetric quantum dot on a wetting layer. The calculated values are of the order a few nanometers, in units of the elementary charge, and are in agreement with previously published results by Chang-Hasnain *et al.* [1, 4].

A space dependent version of the optical Bloch equations has been derived and applied to the three-level system in the quantum dot, with an electric field interaction.

An analysis of slow-light has been performed for the case both the probe and coupling field being continuous wave fields. Here analytical results are obtained for the complex susceptibility and refractive group index. From this we predict slow down factors ranging from the background value to a staggering 10^6 and an accompanying absorption which unfortunately increases along with the group index. Again in accordance with Chang-Hasnain *et al.*

The analysis has been extended to a model for simulation of the dynamic behavior of pulses. In this we adopt the slowly varying envelope approximation for equation of the electric field. A numerical implementation based on a combined Runge Kutta/spectral method has been developed.

With this we have simulated EIT for a wide range of different pulses. From this it is evident that the linewidth γ_{13} introduces a large absorption when set to realistic values. This poses a significant problem for the use of quantum dots for EIT.

For wide pulses the predictions of the steady state and dynamical analyses are in good agreement. For narrow pulses, spectrally exceeding the level splitting, the dynamical model predicts large dipole oscillations. In some cases these can destroy the pulse itself. Furthermore the linewidth γ_{12} has to be relatively low for the two split levels to remain distinct.

In order for two pulses to be adequately transmitted through the active region we can state the following requirements: $\gamma_{12} \ll 2|\Omega_c|$ and $W_\omega \ll 2|\Omega_c|$. However, if the separation between two pulses becomes too small, fulfilling the above requirements is not enough for them to be transmitted nicely. Dipole oscillations, although small, will in worst case destroy the second pulse.

The parameters γ_{12} and W_ω set the lower limit for Ω_c. The bandwidth of the signal will provide W_ω and γ_{12} is given by the material. The lower limit of Ω_c implies that only a certain (low) n_g can be obtained, which is a serious draw-back for applications.

Henri Nielsen

Per Nielsen

Bibliography

[1] Connie J. Chang-Hasnain, Pei-Cheng Ku, Jungho Kim, and Shun-Lien Chuang. Variable optical buffer using slow light in semiconductor nanostructures. *Proceedings of the IEEE*, 91 (11):1884–1897, November 2003.

[2] R. S. Tucker, P. C. Ku, and C. J. Chang-Hasnain. Delay-bandwidth product and storage density in slow light optical buffer. *electronics Letters*, 41(4), February 2005.

[3] Zachary Dutton, Naomi S. Ginsberg, Christopher Slowe, and Lene Vestergaard Hau. The art of taming light: ultra-slow and stopped light. *europhysics news*, March/April 2004.

[4] J. Kim, S. L. Chuang, P. C. Ku, and C. J. Chang-Hasnain. Slow light using semiconductor quantum dots. *Journal of Physics: Condensed Matter*, pages 3727–3735, August 2004.

[5] Stephen E. Harris. Electromagnetically induced transparency. *Physics Today*, July 1997.

[6] Marlan O. Scully and Suhail Zubairy. *Quantum Optics*. Cambridge University Press, 1997. ISBN 0521435951.

[7] J.M. Luttinger and W. Kohn. Motion of electrons and holes in perturbed periodic fields. *Physical Review*, pages 869–883, February 1955.

[8] L.A. Coldren and S.W. Corzine. *Diode Lasers and Photonic Integrated Circuits*. Wiley, 1995. ISBN 0471118753.

[9] Trols Markussen, Philip Kristensen, Bjarne Tromborg, Tommy Winther Berg, and Jesper Mørk. Influence of wetting layer wave functions on phonon meditated carrier capture into self-assembled quantum dots. February 2005.

[10] Rodney Loudon. *The Quantum Theory of Light*. Oxford Science Publications, 2000. ISBN 0198501765.

[11] P. Borri, W. Langbein, S. Schneider, U. Woggon, R.L. Sellin, D. Ouyang, and D. Bimberg. Ultralong dephasing time in ingaas quantum dots. *Physical Review Letters*, 87(15):157401–1 – 157401–4, October 2001.

[12] P. Borri, W. Langbein, J. Mørk, J.M. Hvam, F. Heinrichsdorff, M.-H. Mao, and D. Bimberg. Dephasing in inas/gaas quantum dots. *Physical Review B*, 11(60):7784–7787, September 1999.

[13] Ammon Yariv. *Quantum Electronics*, chapter 15. John Wiley & Sons, Inc., 2nd edition, 1975.

[14] Lloyd N. Trefethen. *Spectral Methods in MATLAB*. Society of Industrial and Applied Mathematics, 2000.

[15] John P. Boyd. *Chebyshev and Fourier Spectral Methods*. Dover Publishers, 2nd edition, 2001.

[16] Robert W. Boyd, Daniel J. Gauthier, Alexander L. Gaeta, and Alan E. Willner. Maximum time delay achievable on propagation through a slow-light medium. *Physical Review A*, 71, 2004.

[17] Henrik Bruus. Introduction to nanotechnology. Lectrue note, 2004.

[18] Z. M. Zang and Keunhan Park. On the group front and group velocity in a dispersive medium upon refraction from a nondispersive medium. *Journal of Heat Transfer*, Spring .

A. Appendix

A.1. EIT window in $\tilde{\chi}$

We want to obtain approximate expressions for the frequency ranges $\Delta\chi'$ and $\Delta\chi''$ shown in figure 6.4. In the expressions for χ' and χ'' (eq. (6.6) and (6.7) respectively) we put $\gamma_{13} = 0$ as our main assumption is that: $\gamma_{13} \ll \gamma_{12}, \Omega_c$. Performing this substitution, setting $\Delta_c = 0$ which we are free to do, χ' and χ'' reduce to

$$\chi' = \frac{N|\mu_{21}|^2\eta}{\varepsilon_0\hbar}\frac{\Delta_p(\Delta_p^2 - |\Omega_c|^2)}{\left[|\Omega_c|^2 - \Delta_p^2\right]^2 + \left[\Delta_p\gamma_{12}\right]^2},$$

and

$$\chi'' = \frac{N|\mu_{21}|^2\eta}{\varepsilon_0\hbar}\frac{\Delta_p^2\gamma_{12}}{\left[|\Omega_c|^2 - \Delta_p^2\right]^2 + \left[\Delta_p\gamma_{12}\right]^2}.$$

As seen from figure 6.4 $\Delta\chi'$ and $\Delta\chi''$ are the distances between two extremum, having zero slope. This invites us to differentiate χ' and χ'' with respect to Δ_p and equate with zero,

$$\frac{\partial\chi'}{\partial\Delta_p} = 0 \Rightarrow \Delta_p^4 - \Delta_p^2\gamma_{12}^2 - 2\Delta_p^2|\Omega_c|^2 + |\Omega_c|^4 = 0$$

and

$$\frac{\partial\chi''}{\partial\Delta_p} = 0 \Rightarrow |\Omega_c|^4 - \Delta_p^4 = 0.$$

Solving the equations for χ' gives four solutions as you could have guessed (χ' has four extremum), picking the lowest positive and multiplying by two as we want the full width, gives following result

$$\frac{\Delta\chi'}{|\Omega_c|} = \sqrt{\frac{\gamma_{12}}{|\Omega_c|} + 4} - \frac{\gamma_{12}}{|\Omega_c|}.$$

The equation for χ'' is easily solved and after multiplying by two we get

$$\frac{\Delta\chi''}{|\Omega_c|} = 2.$$

These are the desired results.

A.2. Approximative vs. exact susceptibility

The purpose of this appendix is to justify the assumption made in section 6.2, by comparing the approximate solution with the exact solution of the susceptibility. For the case of both the probe and coupling field being CW fields, the Bloch equations are a set of linear first order differential equations. These we are able to solve by using methods from linear algebra, even in the full time-dependent case. However, we are only interested in the steady state solutions. Setting all time derivatives equal to zero reduces the Bloch equations to a set of ordinary linear equations. Along with conservation of probability restriction: $\rho_{11} + \rho_{22} + \rho_{33} = 1$, these are easily solved analytically using MATHEMATICA. The solutions are very extensive, so we will not present them here, but merely show the susceptibility resulting from them.

The assumptions imposed in section 6.2 were the following: First we assumed that all carriers were trapped in the ground state, $\eta = \rho_{11} - \rho_{22} \approx 1$, i.e. full EIT state. Secondly we assumed that $\Omega_c \gg \Omega_p$, which basically means that $|\tilde{E}_c| \gg |\tilde{E}_p|$. The second assumption is the only one which we can control directly and it turns out that $\eta \approx 1$ follows from this, see figure A.4.

Apart from making the solutions simpler, another effect was that the decay rates γ_{22}, γ_{33} and γ_{23} and Ω_p drop out of the solutions. Hence the susceptibility does not depend on these parameters in the approximation. When solving without any approximations, we cannot expect this to happen and it does not. To graphically compare the two different susceptibilities, we of course have assign values to γ_{22}, γ_{33}, γ_{23} and Ω_p.

First we want to illustrate how gradually increasing the ratio $\lambda = \frac{|\Omega_c|}{|\Omega_p|}$, will make the approximative and exact solution converge towards the same. We fix the decay rates for the off-diagonal elements so that: $\gamma_{12} = \gamma_{13} = \gamma_{23} = 5 \times 10^9$ Hz. The decay rates for diagonal elements we set a bit lower since these do not experience dephasing: $\gamma_{22} = \gamma_{33} = 10^9$ Hz. The Rabi frequency for the coupling field is fixed at 50 GHz. This means that when we increase λ we decrease $|\Omega_p|$. All other parameters are as in table 6.2. The figures A.1(a) to A.1(e) show how increasing λ from 5 to 230 in different steps, make the two solutions tend towards the same susceptibility. The approximate solution does not change while varying λ, as it does depend on the probe field amplitude. The ratio $\lambda = 230$ corresponds to $\frac{|\tilde{E}_c|}{|\tilde{E}_p|} \approx 51$.

Having found a λ where the two solutions seem to coincide with each other, we now fix λ to 230 and vary the decay rates. In figure A.2(a) we have used $\gamma_{23} = 5 \times 10^9$ Hz and $\gamma_{22} = \gamma_{33} = 1 \times 10^{12}$ Hz, a shift of three orders of magnitude in the diagonal decay rates. Remarkably, no change is apparent from the figure illustrating the two solutions. Figure A.2(b) shows the case where $\gamma_{23} = 5 \times 10^{12}$ Hz and $\gamma_{22} = \gamma_{33} = 1 \times 10^9$ Hz, here the off-diagonal decay rate has been raised three orders of magnitude. Again we see no difference between the two solutions. Finally in figure A.2(c) both set of decay rates have been set to high values: $\gamma_{23} = 5 \times 10^{12}$ Hz and $\gamma_{22} = \gamma_{33} = 1 \times 10^{12}$ Hz. This does not cause any visible difference either.

The conclusion to be drawn from this appendix is illustrated in figures A.1 and A.2. If the assumption $\Omega_c \gg \Omega_p$ is sufficiently well satisfied, the values of γ_{23}, γ_{22} and γ_{33} do not seem to matter much.

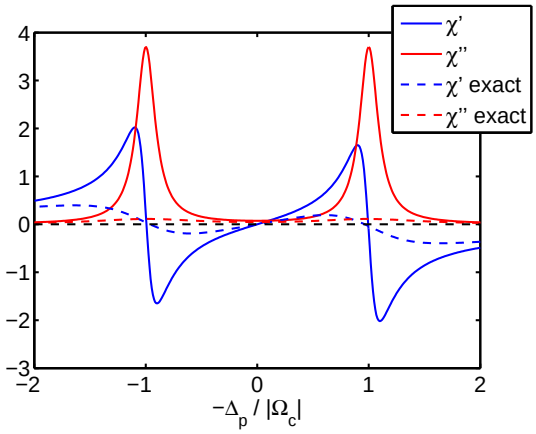

(a) $\lambda = 5$.

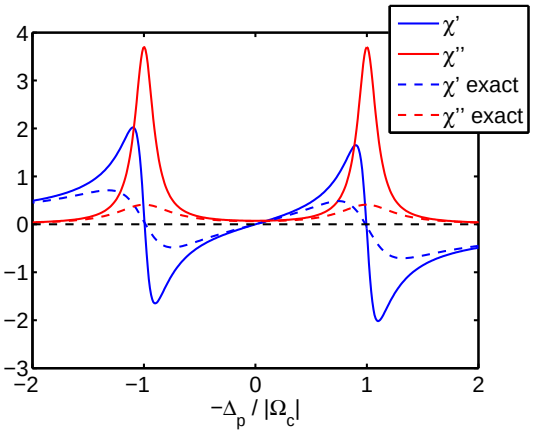

(b) $\lambda = 10$.

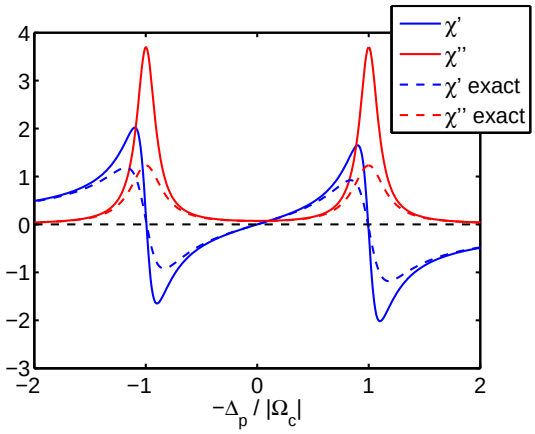

(c) $\lambda = 20$.

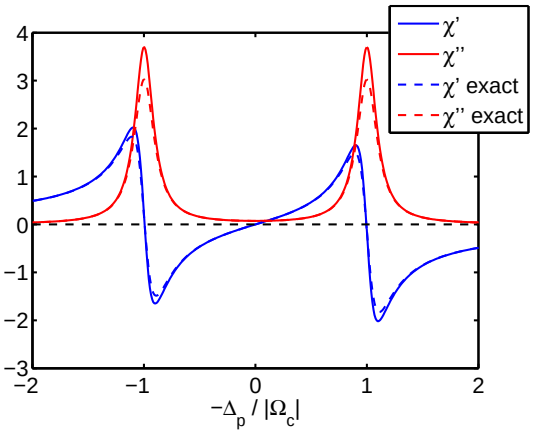

(d) $\lambda = 60$.

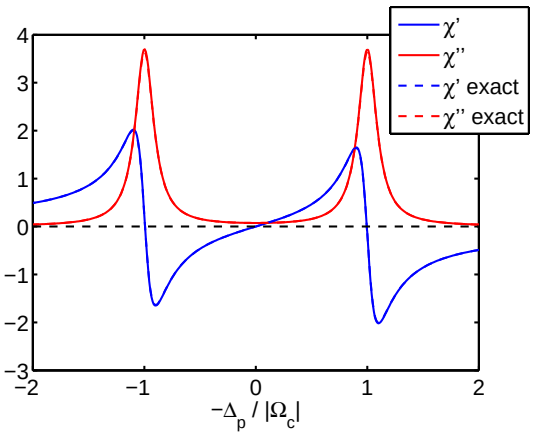

(e) $\lambda = 230$.

Figure A.1.: *Figures for of the comparison approximate and exact solution of the susceptibility. The ratio* $\lambda = \frac{|\Omega_c|}{|\Omega_p|}$ *is increased from 5 to 230 and all other parameters are fixed.*

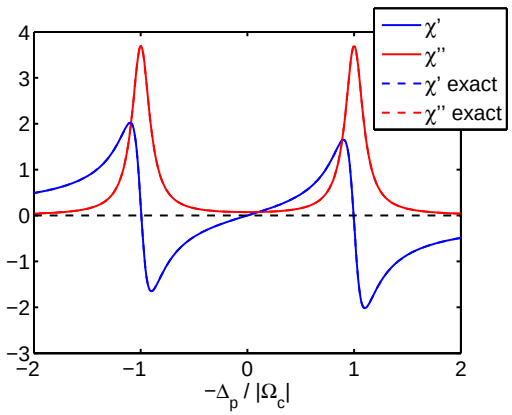

(a) $\gamma_{23} = 5 \times 10^9$ Hz and $\gamma_{22} = \gamma_{33} = 1 \times 10^{12}$ Hz.

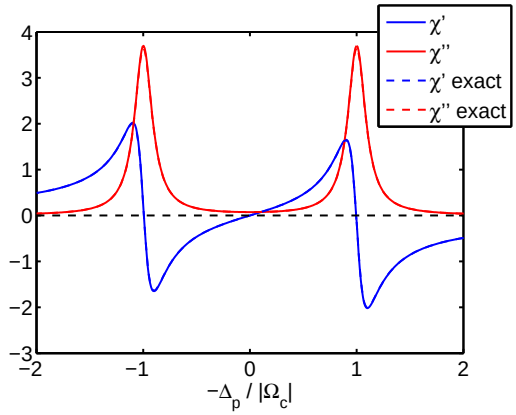

(b) $\gamma_{23} = 5 \times 10^{12}$ Hz and $\gamma_{22} = \gamma_{33} = 1 \times 10^9$ Hz.

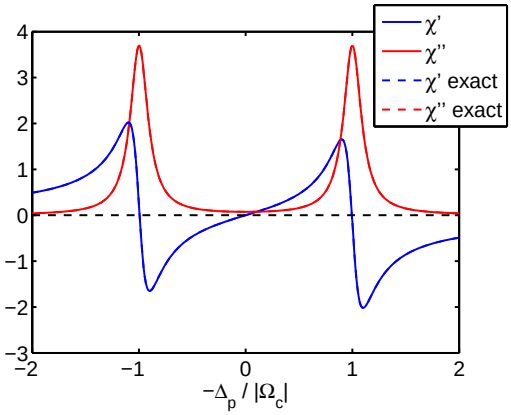

(c) $\gamma_{23} = 5 \times 10^{12}$ Hz and $\gamma_{22} = \gamma_{33} = 1 \times 10^{12}$ Hz.

Figure A.2.: *Figures for comparison of the approximate and exact solution of the susceptibility. Here we fixed* $\lambda = 230$ *and* $|\Omega_c| = 50$ *GHz, while the decay rates are changed.*

A.3. Selection rules and $|M|$

In the first part of this appendix we want to show that the interband transitions $(v, 1, \pm 1) \leftrightarrow (c, 1, 0)$ and the intraband transition $(c, 1, 0) \leftrightarrow (c, 2, 0)$ are non-allowed dipole transitions.

For the interband transition $(v, 1, \pm 1) \leftrightarrow (c, 1, 0)$ we know from eq. (3.8) that it is the overlap integral, between the two envelope functions, that determines whether or not the transition is dipole allowed. We use the basis (3.11) to represent the degenerate subspace, thus we have

$$\langle F^v_{1\pm1} | F^c_{10} \rangle = \left\langle f^v_{11} \Phi^{\pm} \middle| \frac{1}{\sqrt{2\pi}} f^c_{10} \right\rangle = \frac{1}{\sqrt{2\pi}} \int \Phi^{\pm} d\varphi \int [f^v_{11}]^* \, f^c_{10} r dr dz.$$

The integral over $\Phi^{\pm}$ will be either over a pure cosine or sine, both equal to zero and the transition is not dipole allowed.

The matrix element for the intraband transition $(c, 1, 0) \leftrightarrow (c, 2, 0)$ is given by, cf. eq. (3.12):

$$\langle F^c_{10} | r \sin\varphi | F^c_{20} \rangle = \frac{1}{2\pi} \int \sin\varphi d\varphi \int [f^c_{10}]^* \, f^c_{20} r^2 dr dz,$$

the integral over the sine function will equal zero and hence the transition is not dipole allowed.

In the last part we explain how we arrived at eq. (3.9), $|M| = \frac{0.699}{(\omega_{\mathrm{p}}[\mathrm{fs}^{-1}])}$ nm. The matrix element, absolute squared, for the interband transitions considered in this report, can be written in the following form:

$$|\langle 1|\hat{H}_{\mathrm{I}}|2\rangle|^2 = |eE_0|^2|\langle u^v|\hat{\mathbf{e}}\cdot\mathbf{r}|u^c\rangle|^2|\langle F^v_{10}|F^c_{10}\rangle|^2,$$

where $\hat{\mathbf{e}}$ is a unit vector in the direction of the polarization of the field and E_0 is a field amplitude. In the notation of the magnetic vector potential, $\mathbf{A}$, and the momentum operator, $\hat{\mathbf{p}}$, the same matrix elements can be written

$$|\langle 1|\hat{H}_{\mathrm{I}}|2\rangle|^2 = |eA_0/2m|^2|\langle u^v|\hat{\mathbf{e}}\cdot\hat{\mathbf{p}}|u^c\rangle|^2|\langle F^v_{10}|F^c_{10}\rangle|^2,$$

where A_0 is the amplitude of the vector potential. Equating these two expressions and cancelling common factors yields

$$|E_0|^2|\langle u^v|\hat{\mathbf{e}}\cdot\mathbf{r}|u^c\rangle|^2 = |A_0/2m|^2|\langle u^v|\hat{\mathbf{e}}\cdot\hat{\mathbf{p}}|u^c\rangle|^2.$$

The relation between E_0 and A_0 can be found from $\mathbf{E} = -\frac{\partial\mathbf{A}}{\partial t}$, and for a CW field this implies that $A_0 = \frac{E_0}{\omega_0}$. Using this and rearranging we get

$$|\langle u^v|\hat{\mathbf{e}}\cdot\mathbf{r}|u^c\rangle|^2 = \frac{1}{8m\omega_0^2}\frac{2}{m}|\langle u^v|\hat{\mathbf{e}}\cdot\hat{\mathbf{p}}|u^c\rangle|^2 \equiv \frac{1}{8m\omega_0^2}\beta.$$

The β parameter can be found in [8, p. 121] and for InAs it has the value 22.2 eV. Inserting this, the electron mass, and taking the square root gives the following result,

$$|M| = \frac{0.699}{(\omega_{\mathrm{p}}[\mathrm{fs}^{-1}])}\ \mathrm{nm},$$

where we have replaced ω_0 by ω_{p}, which has to be plugged in in units of fs^{-1}. This is the expression we were looking for.

A.4. Real/Fourier space width product

In this appendix we will derive the relation $W_xW_k = W_tW_\omega = 4\ln 2$, eq. (7.7). The initial condition, eq. (7.6), for the Gaussian pulse we use in the simulations is ($x_0 = 0$)

$$E'_{\mathrm{p}}(x) = \mathcal{E}_{\mathrm{p}}\exp\left[-2\ln 2\left(\frac{x}{W_x}\right)^2\right].$$

The FWHM for this pulse is by construction equal to W_x. The pulse above has a Fourier transform given by

$$E'_{\mathrm{p}}(k) = \int_{-\infty}^{+\infty} E'_{\mathrm{p}}(x)e^{ikx}dx = \mathcal{E}_{\mathrm{p}}W_x\sqrt{\frac{\pi}{2\ln 2}}\exp\left(-\frac{k^2W_x^2}{8\ln 2}\right),$$

the Fourier transform is seen also to be a Gaussian peaked about $k = 0$. The FWHM if the Fourier transform can be found from the equation $|E_{\mathrm{p}}^{'}(W_k/2)|^2 = \frac{1}{2}|E_{\mathrm{p}}^{'}(0)|^2$. Solving this with respect to W_k yields: $W_k = \frac{1}{W_x} 4 \ln 2$. Multiplying W_x and W_k gives the wanted result

$$W_x W_k = 4 \ln 2.$$

One can repeat the above for time and frequency and find the same product.

A.5. Derivation of the wave equation

We want to derive the wave equation governing electric waves in matter. This is done from the four Maxwell equations which are the basic equations of classical electromagnetic theory. We start out by the Maxwell equations in matter.

$$\nabla \cdot \mathbf{D} = 0 \tag{A.1a}$$

$$\nabla \times \mathbf{E} = -\frac{\partial \mathbf{B}}{\partial t} \tag{A.1b}$$

$$\nabla \cdot \mathbf{B} = 0 \tag{A.1c}$$

$$\nabla \times \mathbf{H} = \frac{\partial \mathbf{D}}{\partial t}. \tag{A.1d}$$

Where $\mathbf{D}$ and $\mathbf{H}$ in general are given as

$$\mathbf{D} = \varepsilon_0 \mathbf{E} + \mathbf{P}_{\mathrm{b}} + \mathbf{P} = \varepsilon \mathbf{E} + \mathbf{P} \tag{A.2a}$$

$$\mathbf{H} = \frac{1}{\mu_0} \mathbf{B} - \mathbf{M}. \tag{A.2b}$$

In eq. (A.2a) for $\mathbf{D}$, we have split the polarization into two parts. A linear background polarization, $\varepsilon \mathbf{E}$, in which we can include the dielectric constant, $\varepsilon = \varepsilon_0 \varepsilon_{\mathrm{b}}$. $\mathbf{P}$ is the actively induced polarization which can be time and space dependent. To simplify the calculation we assume that the material does not have a magnetization, and $\mathbf{M}$ can be eliminated. To arrive at the wave equation for $\mathbf{E}$ we need two of the four Maxwell equations.

First we insert the expressions for $\mathbf{H}$ and $\mathbf{D}$ into eq. (A.1d) and get

$$\frac{1}{\mu_0} \nabla \times \mathbf{B} = \varepsilon \frac{\partial \mathbf{E}}{\partial t} + \frac{\partial \mathbf{P}}{\partial t}.$$

Taking the curl of (A.1b) and inserting the equation above we arrive at the three dimensional wave equations:

$$\begin{aligned} \nabla \times (\nabla \times \mathbf{E}) &= -\frac{\partial}{\partial t} (\nabla \times \mathbf{B}) \\ &= -\mu_0 \varepsilon \frac{\partial^2}{\partial t^2} \mathbf{E} - \mu_0 \frac{\partial^2}{\partial t^2} \mathbf{P}. \end{aligned}$$

Using that $\mu_0 \varepsilon_0 = c^{-2}$ and defining $n_{\mathrm{b}} \equiv \sqrt{\varepsilon_{\mathrm{b}}}$, called the background refractive index, the wave equation can be written as,

$$\nabla \times (\nabla \times \mathbf{E}) + \frac{n_{\mathrm{b}}^2}{c^2} \frac{\partial^2}{\partial t^2} \mathbf{E} = -\mu_0 \frac{\partial^2}{\partial t^2} \mathbf{P}.$$

By using the relation $\nabla\times(\nabla\times\mathbf{E}) = \nabla(\nabla\cdot\mathbf{E})-\nabla^2\mathbf{E}$ we can rewrite the equation to give,

$$\nabla^2\mathbf{E} - \nabla(\nabla\cdot\mathbf{E}) - \frac{n_\mathrm{b}^2}{c^2}\frac{\partial^2}{\partial t^2}\mathbf{E} = \mu_0\frac{\partial^2}{\partial t^2}\mathbf{P}. \tag{A.3}$$

A solution to eq. (A.3) is transverse EM waves in which the electric field is orthogonal to the propagation direction. We can effectively reduce the problem to 1D by choosing $\mathbf{E} = E(x)\hat{\mathbf{y}}$. The second term now equals 0 as $\nabla(\nabla\cdot E(x)\hat{\mathbf{y}}) = \nabla(\frac{\partial E(x)}{\partial y}) = 0$ and eq. (A.3) reduces to

$$\frac{\partial^2}{\partial x^2}E - \frac{n_\mathrm{b}^2}{c^2}\frac{\partial^2}{\partial t^2}E = \mu_0\frac{\partial^2}{\partial t^2}P.$$

A.6. Group velocity

In this appendix we want to give a short derivation of the group velocity used in eq. (4.6) and some outlook to its definition and limitations. The derivation here is greatly inspired by [17]

If we in 1D consider a wave package, we can define the group velocity as the velocity of its maximum amplitude. A wave package can be composed by superimposing plane waves with different wave vectors peeked around k_0. The amplitude of each wave is given by $\Phi(k)$. To form a well behaved wave packed we require that $\Phi(k)$ goes to zero for large $|k|$ values. The wave packet in time and space, $\tilde{F}(x,t)$ can then be written as a Fourier transform,

$$\tilde{F}(x,t) = \int_{-\infty}^{\infty} dk e^{i(kx-\omega_k t)}\Phi(k). \tag{A.4}$$

We assume that the wave packet is confined to a narrow region around k_0 and thus we can Taylor expand the dispersion relation, ω_k around k_0 to first order.

$$\omega_k \approx \omega_0 + \frac{\partial\omega_0}{\partial k}(k-k_0) + \mathcal{O}((k-k_0)^2)$$

where $\omega_k = \omega(k)$ and $\omega_0 = \omega(k_0)$. This inserted into eq. (A.4) and defining $K = k - k_0$ yields,

$$\begin{aligned}\tilde{F}(x,t) &\approx \int_{-\infty}^{\infty} dK e^{i[(K+k_0)x-(\omega_0+\frac{\partial\omega_0}{\partial k}K)t]}\Phi(K+k_0)\\ &= e^{i(k_0x-\omega_0t)}\int_{-\infty}^{\infty} dK e^{i(x-\frac{\partial\omega_0}{\partial k}t)K}\Phi(K+k_0)\end{aligned}$$

The complex exponential is just the fast oscillation of the center frequency and just the normal phase velocity $v_\mathrm{ph} = \frac{\omega_0}{k_0}$. The integral is a function with a argument of the form: $x-\frac{\partial\omega}{\partial k}t$. This implies that a function value of constant argument, will move with a velocity

$$v_\mathrm{g} = \frac{\partial\omega}{\partial k}$$

Which is the group velocity.

It can be proved that the group velocity and energy velocity are equal for propagating electromagnetic waves in linear, nondissipative and nonmagnetic media [18]. This is not in general the

case in our study. For absorbing and dispersive media the group velocity can be both larger than the speed of light or negative. This is due to changes of the pulse shape and the peak point no longer represents the flow of energy and the group velocity is no longer a good definition.

A.7. The slowly varying envelope approximation applied to the wave equation

The derivation of the two envelope equations from the wave equation is a rather lengthy affair. In this appendix we will go into some more detail with this calculation.

We want to solve the wave equation

$$\frac{\partial^2}{\partial x^2}E - \frac{n_\mathrm{b}^2}{c^2}\frac{\partial^2}{\partial t^2}E = \mu_0\frac{\partial^2}{\partial t^2}P, \qquad \text{eq. (4.1)}$$

and write the electric field and the polarization as envelope functions times an underlying fast oscillation

$$E = E'_\mathrm{p}\cos(k_\mathrm{p}x - \omega_\mathrm{p}t) - E''_\mathrm{p}\sin(k_\mathrm{p}x - \omega_\mathrm{p}t) + \mathcal{E}_\mathrm{c}\cos(k_\mathrm{c}x - \omega_\mathrm{c}t), \qquad \text{eq. (7.2)}$$

$$P = U_\mathrm{p}\cos(k_\mathrm{p}x - \omega_\mathrm{p}t) - V_\mathrm{p}\sin(k_\mathrm{p}x - \omega_\mathrm{p}t) + \mathcal{U}_\mathrm{c}\cos(k_\mathrm{c}y - \omega_\mathrm{c}t) - \mathcal{V}_\mathrm{c}\sin(k_\mathrm{c}y - \omega_\mathrm{c}t). \qquad \text{eq. (7.3)}$$

All the curled parameters is assumed to be known and constants. This rewriting can be done in general when we have two functions for each field, but is most practical when the chosen frequency is a resonant frequency of the system. If this is fulfilled we can in most cases assume that the envelope functions are slowly varying compared to the underlying resonant frequencies. For optical systems this criteria is easily met as $\omega_\mathrm{c}, \omega_\mathrm{p} \approx 10^{15}\ \mathrm{s}^{-1}$, which is only violated when considering femtosecond wide envelopes.

We now want to find equations for E'_p and E''_p, which ensure that the electric field is satisfying the wave equation. Inserting (7.2) and eq. (7.3) into (4.1) yields a lengthy nonlinear differential equation.

To simplify this, we apply the slowly varying envelope approximation which in mathematical terms can stated as: $\partial F/\partial t \ll \omega F, \partial F/\partial x \ll kF, \partial^2 F/\partial t^2 \ll \omega \partial F/\partial t, \partial^2 F/\partial x^2 \ll k\partial F/\partial x$, where F represent the four envelope functions, E'_p, E''_p, U_p and V_p. In practice we end up removing all non-linear and 2. order terms in the unknown and all terms which is differentiated twice [13].

What is left is an equation which still contain all the sine and cosine terms. As all sine and cosines with different argument are linear independent, we can extract the coefficients as individual equations and we get:

The coefficient to $\cos(k_\mathrm{p}x - \omega_\mathrm{p}t)$:

$$-k_\mathrm{p}^2 E'_\mathrm{p} + \frac{n_\mathrm{b}^2\omega_\mathrm{p}^2}{c^2}E'_\mathrm{p} + \mu_0\omega_\mathrm{p}^2 U_\mathrm{p} - 2\frac{n_\mathrm{b}^2\omega_\mathrm{p}}{c^2}\frac{\partial E''_\mathrm{p}}{\partial t} - 2\mu_0\omega_\mathrm{p}\frac{\partial V_\mathrm{p}}{\partial t} - 2k_\mathrm{p}\frac{\partial E''_\mathrm{p}}{\partial x} = 0 \qquad \text{(A.5a)}$$

The coefficient to $\sin(k_\mathrm{p}x - \omega_\mathrm{p}t)$:

$$k_\mathrm{p}^2 E_\mathrm{p}'' - \frac{n_\mathrm{b}^2\omega_\mathrm{p}^2}{c^2}E_\mathrm{p}'' - \mu_0\omega_\mathrm{p}^2 V_\mathrm{p} - 2\frac{n_\mathrm{b}^2\omega_\mathrm{p}}{c^2}\frac{\partial E_\mathrm{p}'}{\partial t} - 2\mu_0\omega_\mathrm{p}\frac{\partial U_\mathrm{p}}{\partial t} - 2k_\mathrm{p}\frac{\partial E_\mathrm{p}'}{\partial x} = 0 \tag{A.5b}$$

The coefficient to $\cos(k_\mathrm{c}x - \omega_\mathrm{c}t)$:

$$-k_\mathrm{c}^2\mathcal{E}_\mathrm{c} + \frac{n_\mathrm{b}^2\omega_\mathrm{p}^2}{c^2}\mathcal{E}_\mathrm{c} + \mu_0\omega_c^2\mathcal{U}_\mathrm{c} = 0 \tag{A.5c}$$

The coefficient to $\sin(k_\mathrm{c}x - \omega_\mathrm{c}t)$:

$$\mu_0\omega_c^2\mathcal{V}_\mathrm{c} = 0 \tag{A.5d}$$

Using the dispersion relation $k = \frac{n_\mathrm{b}\omega}{c}$ the E_p' terms cancel from (A.5a) and so does the E_p'' terms from eq. (A.5b). Hence we have two separate equations for each of the probe field envelopes. The last two equations reduce to

$$\mathcal{U}_\mathrm{c} = 0 \quad \mathcal{V}_\mathrm{c} = 0.$$

This is a consequence of assuming that $\mathcal{E}_\mathrm{c}$ is constant. If not so $\mathcal{U}_\mathrm{c}$ and $\mathcal{V}_\mathrm{c}$ would act as source terms to the coupling field and thus change it. $\mathcal{U}_\mathrm{c}$ and $\mathcal{V}_\mathrm{c}$ are related to σ_{23} in the same way that the probe polarization is related to σ_{12}, and σ_{23} is not zero, see figure A.7(a). Thus we neglect the coupling between σ_{23}, $\mathcal{U}_\mathrm{c}$, and $\mathcal{V}_\mathrm{c}$. This elimination is justified by our assumption that $\mathcal{E}_\mathrm{c}$ is strong compared to $|E_\mathrm{p}|$, hence our model is not valid when the two fields are comparable. By comparing figure A.7(a) to figure A.5(e) we see that σ_{23} is 2 to 3 magnitudes smaller than σ_{12}, and the approximations are well satisfied for our default values.

Equations (A.5a) and (A.5b) now look like

$$\begin{aligned}
2\frac{n_\mathrm{b}^2\omega_\mathrm{p}}{c^2}\frac{\partial E_\mathrm{p}''}{\partial t} + 2k_\mathrm{p}\frac{\partial E_\mathrm{p}''}{\partial x} &= \mu_0\omega_\mathrm{p}^2 U_\mathrm{p} - 2\mu_0\omega_\mathrm{p}\frac{\partial V_\mathrm{p}}{\partial t} \\
2\frac{n_\mathrm{b}^2\omega_\mathrm{p}}{c^2}\frac{\partial E_\mathrm{p}'}{\partial t} + 2k_\mathrm{p}\frac{\partial E_\mathrm{p}'}{\partial x} &= -\mu_0\omega_\mathrm{p}^2 V_\mathrm{p} - 2\mu_0\omega_\mathrm{p}\frac{\partial U_\mathrm{p}}{\partial t}
\end{aligned}$$

The last term in each equation can be approximated out, again according to the slowly varying envelope approximation by using that $\frac{\partial V_\mathrm{p}}{\partial t} \ll \omega_\mathrm{p}U_\mathrm{p}$ and $\frac{\partial U_\mathrm{p}}{\partial t} \ll \omega_\mathrm{p}V_\mathrm{p}$. If we divide by $2k_\mathrm{p}$ and utilize the dispersion relation we get

$$\begin{aligned}
\frac{\partial E_\mathrm{p}''}{\partial x} + \frac{n_\mathrm{b}}{c}\frac{\partial E_\mathrm{p}''}{\partial t} &= \frac{\mu_0\omega_\mathrm{p}c}{2n_\mathrm{b}}U_\mathrm{p} \\
\frac{\partial E_\mathrm{p}'}{\partial x} + \frac{n_\mathrm{b}}{c}\frac{\partial E_\mathrm{p}'}{\partial t} &= -\frac{\mu_0\omega_\mathrm{p}c}{2n_\mathrm{b}}V_\mathrm{p}
\end{aligned}$$

These are the two forward propagating wave equations governing the two envelopes for the probe field, which are valid under the above assumptions.

A.8. The phase of the electric field and detuning

In this appendix we will look at the phase ϕ_p of the probe field, which from our solutions of E'_p and E''_p can be calculated from

$$\phi_\mathrm{p} = \arctan\left(\frac{E''_\mathrm{p}}{E'_\mathrm{p}}\right)$$

which have to take into account which quadrant the complex envelope $\tilde{E}_\mathrm{p} = E'_\mathrm{p} + iE''_\mathrm{p}$ represent. When $E''_\mathrm{p} = 0$ the field would ether have $\phi_\mathrm{p} = 0$ or $\phi_\mathrm{p} = \pi$. This is the case for zero detuning when $\Delta_\mathrm{p} = \omega_{21} - \omega_\mathrm{p} = 0$ and $\Delta_\mathrm{c} = \omega_{32} - \omega_\mathrm{c} = 0$. This can be seen by examine of the Bloch equations. If the initial conditions are zero for all variables except for ρ_{11} and E'_p, both being real. Then Ω_p is real and we enter a self-consistent mode for the system in which

$E'_\mathrm{p} \in \,]-\infty;\infty[$	$E''_\mathrm{p} = 0$
ρ_{11} : Real	ρ_{22} : Real
ρ_{33} : Real	σ_{12} : Imaginary
σ_{13} : Real	ρ_{23} : Imaginary.

From this we can see that σ_{12} will never have a real part, which is the source term in the E''_p wave equation, (7.5b), and E''_p will remain zero.

For zero detuning, solutions for all dependent variables are in the left side of figures A.3 to A.7. All the white plots are zero, which exactly correspond to the ones predicted by the mode described above. Though for zero detuning we only have discontinuous phase changes when the field envelope is zero.

If we change the detuning from zero, there are no restrictions on the real and imaginary parts of the off-diagonal elements. The source term to the E''_p-equation is in general no longer zero. This means that ϕ can now have any value in the interval $[-\pi;\pi]$. In the plots in the right side of figures A.3 to A.7 all dependent variables are plotted again for $\Delta_\mathrm{p} = 450$ GHz. The Rabi frequency, Ω_c, also has this value.

The main difference is, that the phase now changes continuously and seems to rotate linearly in time, which effectively corresponds to a frequency change.

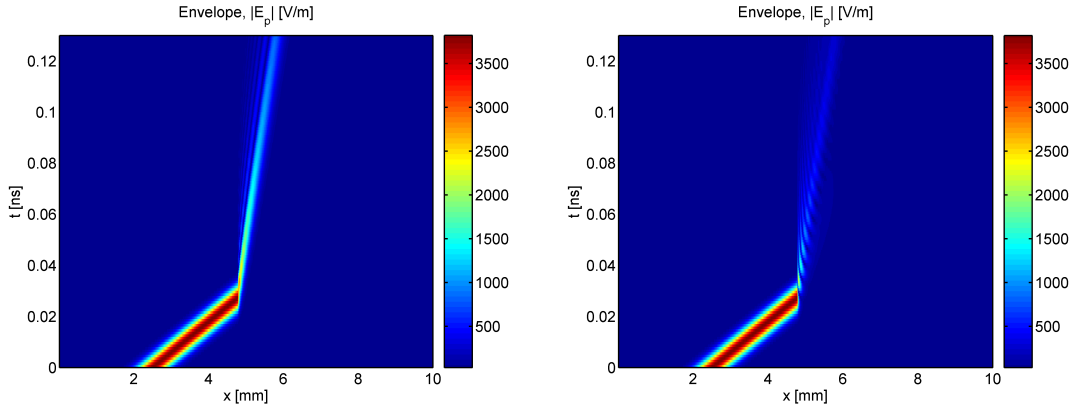

(a) For no detuning.

(b) For $\Delta_{\mathrm{p}} = 450$ GHz

Figure A.3.: *The electric field envelope with and without detuning.*

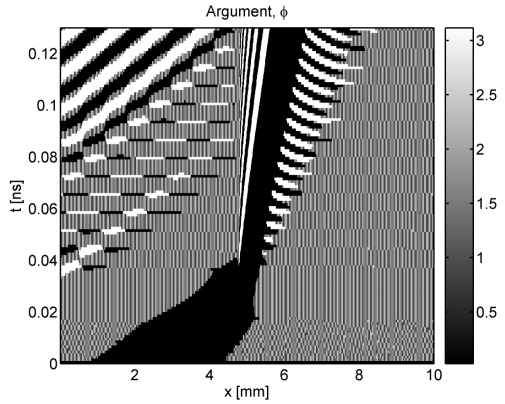

(a) For no detuning.

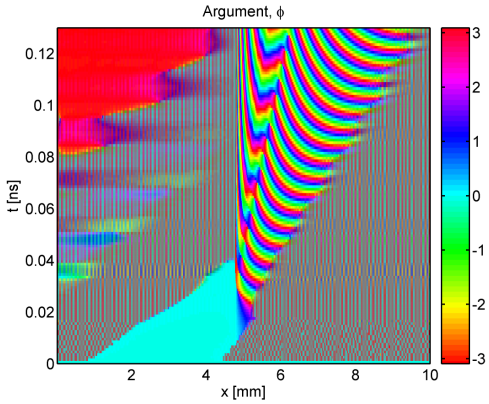

(b) For $\Delta_p = 450$ GHz

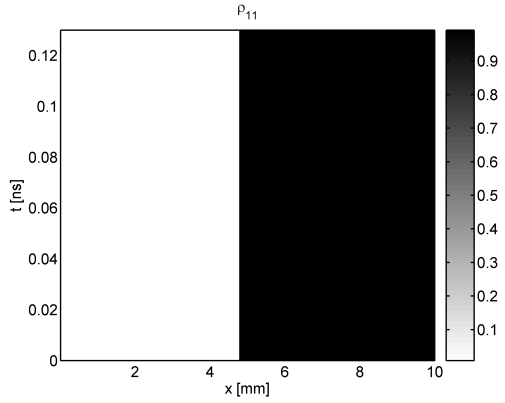

(c) For no detuning.

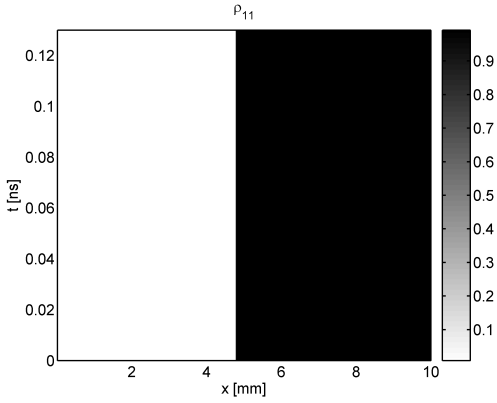

(d) For $\Delta_p = 450$ GHz

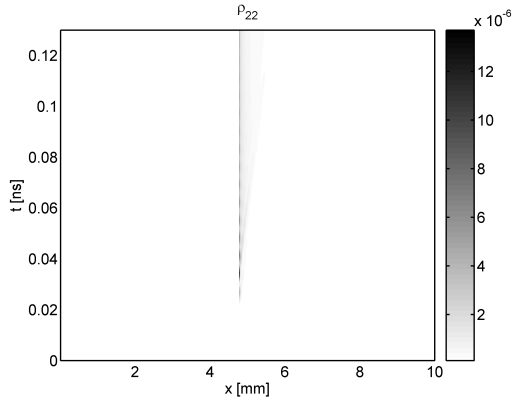

(e) For no detuning.

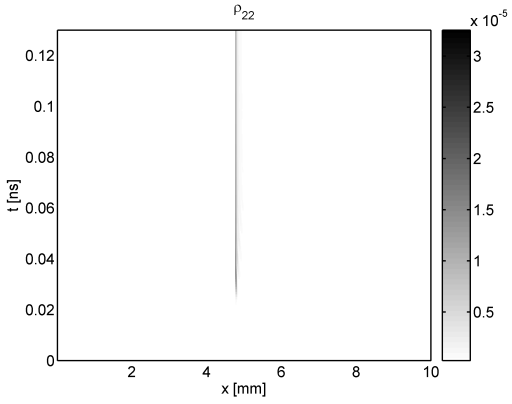

(f) For $\Delta_p = 450$ GHz

Figure A.4.: *The phase and population of the ground state and first exited state with and without detuning. All the small ripples outside the wave in the phase plot represent numerical errors, as E_p'' oscillates at a very low value around zero.*

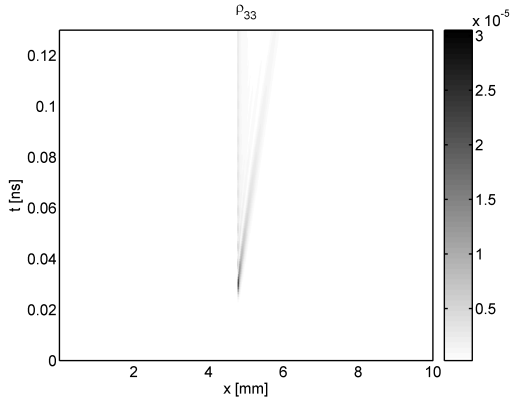

(a) For no detuning.

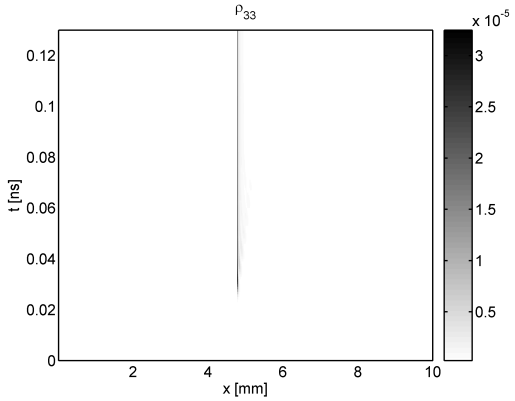

(b) For $\Delta_p = 450$ GHz

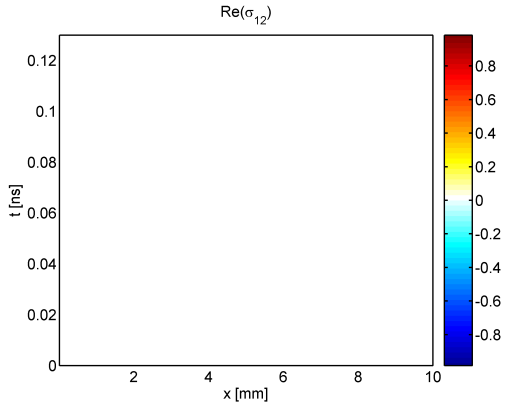

(c) For no detuning.

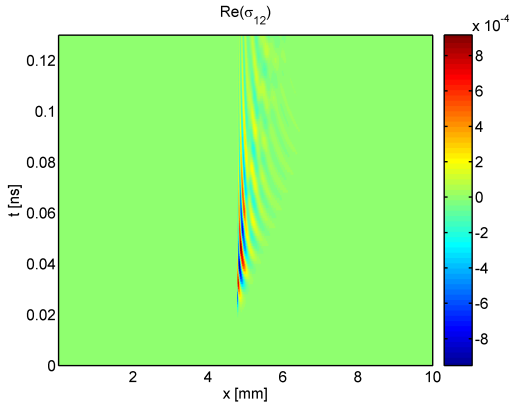

(d) For $\Delta_p = 450$ GHz

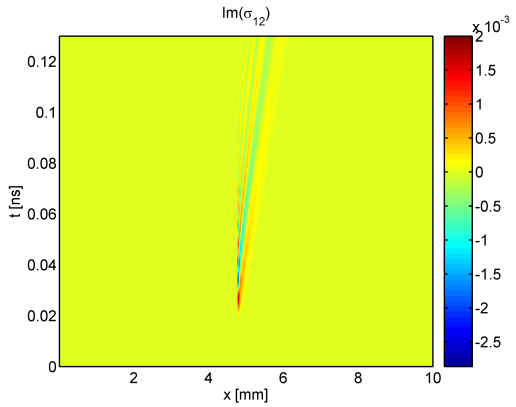

(e) For no detuning.

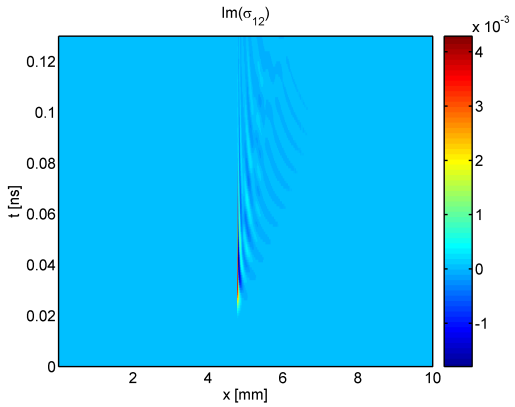

(f) For $\Delta_p = 450$ GHz

Figure A.5.: *The population of the* $|3\rangle$ *state and* σ_{12} *with and without detuning.*

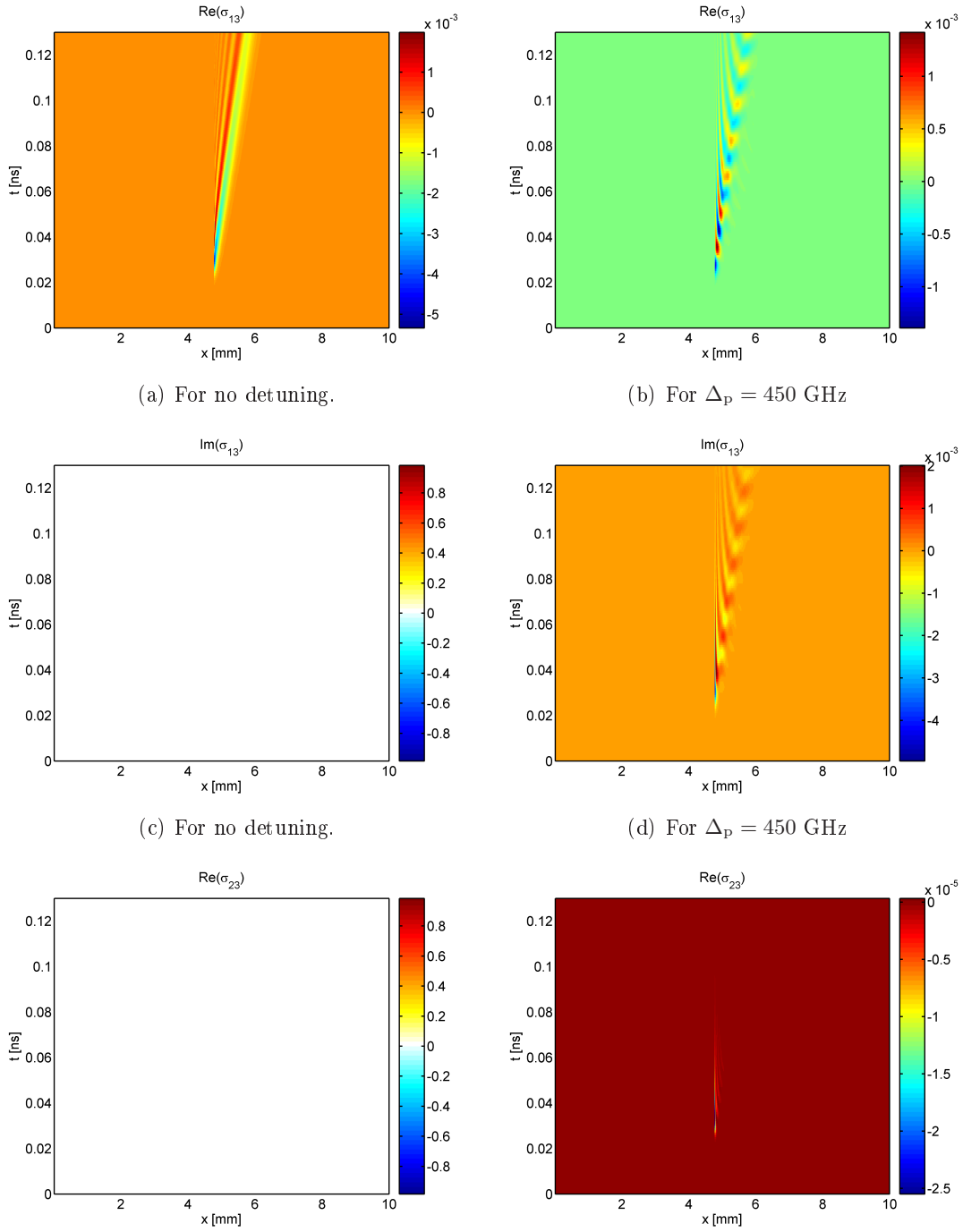

(a) For no detuning.

(b) For $\Delta_p = 450$ GHz

(c) For no detuning.

(d) For $\Delta_p = 450$ GHz

(e) For no detuning.

(f) For $\Delta_p = 450$ GHz

Figure A.6.: *σ_{13} and the real part of σ_{23} with and without detuning.*

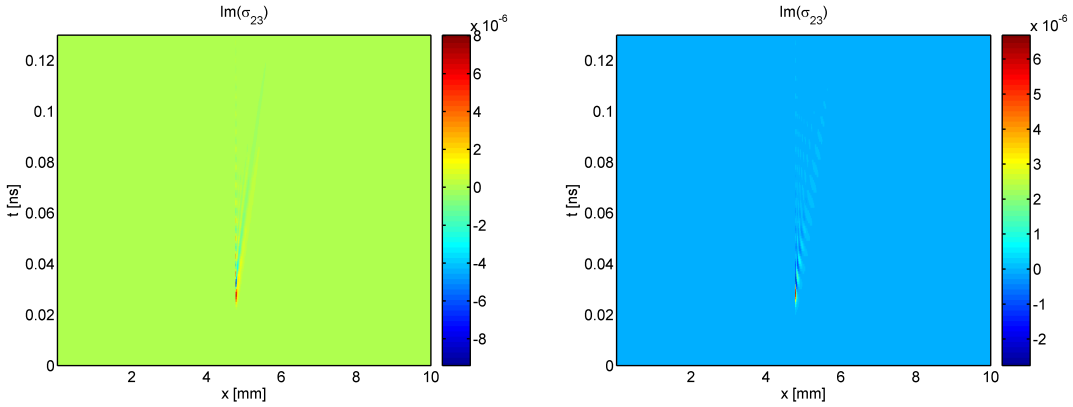

(a) For no detuning.

(b) For $\Delta_{\mathrm{p}} = 450$ GHz

Figure A.7.: *The imaginary part of σ_{23} with and without detuning.*